Optimization and Investigation of SO_2 Adsorption Process for Solid Oxide Fuel Cell Cathode Protection

by

Peng Cheng

A dissertation submitted to the Graduate Faculty of
Auburn University
in partial fulfillment of the
requirements for the Degree of
Doctor of Philosophy

Auburn, Alabama
May 7, 2017

Keywords: wet laid process, microfibrous structure, mass transfer, kinetic study, cathode filter design, fuel cell performance

Approved by

Bruce J. Tatarchuk, Chair, Professor of Chemical Engineering
Yoon Y. Lee, Professor of Chemical Engineering
W. Robert Ashurst, Associate Professor of Chemical Engineering
Bart Prorok, Professor of Materials Engineering

Abstract

Gas-phase contaminant removal is a critical process for power supply systems (e.g. fuel cells and gas turbines). Because of high-energy efficiency, low emissions, and fuel flexibility, Solid Oxide Fuel Cells (SOFCs) are promising energy converting devices. However, various types of contaminants on the cathode side of SOFCs can cause performance degradation, such as sea salt particles and sulfur compounds. Recently, researchers have shown significant degradation caused by SO_2, which reacts with cathode side materials and blocks the active sites available for oxygen reduction reaction. The major SO_2 source is the emission from marine fuels such as JP-5 and JP-8 whose sulfur content can be up to 1200 ppmw. It has also been reported that 5-20 ppm SO_2 can be generated after combustion by using high sulfur containing hydrocarbon fuels. Moreover, researchers revealed that cell exposed to as low as 100 ppbv of SO_2 underwent a current loss. Therefore, it is necessary to remove SO_2 from cathode side down to a sub ppm level.

In this study, SO_2 breakthrough performance was studied by using various transition metal supported on gamma alumina. All of the transition metal containing adsorbents were prepared using incipient wetness impregnation method. Among the candidates, manganese-containing adsorbents exhibited the best sulfur capacity in the preliminary screening test. Furthermore, the effect of manganese loading, types of supports, and calcination temperature were further investigated.

Addition of 5 wt.% Mn demonstrated the highest breakthrough and saturation capacity in the presence of O_2 at room temperature. XRD and H_2-TPR technique revealed that Mn_3O_4 and Mn_2O_3 co-existed in well-dispersed forms. Furthermore, the Mn/Al_2O_3 adsorbent showed better performance than Mn/ZrO_2 and Mn/TiO_2. A possible explanation was that Mn/Al_2O_3 possessed larger population of terminal (isolated) hydroxyl groups on the sorbent surface, which was beneficial during the SO_2 adsorption process. According to the XPS study, the hydroxyl groups on $5Mn/Al_2O_3$ and $5Mn/ZrO_2$ were 18.8 % and 15.9 %, respectively. Therefore, the XPS study can explain why the capacity of using Al_2O_3 support was higher than that of using ZrO_2. Additionally, the role of manganese oxidation state was studied by XPS and H_2-TPR technique. It was also believed that the activity of low valence manganese oxide species was higher than that of Mn(IV). This conclusion was supported by the study of calcination temperature effect. In chapter III, the TPR results show the average oxidation state (AOS) decreased monotonously with increasing calcination temperature. The SO_2 removal capacity of $5Mn/Al_2O_3$ calcined at 650 °C (AOS =1.57) exhibited the highest performance in the presence of 10 ppm SO_2 in air. Oxygen chemisorption was also used to characterize the dispersion of manganese on the surface; however, the effect of active metal dispersion was not clear in this work and needs further investigation. The textual properties such as BET surface area, pore volume were also measured. They were important factors in SO_2 adsorption process. The regeneration condition and aging tests were discussed in this part as well.

The kinetics of non-catalytic gas-solid reaction between MnO_x/γ-Al_2O_3 and SO_2 at room temperature (20 °C) was investigated in Chapter IV. A mathematical model coupled with axial dispersion effect, external and internal diffusion resistance, and depletion mechanism of sorbent can not only fit the breakthrough results but also predict the breakthrough curves of packed bed (PB) and microfibrous entrapped sorbents (MFES) with acceptable deviations. The model consists of two important variables: initial sorption rate constant (k_o) and depletion rate constant (k_d), which can be determined by fitting the model to experimental data. Due to uniform flow pattern and minimized bed channeling, MFES outperformed conventional packed bed. The regeneration performance of MFES surpassed that of PB significantly in model anode exhaust gas (AEG) at ca. 650 °C. Furthermore, MFES maintained its breakthrough capacity up to 5 regeneration/adsorption cycles. Thus, the drawbacks of the packed bed due to flow maldistribution can be addressed employing MFES.

In Chapter V, based on the mathematical model derived in the previous chapter, we could estimate the parasitic power consumed by the fuel cell system under various filter designs. For the case study, a 60 kW fuel cell stack was investigated. Generally speaking, when long term protection is required, composite bed and packed bed is the best option due to their high capacity. However, when long term protection is not the primary concern and high removal efficiency is required, MFES consumes the least parasitic power. Hence, it is vital to choose the best filter design based on various environmental condition.

In Chapter VI, the strategy of protecting the Proton Exchange Membrane Fuel Cells (PEMFC) was discussed. Volatile Organic Compound was selected as the model impurity. Various activated carbons were used as sorbents for the fuel cell filters. Meanwhile, Yoon and Nelson model was used to describe this adsorption process. In this part, we also applied a chemical activation method to enhance the adsorption performance.

Some proposed future works are listed in Chapter VII, including the investigation of altering the population of surface hydroxyl groups on the sorbent surface, UV-assisted SO_2 adsorption on Mn/TiO_2, incorporation of other additives to enhance the SO_2 removal performance.

Acknowledgments

I would like to express my deepest gratitude to Dr. Bruce J. Tatarchuk for his support and guidance for this research. His knowledge and experience both in industry and academia broadened my field of vision in my research area. Without his continuous support mentally and financially, this dissertation would not have been possible. I would also like to express my deepest appreciation to my committee member, Dr. Yoon Lee, who inspired me during my PhD study, especially during the most difficult time. Also, I would like to thank Dr. William Ashurst, who helped me a lot and treated me like a true friend. In addition, a thank you to Dr. Bart Prorok, who provided me some very good advice for the mathematical model developed in this study. I would like to thank Dr. Dong-Joo (Daniel) Kim for serving as my university reader. I would also like to thank Dr. Christopher Roberts and Dr. Mario Eden for their efforts in serving our department. The financial support from the Office of Naval Research for this research is gratefully acknowledged.

I would specially like to thank Dr. Hongyun Yang (IntraMicron Inc.) and Dr. Donald Cahela for their selfless help and suggestions for my research. Their thoughtful idea and critical thinking brought me to the higher level as a PhD. I am grateful to Dr. Yanli Chen and Dr. Amogh Karwa for their training at the beginning of my graduate study. I would like to thank all current and past members of the Center for Microfibrous Materials Manufacturing (CM^3): Dr. Wenhua Zhu, Mr. Dwight Cahela, Ms. Kimberly Dennis, Xinquan Cheng, Dr. Pengfei Zhao, Dr. Robert Henderson, Dr. Xueni Sun, Mingyang Chi,

Dr. Qiang Gu, Dr. Guomin Xu, Dr. Shahadat Hussain, Dr. Sabrina Wahid, Achintya Sujan, and Dr. Abhijeet Phalle.

I am very thankful to the following members of the Staff who have helped to a great extent during my PhD study: Dr. Allan David, Dr. Joseph Shaeiwitz, Ms. Sue Ellen Abner, Ms. Karen Cochran, Mr. Matt Montgomery, and Mr. Brian Scweiker. I am also greatly thankful to the friends who helped me and guided me throughout my PhD: Mr. Ming Fang, Dr. Chen Zhou, Dr. Shaima Nahreen, Dr. Jie Zhong, Pengcheng Li, Xin Fan, Shu Fang, Nan Wei, Dr. Rujian Fu, Dr. Rui Xu, Dr. Wen J. Seeto, and Dr. Teng Xu.

This dissertation would not have been possible without the unwarranted love and encouragement from my parents, and especially my wife. Finally, I would like to thank the Almighty that makes this happen.

Table of Contents

List of Figures

List of Tables

Chapter I Introduction and Literature Review

I.1 Introduction of Solid Oxide Fuel Cell (SOFCs)

I.1.1 Components of SOFCs

Currently, numerous research groups throughout the world has focused on the third generation fuel cell-Solid Oxide Fuel Cell (SOFCs), which is able to fulfill the requirement of high efficiency, fuel flexibility, long stability, and zero/low emissions[1–6].

Among various types of fuel cells, solid oxide fuel cell requires extremely high operating temperature (e.g. 600~1000 °C) and can use natural gas or propane as its fuels since its advantage of fuel flexibility. SOFC is supposed to be very reliable in large, high power applications (e.g. full-scale industrial plants or U.S. Navy shipboard).

The major components of a single SOFC include electrolyte, cathode, and anode as shown in Figure I.1. In addition, fuel cell stacks is composed of an electrical interconnect, which is able to connect every single cell together in series or parallel. The electrolyte is mainly made of YSZ and works as an oxide ion conductor. In general, oxygen atoms are reduced into oxide ions on the surface of cathode. Then the oxide ion penetrates through the ceramic electrolyte to the anode side, where the oxide ions react with the fuel comes from the anode and generates electrons.

Table I.1 Materials of SOFC Components[1]

Components	Materials
Electrolyte	Y_2O_3-Stabilized ZrO_2 (YSZ)
	Cerium oxide doped with samarium (SDC)
	Cerium oxide doped with gadolinium (GDC)
	Cerium oxide doped with yttrium doped Ceria (YDC)
	Strontium Cerate (SYC)
Anode	NiO/YSZ (suited for YSZ electrolyte)
	NiO/SDC or NiO/GDC (suited for ceria based eletrolyte)
Cathode	$LaSrMnO_3$ (LSM)
	$LaCaMnO_3$ (LCM)
	$LaSrFeO_3$ (LSF)
	$SmSrCoO_3$ (SSC)
	$LaSrCoO_3$ (LSC)
	$LaSrCoFeO_3$ (LSCF)

Note: Both the anode and cathode are made of porous structure to accelerate mass transport of reactant and product gases.

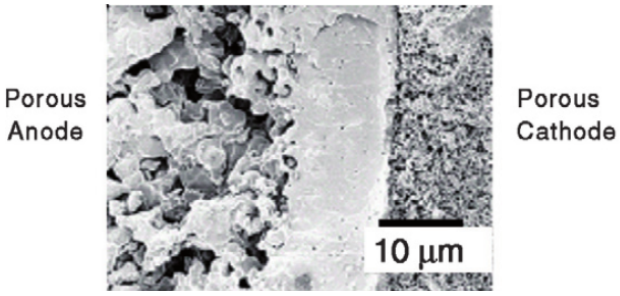

Figure I.1 SEM image of SOFC microstructures.[7]

Usually, the anode is composed of Ni-ZrO_2 cermet. The function of the zirconia material is to prevent the metal particles from sintering and provides a thermal expansion coefficient comparable to that of the electrolyte material. In addition, the anode material of SOFCs possesses the property of high porosity. Therefore, it can favor the mass transport of reactant as well as the product gases.

Similarly, the cathode of SOFCs is also made of porous structure that facilitates rapid mass transport for reactant or product gases. As listed in Table I.1, strontium doped lanthanum manganite is most widely used for the cathode material. Some other materials such as p-type semi-conductors are being used for SOFCs. The application of these materials is beneficial for decreasing the SOFC operation temperature, which can reduce the cost of materials. For this reason, mixed conductors like lanthanum strontium ferrite and lanthanum strontium cobaltite are better candidates than the lanthanum strontium manganite.

As mentioned earlier, because of the high temperature operation condition, SOFCs face a great deal of challenges on its materials. Recently, it was reported that planar SOFC is

capable of operating at lower temperatures (700-850 °C). Considering the ability of SOFC can use conventional fossil fuels, the cost of the SOFCs can be reduced significantly.

I.1.2 Factors Affecting the Performance of SOFCs

a) Pressure

Similar to all types of fuel cell, the performance of SOFCs is enhanced with increasing cell pressure. If the pressure is increased from P_1 to P_2, the voltage difference can be expressed as follows:

$$\Delta \boldsymbol{V} = 0.027 \ln\left(\frac{\boldsymbol{P_2}}{\boldsymbol{P_1}}\right)$$

For SOFCs combined with gas turbine, high pressure operation condition favors the performance significantly.

b) Temperature

It is well known that the effect of temperature is of great importance on the SOFCs performance. The main reason is that higher temperature can enhance the conductivity of materials, which reduces the ohmic loss of the fuel cell. Therefore, most of the SOFCs operate at the temperature range of 800-1000 °C. As a result, LSM-based composites remain the most widely used materials on the cathode because of their excellent long-term stability when operate at high temperatures.

I.2 Introduction of SOFCs Cathode Air Protection

There are two main types of air contaminants in air. The first one is particulate contaminants, including soot, smoke, dust, sea salt particles and so forth[8]. The other one is gas phase contaminants, such as VOCs, NO_x, and SO_2.

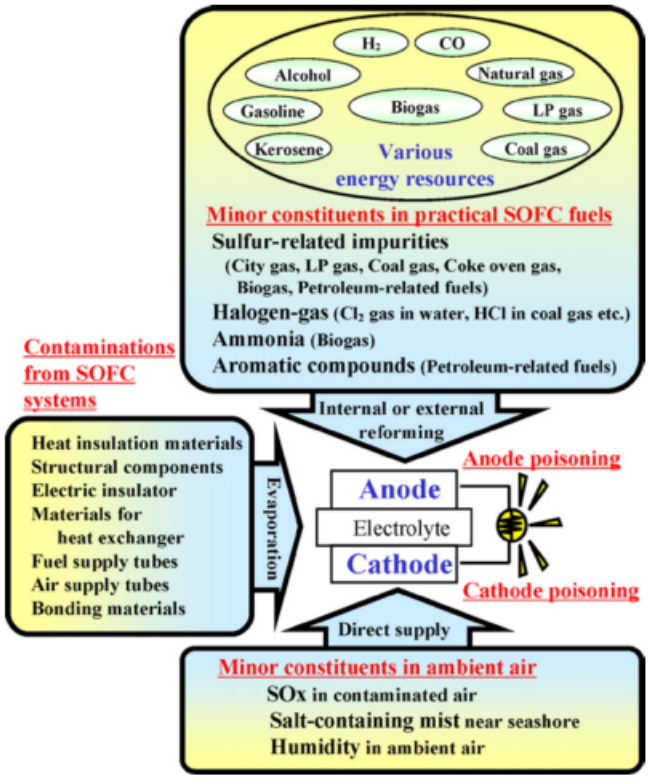

Figure I.2 Possible contaminants of SOFCs.[8]

Since ambient air is continuously introduced into the cathodes during operation over a long period of time, external contaminant poisoning effects should be taken into account[5]. The extrinsic impurities, which can lead to chemical degradation of SOFCs, are demonstrated in Figure I.2. On the cathode of SOFCs, it can be seen that SO_2 is the most

typical contaminant other than the salt particles. Sulfur dioxide poisoning remains a critical issue for the SOFCs cathode degradation[9], even though the cathodes of SOFCs possess higher sulfur tolerance than that of proton exchange membrane fuel cells (PEMFCs)[4,10].

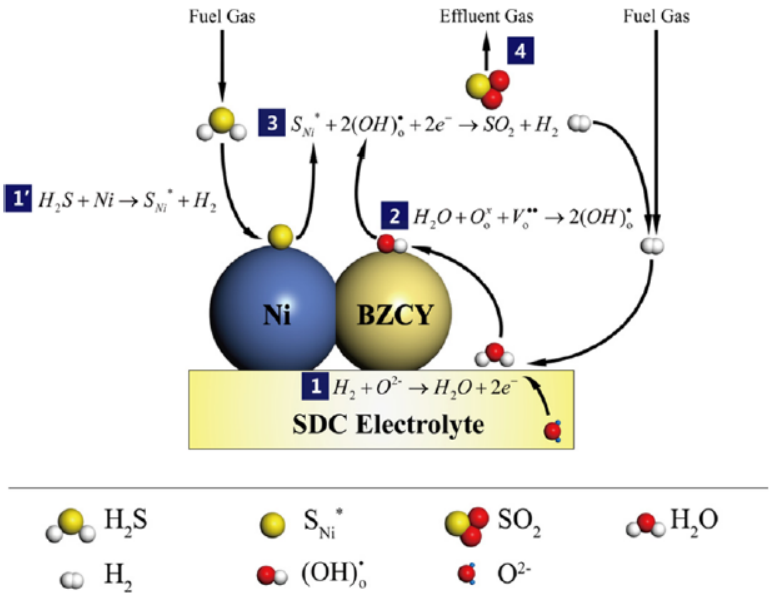

Figure I.3 Proposed mechanism for Ni+BZCY anodes using hydrogen fuels containing 100-1000 ppm of H_2S.[21]

Usually, SO_2 is generated in the process of burning of fossil fuels in factories, power plants, automobiles, or fuel cell power systems[11]. As we know, in military logistic SOFC system, the sources of SO_2 mainly arise from marine fuels, such as JP-5 and JP-8. For example, JP-5 jet fuel obtained from US Office of Naval Research contains c.a. 1050 ppmw S[12–16]. Sulfur dioxide is present not only in fuel emissions, but it can also be transformed from some other sulfur species (e.g. H_2S, organosulphur compounds) at elevated temperatures[17]. As illustrated in Figure I.3, the sulfur containing fuels can not only cause

Ni+SDC anode degradation, it also generate SO_2 which can further react with the cathode materials on the grain boundary of SOFC cathode[18]. It has been reported that 5-20 ppm SO_2 can be generated after combustion in a typical engine exhaust[11,19,20].

I.3 Sulfur Dioxide Poisoning Effect on SOFCs Cathode

SO_2 is known as the major sulfur-containing anthropogenic toxic gas, which can lead to acid smog formation or acid rain[21]. Many countries have regulations about limiting the emission of SO_x into the atmosphere since it is very harmful to human beings. (e.g. causing eye, nose, and throat irritations, choking, cough, and so forth.) According to United States Environmental Protection Agency, it was set in 1971 that the primary standard for SO_2 is 140 ppbv. In addition, EPA defined 500 ppbv as a 3-hour average secondary standard.

Over recent years, many researchers investigated the SO_2 poisoning effect on SOFCs cathode. It is well known that even with ultra-low sulfur content fuels, the long period adverse effects of small amount of SO_2 in emissions is detrimental to fuel cell performance[22]. The sulfur contaminants build up in the fuel cell system, resulting in more severe degradation with longer exposure times[23]. Wang et al.[24,25]experimentally studied SO_2 poisoning effect on $LaSrCoFeO_3$ (LSCF) cathode for SOFCs. They revealed that there was apparent current loss even if the cell exposed to 100 ppbv SO_2 balanced in air for c.a. 100 h, though the cell performance could be partially recovered if the SO_2 source was cut from the air stream. As shown in Figure I.4, 0.1 ppmv SO_2 was introduced into the LSCF

cathode and the performance degradation was around 3 % after 2 h[24]. After the SO_2 was cut from the air after 2 h, the degradation was recovered c.a. 1.5 %. Wang et al.[24] further stated that the SO_2 adsorption is responsible for the rapid performance degradation, which was confirmed by SEM and EDX results. Furthermore, long time operation (>5000 h) of fuel cell may cause $SrSO_4$ precipitates. It is well known that $SrSO_4$ formation can block the active surface[26], reduce the cathode porosity, and lead to morphological changes[9].

Researchers also investigated the current loss when the fuel cell was exposed to SO_2 with various flow rates. As shown in Figure I.5, when the flow rate of air was set to 25 mL min^{-1}, I/I_o value decreased drastically to 95 % during the first 10 h. After that, I/I_o value gradually decreased from 10 to 100 h. The similar phenomenon took place at the flow rate of both 50 and 90 mL min^{-1}. In addition, the higher the flow rate, the worse the degradation for the fuel cell performance. However, the author did not explain the mechanisms regarding two degradation stages (< 10 h and > 10 h).

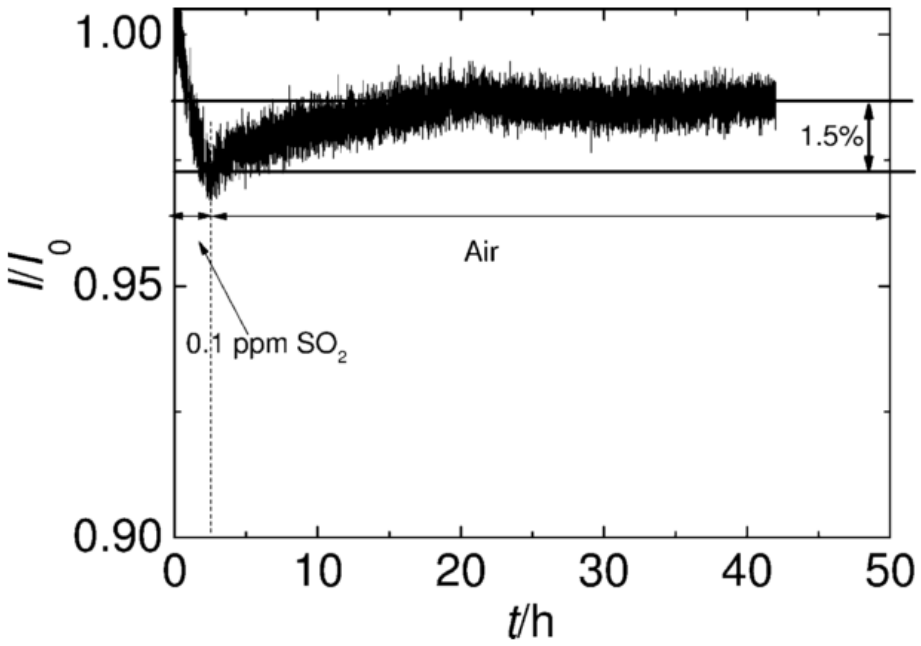

Figure I.4 Sulfur poisoning and recovery performance after exposure to 0.1 ppmv SO_2 for 2 h.[25]

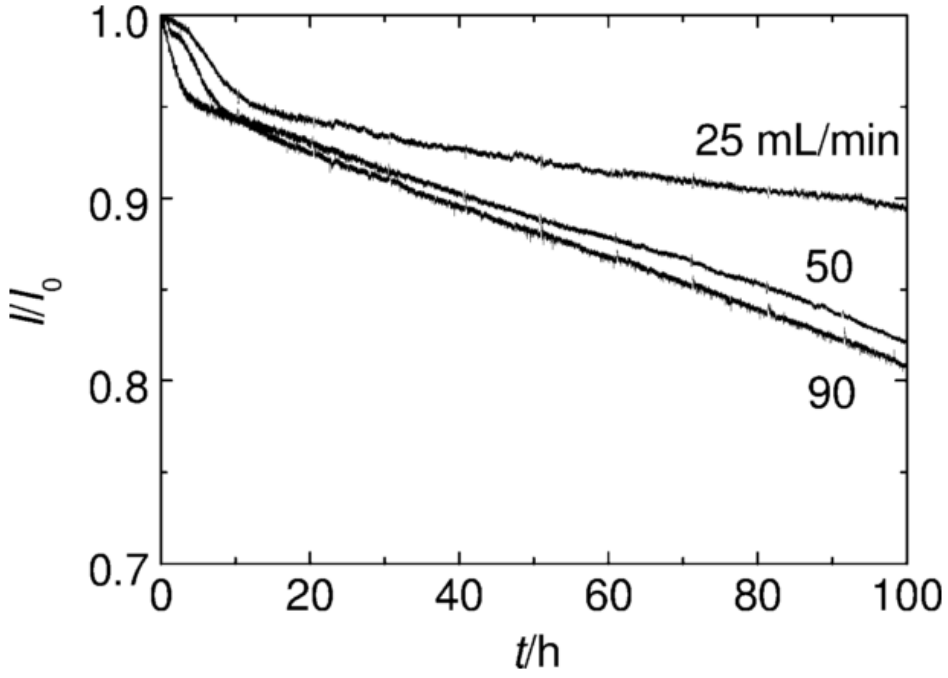

Figure I.5 Time dependence of I/Io of the cells exposed to 100 ppbv SO_2 for 100 h at various flowrates.[25]

I.4 Introduction and History of SO_2 Removal Technologies

I.4.1 Technologies for SO_2 Removal

This section reviewed a number of desulfurization technologies in the past decades. Some of the technologies are being used for over 40 years; however, some of them are still staying at the laboratory level. Generally, the most common way to remove SO_2 is to use basic oxide materials. Wet and dry FGD (flue gas desulfurization) processes represent the

major industrial routes designed to control SO_2 emissions in atmosphere. The major drawbacks of wet scrubbing methods are large amounts of water consuming and production of large volumes of waste liquids.

Sulfur dioxide emission control is traditionally applied in flue gas desulfurization. Generally, the flue gas reacts with absorbent medium in either an absorber or scrubber vessel to produce slurry with high sulfur-containing[27].

For wet FGD systems, the wet scrubbers generate wet products, which can be regenerable or unregenerable. Commercial power generation wet FGD systems mainly use $CaCO_3$, $Ca(OH)_2$, or a mixture of $Ca(OH)_2$ and alkaline fly ash sorbents. An aqueous suspension of these materials is sprayed into towers. Then the SO_2 contacts with the scrubbers and forms into gypsum ($CaSO_4 \cdot 2H_2O$). The drawback for wet FGD system is of low removal efficiency. Typically, it can only reach about 90% efficiency[27]. Therefore, it is not applicable if the inlet concentration of SO_2 is in ppm level. Furthermore, the thermal regeneration of its waste (gypsum) requires a high temperature level. In addition, intensive recrystallization with a drastic loss of porosity and reactivity occurred during the thermal regeneration process. Hence, after reaction, such a "throw-away" process is not able to achieve current and future environmental trends. The CO_2 product will lead to greenhouse gas effect and large amount of wastewater as well as low-grade gypsum cannot be commercialized. Considering the real operation condition, dry desulfurization processes are much more convenient and environmental friendly. Therefore, many studies were

devoted to the development of supported metal oxide sorbents[21]. The supported sorbents are not only capable of removing SO_2 with a high efficient, but also show a large surface area and high textural properties, which is favorable for heterogeneous adsorption. In summary, the SO_2 adsorption by using supported sorbents is more applicable for fuel cell cathode system.

I.4.2 Sorbent Screening

Adsorption can be a promising technology to remove SO_2 due to its unique advantages such as ease of adsorbent regeneration, simple adsorber design, and much less problems in waste disposal[20]. Most of the sorbents used in SO_2 adsorption are metal oxides. Based on the thermodynamic data and Gibbs free energies, the metal oxides of iron (Fe), copper (Cu), silver (Ag), manganese (Mn), nickel (Ni), cerium (Ce), calcium (Ca), vanadium (V), zinc (Zn), strontium (Sr), barium (Ba), cobalt (Co) and magnesium (Mg) have the thermodynamic feasibility for SO_2 adsorption. Among these candidates, Co, Fe, V, and Zn are usually operated at low temperature (300-550 °C). Since SOFC usually operates at high temperature (>600 °C), these candidates are not suitable for cathode filter adsorbents. Qualitatively, a sorbent designed to be effective over a wide temperature range must undergo sorption with a negative standard free Gibbs energy over that range. In 1971, Lowell et al.[28] evaluated 47 different oxides for use as sorbents for removing SO_2 from flue gas. There are mainly two factors for them to choose the candidates for future sorbent

development: (1) sorption rate; (2) sorbent stability during long term sorption-regeneration cycles. They mainly use thermodynamic analysis and literature data to select potential sorbents. Firstly, oxides of Ba, Ca, Cd, Cs, K, La, Li, Mg, Na, Rb, Sc, Sr, and Y were removed from their list as unfavorable sulfate decomposition temperatures (> 900 °C). Then, oxides of Ag, As, B, and Si were eliminated because of unfavorable chemistry such as decompose to free metal. In addition, Be was removed from their list because of its toxicity. Furthermore, Ga, Ge, Ir, Pd, Re, and Rh were eliminated since their high cost. In addition, MoO_3 was eliminated because it has a high vapor pressure at elevated temperatures. Finally, the potential sorbents remains on Lowell's list are Ti, Zr, V, Fe, Co, Ni, Cu, Zn, Al, Ce, and Mn. An experimental studies conducted by Bienstock et al. suggested that bulk oxides of Mn, Co, and Cu were the most promising candidates for SO_2 adsorption. Furthermore, to improve the physical strength of DeSOx sorbents, interests of research focused on the development of supported sorbents. In 1974, Vogel et al. evaluated a number of impregnated metal oxides supported on alumina for SO_2 removal at 343 °C and summarized that the supported oxides of Na, K, Sr, Ca, Cr, and Cu demonstrated high reactivity to SO_2. However, there was a hydrogen pretreatment step (482 °C) for their sorbents, which would affect the activity of Mn and Co. Further study were conducted by Koballa et al. stated that the oxides of Ni, Mn, Fe, Co, and Zn were the most promising metal oxide sorbents for SO_2 adsorption. In the following part, sorbents based on various metal oxides, and some sorbents widely used in industry such as CaO, MgO will be

discussed alphabetically in this work. In addition, mixed oxide adsorbents on various support materials will be discussed in the following part.

I.4.2.1 Calcium Oxide Based Sorbents

Calcium oxide (in the form of limestone, hydrated lime or lime) is a sorbent widely used in both laboratorial and industrial scale and is able to remove most acid gases such as CO_2, H_2S, and SO_2 even at low temperatures[29]. In most cases, CaO based sorbents are disposable sorbents, though it has high efficiency and capacity to SO_2. Their typical regeneration temperature is above 1000 °C, which is not practical for industrial application. There are two major techniques for calcium-based sorbents to remove SO_2: (1) wet scrubbing; (2) dry scrubbing.

The wet scrubbing process is given by reaction 1 as follows.

$$SO_2 + CaCO_3 + ½\ O_2 + 2H_2O \rightarrow CaSO_4{\cdot}2H_2O + CO_2 \quad \text{(I-1)}$$

The wet scrubbing process has major economic issues such as large consumption of slurry, release of CO_2 leading to greenhouse effect, and waste of low-grade gypsum that cannot be commercialized.

The dry scrubbing process can be described by reaction 2-4

$$CaO + H_2O \rightarrow Ca(OH)_2 \quad \text{(I-2)}$$

$$Ca(OH)_2 + SO_2 \rightarrow CaSO_3 + H_2O \quad \text{(I-3)}$$

$$CaO + SO_2 + ½\ O_2 \rightarrow CaSO_4 \quad \text{(I-4)}$$

Dry scrubbing process outperformed wet scrubbing process since less energy is required and almost no wastewater is generated during that process. Nevertheless, due to the high decomposition temperatures of $CaSO_3$ or $CaSO_4$ and the sintering effect of the regenerated CaO, both the wet and dry scrubbing process is non-regenerative methods. Therefore, this material will cause many environmental problems.

I.4.2.2 Cerium Oxide Based Sorbents

Cerium oxide (CeO_2) is commonly used as a promoter in SO_2 adsorption rather than the main active metal[30,31]. Ceria is also known as high oxygen storage capacity, which is usually used as a redox catalyst. Jae et al.[32] and Cantu et al.[31] used cerium as a promotor for MgO-based and hydrotalcite-like sorbents to remove SO_2. Jae et al found that the SO_2 breakthrough capacity could be enhanced by 3-4 times with incorporation of 15 wt.% Ce[32]. They also stated that the addition of Ce could drive the SO_2 transform into SO_3. Also, the basic character of CeO_x species favors the SO_2 adsorption on the surface of material[31]. Sumathi et al.[33] impregnated Ce onto palm shell activated carbon to remove SO_2 and NO simultaneously. They reported that Ce was a good candidate for $DeSO_x$ process at temperature range of 100-300 °C. Moreover, Ce as a promotor can lower the regeneration temperature for mixed metal oxide sorbents, which can save numerous energy for industrial process.

I.4.2.3 Copper Oxide Based Sorbents

Copper oxide (CuO) is considered a suitable candidate for industrial applications. Sulfur dioxide reacts with copper oxide and oxygen to generate $CuSO_4$ at 300-500 °C. Regeneration of sulfated sorbent is conducted with a gas stream containing hydrogen, methane, carbon monoxide or ammonia at the same temperature range[34]. After that, the metallic copper in the sorbent can be easily re-oxidized in air at the operation temperature for future SO_2 adsorption cycle. When CuO supported on porous materials, there are more advantages such as high thermal stability, high surface area, and relatively low temperature required for copper desulfation[21]. The following reactions are involved in the DeSOx and regeneration process of CuO.

$$CuO + SO_2 + ½\ O_2 \rightarrow CuSO_4 \quad \text{(I-5)}$$

$$CuSO_4 + 2H_2 \rightarrow Cu + SO_2 + 2H_2O \quad \text{(I-6)}$$

$$CuSO_4 + ½\ CH_4 \rightarrow Cu + SO_2 + ½\ CO_2 + H_2O \quad \text{(I-7)}$$

$$Cu + ½\ O_2 \rightarrow CuO \quad \text{(I-8)}$$

Copper oxide doped on γ-alumina was widely studied by researchers. In literature, approximately 3.5-7.2 wt.% Cu was doped on alumina to achieve the highest SO_2 capacity. Apart from γ-alumina, different porous materials including α-alumina, silica, and titania were also used as sorbent supports[35]. In 1970, McCrea et al.[36] derived a dry, solid adsorbent prepared by impregnating copper salts into a 1/16 inch alumina support. In their work, a

preliminary process design and economic evaluation for power plant utilization are included[36]. Also, they stated that adsorption of SO_2 from flue gas occurs readily at 300 °C or above when the support contains about 4-6 wt.% copper. For the regeneration process, exposure of sulfated sorbents to air or nitrogen at 650-700 °C could not efficiently remove the sulfur species. A minimum of 4 h is required for the sorbent regenerated at 700 °C. In 1994, Yoo and Kim[37] showed that SO_2 adsorption performance of CuO/γ-Al_2O_3 sorbent varied with sulfation temperature as well as the amount of copper loading. Two years later, based on Yoo and Kim's work, Jeong and Kim[38] incorporated alkali salt to the sorbent and increased the SO_2 sorption rate for the bulk sulfation of the CuO/γ-Al_2O_3. They also claimed that the most efficient promoters for CuO/γ-Al_2O_3 sorbent were LiCl, which increased the sulfur removal capacity by about three times compared to the promoter-free sorbent. However, the sorbent did not show good $DeSO_x$ performance at lower temperature (e.g. < 200 °C).

Still further, people also used some novel preparation approaches to enhance SO_2 adsorption performance, such as sol-gel technique. In 1996, Deng and Lin[34] prepared γ-Al_2O_3 supported copper oxide and calcium oxide sorbents by using sol-gel methods. It was found that the sorbent containing 20 wt.% CuO on the surface possessed the highest SO_2 sorption capacity. In 2006, Gavaskar et al.[35] further studied copper-based sorbents prepared via sol-gel routes. It was demonstrated that the highest sorbent capacity was achieved with sorbent incorporated 14.1 wt.% Cu. Furthermore, the ceramic sorbents prepared by sol-gel

method generally provide a high surface area and mechanical strength compared to the conventional incipient wetness impregnation method[35].

Besides this, other supported CuO sorbents and mixed metal oxide sorbents based on CuO have also been widely studied. Corma et al.[39] synthesized hydrotalcite-derived mixed oxides containing Cu, Mg, and Al to remove SO_2 and NO_x in FCC units simultaneously. Cheng et al.[40] used copper impregnated on MgAlFe hydrotalcite-like compounds to remove sulfur for FCC units. They found that copper, as a promoter, is an excellent choice due to its low cost and significant enhancement for SO_2 adsorption. Furthermore, the sorbent can be completely regenerated at 873 K within 15-20 min in hydrogen atmosphere.

The drawback of the copper based sorbent is that the reactivity of the sorbent start to decrease significantly when the reaction temperature is beyond 500 °C. This phenomenon is possibly due to sorbent sintering effect[35]. Additionally, the SO_2 equilibrium concentrations using sorbents of CuO at various temperatures are displayed in Figure I.6.

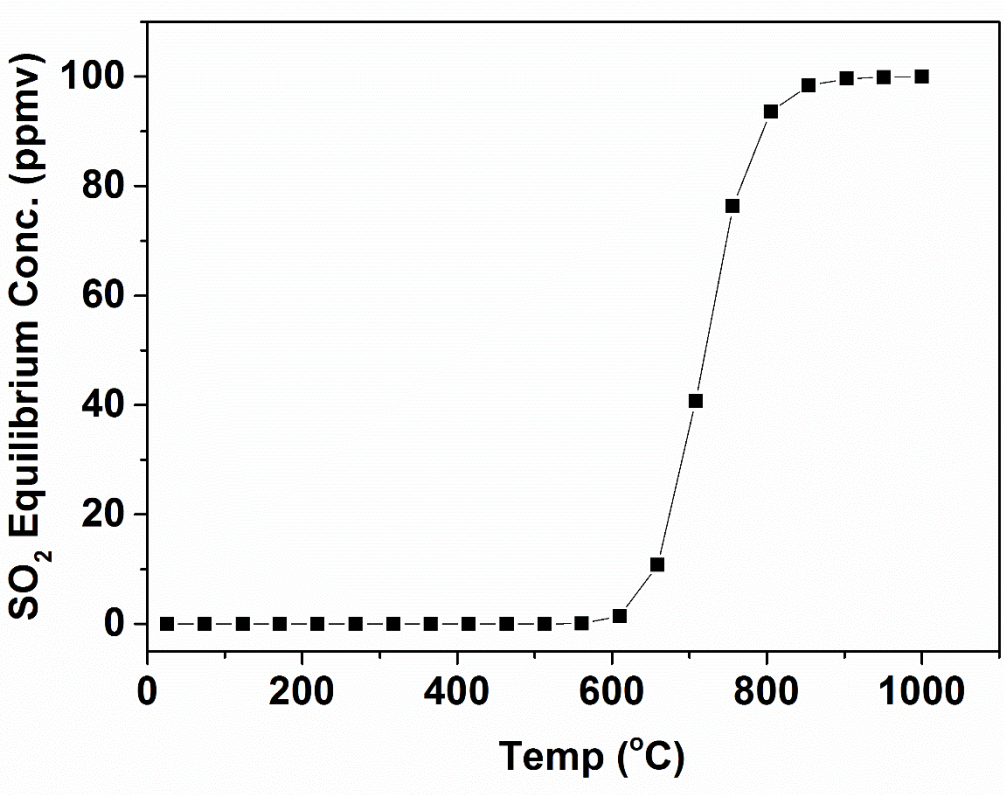

Figure I.6 SO_2 equilibrium concentrations using CuO sorbent at various temperatures. Data were generated by using HSC 6.0 software.

From Figure I.6, we can see that when the temperature approaches around 550 °C, for the thermodynamic reason, the $CuSO_4$ formed starts to decompose into SO_2 and CuO. So the CuO sorbent is not feasible when the desulfurization temperature is beyond 500 °C.

I.4.2.4 Iron Oxide Based Sorbents

Iron oxide (Fe_2O_3), is of low cost and promising candidates for large-scale $DeSO_x$ application. Its application for SO_2 adsorption has been studied since 1970s. Iron oxide supported on alumina is a choice for simultaneously removing NO_x and SO_x from power

plant stack gases. In 1981, Kim and Chol[41] investigated SO_2 oxidation on α-Fe_2O_3 at temperature range from 250 to 400 °C under various P_{SO2} and P_{O2} conditions. They concluded that the reaction is first order with respect to SO_2 and 0.5 order with respect to O_2. Ma et al[42] prepared a novel regenerable Fe/AC sorbents for SO_2 adsorption at low temperatures. In addition, the SO_2 removal ability gradually increases with increasing desulfurization temperature from 150 to 250 °C. Furthermore, the spent Fe/AC sorbent can be regenerated by NH_3 at 350 °C. In addition, Davini et al.[43] stated that by incorporation of iron on activated carbon, the SO_2 adsorption ability was largely increased. They attributed this result to the presence of basic surface sites promoting the initial adsorption of SO_2 and iron derivatives promoting the transformation of adsorbed SO_2 into more stable species.

Recently, iron behaves more as a promotor than a main active site. People usually incorporate iron into hydrotalcite-like compounds to enhance their adsorption and regeneration ability[31,32,44,45]. Cantu et al.[31,44] added c.a. 9 wt.% Fe into MgAl hydrotalcite compounds. The incorporation of iron not only increased the reduction capability but also had no adverse effect on the SO_2 adsorption capacity[31]. Similarly, Jae et al.[32] used Fe and Ce promoted MgO-based sorbents for SO_2 removal and found that Fe was able to enhance the regeneration performance largely.

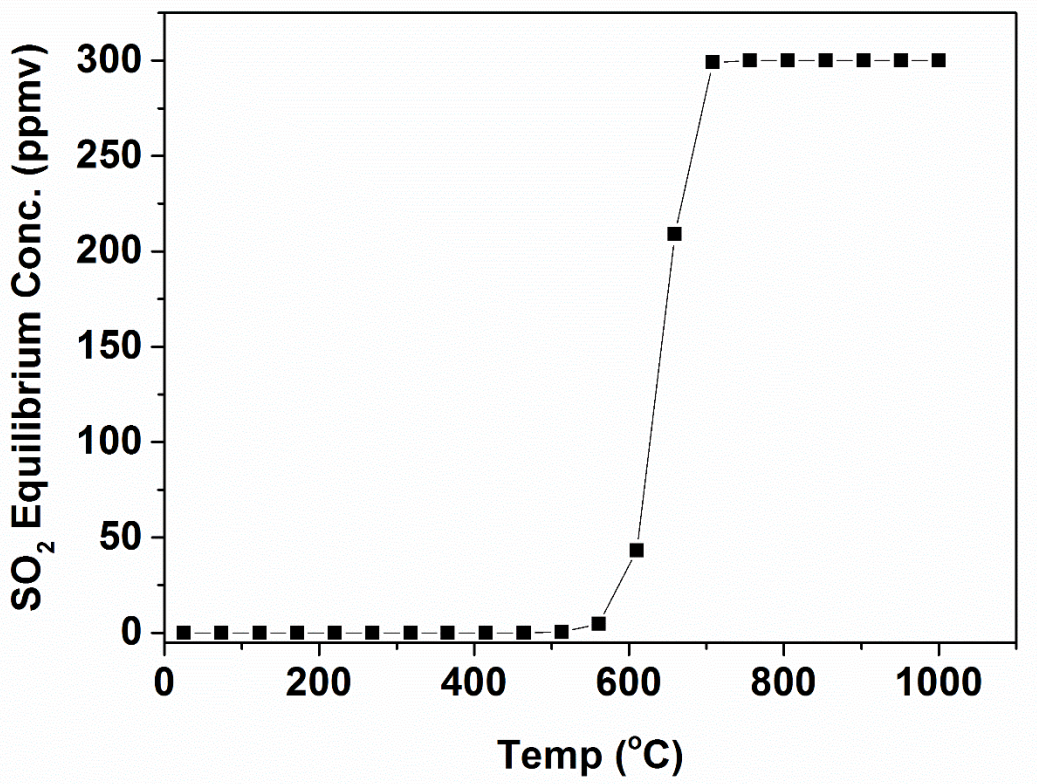

Figure I.7 SO_2 equilibrium concentrations using Fe_2O_3 sorbent at various temperatures. Data were generated by using HSC 6.0 software.

Furthermore, Arcibar-Orozco et al.[46] incorporated 3-4 nm iron nanoparticles onto activated carbon to enhance the SO_2 removal. They revealed that the small iron nanoparticles provided well-dispersed reactive centers and the adsorption capacity was increased by 80 %. However, iron oxide itself cannot remove SO_2 at higher temperature (e.g. T > 450 °C) very effectively. Hence, for SOFC applications, the iron oxide derived sorbent may not be a good choice. The SO_2 equilibrium concentrations using sorbents of Fe_2O_3 at various temperatures are displayed in Figure I.7.

I.4.2.5 Manganese Oxide Based Sorbents

Manganese oxides were first considered as an effective candidate as sorbents for SO_2 removal in 1960s. In 1978, Koballa and Dudukovic[47] summarized that Mn was one of most promising sorbents for SO_2 removal. Manganese oxides, as active components, can be highly dispersed on support materials to remove SO_2. People recently use manganese supported on activated carbons to remove SO_2[48–50]. Also ACF is another choice for SO_2 removal at low temperature[51]. Manganese oxides including MnO_2, Mn_2O_3, Mn_3O_4, and MnO, all of them show activities toward SO_2. Qu et al.[49] summarized that MnO and Mn_3O_4 demonstrated higher activity than MnO_2 in their study. Also, they claimed that the activated carbon containing 5 wt.% Mn calcined at 650 °C in N_2 atmosphere exhibited the best $DeSO_x$ performance. The possible reaction for manganese oxides interact with SO_2 is shown as follows.

$$MnO_2 + SO_2(g) \rightarrow MnSO_4, \quad \text{(I-9)}$$

$$MnO + 2\,SO_2(g) + O_2(g) \rightarrow 2MnSO_4, \quad \text{(I-10)}$$

$$Mn_3O_4 + 3\,SO_2(g) + O_2(g) \rightarrow 3MnSO_4, \quad \text{(I-11)}$$

$$Mn_2O_3 + 2\,SO_2(g) + \frac{1}{2}O_2(g) \rightarrow 2MnSO_4 \quad \text{(I-12)}$$

The regeneration step is usually conducted by heating the spent sorbent under N_2 atmosphere.

$$MnSO_4 \rightarrow 1/2\,Mn_2O_3 + SO_2(g) + 1/4\,O_2(g) \quad \text{(I-13)}$$

$$MnSO_4 \rightarrow 1/3\,Mn_3O_4 + SO_2(g) + 1/3\,O_2(g) \quad \text{(I-14)}$$

Manganese is an excellent candidate for many applications when it is in the oxidized state, such as VOC removal[52–55], SO_x removal[49,56,57], CO oxidation[58–61], SCR of NO_x[61,62], and so forth. Manganese oxides are among the most efficient transition metal for total oxidation, which is a critical sulfate formation step during SO_2 adsorption[59,63]. Compared with noble metals (e.g. Pt, Pd), high stability and low cost render Mn much more available to some practical application[64]. In addition, MnO_x possesses low volatility nature at high temperatures and reacts to a small extent with catalyst support ($MnAl_2O_4$ can be hardly produced unless calcined in hydrogen atmosphere.)[59,60]

It is also well known that manganese oxides possess strong oxygen storage/release ability since they are capable of undergoing a fast redox cycle via the interaction with reducing agent or oxidant[64]. Meanwhile, manganese oxides with various oxidation states are formed during that process. Different types of manganese oxides exhibit different activity in specific catalytic reaction. Kim et al. concluded that the catalytic activity for combustion of VOCs was in the order Mn_3O_4>Mn_2O_3>MnO_2[65]. However, Mn_2O_3 were considered as the active components in the CO and CH_4 oxidation process[66].

I.4.2.6 Nickel Oxide Based Sorbents

Nickel was in Lowell's list as a selection of metal oxide for SO_2 removal[28]. However, as an active species, nickel has not been extensively studied compared with sodium or copper[35]. It was used as either additives[67] or main active species[68,69] in SO_2 adsorption. Guo et al.[68] applied excessive impregnation method to prepare 1wt.% Ni on nitric acid treated activated carbon. They concluded that the acid-treated activated carbon could

significantly increase SO_2 removal ability, which might be due to the Ni and NiO species on the surface of activated carbon. Zhao et al.[69] synthesized a series of hydrotalcite-like compounds containing Ni and Al. It was summarized that the surface basicity and active oxygen species on the surface contributed to the high activity of sorbents for SO_2 adsorption. Furthermore, Zhao et al.[67] incorporate Cu into NiAl hydrotalcite compounds, concluding that the Cu-Ni solid solutions could induce the appearance of Cu-O pairs, which is favorable for SO_2 oxidation reaction. However, the performance of nickel oxide at higher temperature is not ideal based on the thermodynamic calculation. Most of the nickel oxide based DeSOx sorbents were used at room temperature or mild conditions.

I.4.2.7 Vanadium Oxide Based Sorbents

Vanadium oxide (V_2O_5) is known as its application for manufacture of sulfuric acid. It is also an efficient catalyst in SO_2 removal; however, high activity of V_2O_5 is usually operated in the temperature range of 400-600 °C. Therefore, V_2O_5-based sorbents in SO_2 removal were conducted at elevated temperatures[70,71]. In addition, when the temperature is too high (T> 600 °C), an intermediate $VOSO_4$ formed on the sorbent surface will decomposed into SO_2 and V_2O_5, which is a thermodynamic resistance. The reaction between SO_2 and V_2O_5 is listed as follows.

$$V_2O_5+2SO_2+1/2\ O_2 \rightarrow 2VOSO_4 \qquad \text{(I-15)}$$

Xiao et al.[70] concluded that SO_2 adsorption on V_2O_5/AC is comprised of four steps: (1) adsorption of SO_2 on V_2O_5 sites; (2) SO_2 activation by V_2O_5 and formation of $VOSO_4$ intermediate; (3) O_2 reacts with $VOSO_4$ to form SO_3 and V_2O_5; (4) SO_3 reacts with H_2O to

form H_2SO_4, which was stored in AC micropores. They also found that the high SO_2 removal ability was related to the properties of AC. Ma et al.[71] also reported that V_2O_5 supported on commercial AC was able to remove SO_2 and NO simultaneously around 200 °C. Dunn et al.[72] doped vanadia on various supports and determined that the rate of oxidation reaction is zero order with respect to oxygen (when P_{O2} is above 1 vol.%) and first order with respect to SO_2.

For the thermodynamic reason, V_2O_5 is not effective when the temperature is higher than 600 °C. At low temperature (T< 400 °C), its reaction rates is too low. According to Dunn's work, V_2O_5/TiO_2 can only reach less than 20 % conversion when the temperature of the system was lower than 400 °C[72].

I.4.3 Mixed Oxide Adsorbents on Different Support Materials

Various commercial supports, including activated carbons, SiO_2, Al_2O_3, TiO_2, and ZrO_2, are widely employed in industries[29]. Since activated carbon does not possess good thermal stability and the environment of SOFCs may cause degradation to the activated carbon based material, it was not chosen as a candidate in this study. Combining the excellent oxidation ability and high surface area properties of the as mentioned supports, the supported adsorbents are likely to possess high SO_2 adsorption capacity.

Many types of adsorbents possess excellent capacity and activity for SO_2 destruction ($DeSO_x$). Most of these adsorbents are supported transition metal oxides due to their high thermal stability, high surface area, and ease of regeneration[21]. The most common supports people use are γ-Al_2O_3, SiO_2, TiO_2, and ZrO_2. The advantage for these materials is firstly

these supports are cheap and widely used commercial products. For instance, γ-Al_2O_3 is a widely used product in catalysis, gas separation, liquid filtration or as coating material, which is usually generated by calcination of boehmite at 450-500 °C[21]. The second reason is that most of these porous materials are able to provide large surface area, which reduces internal mass transfer resistance. In this section, the materials used for SO_2 removal will be split into three categories:

1. Oxides supported on Alumina
2. Oxides supported on Titania
3. Other mixed oxide materials (e.g. porous silica, CeO_2, ZrO_2, HT-like compounds, spinels, etc.)

I.4.3.1 Oxides Supported on Alumina/Alumina Based Adsorbents

Copper oxide supported on gamma alumina is a traditional adsorbent for SO_2 removal. It is an excellent candidate for industrial application, such as flue gas desulfurization (FGD) process. CuO/ γ -Al_2O_3 can not only remove SO_x, but also NO_x from flue gas simultaneously[73,74]. Furthermore, this sorbents can be regenerated under a reductive atmosphere (CH_4, H_2, or NH_3) at c.a. 500 °C. The SO_2 capture and regeneration reaction are shown as follows:

Reaction: $CuO+ SO_2+1/2O_2 \rightarrow CuSO_4$ (t=350-400 °C) (I-16)

Regeneration: $CuSO_4+2H_2 \rightarrow Cu+SO_2+2H_2O$ (t=500 °C) (I-17)

$CuSO_4+1/2CH_4 \rightarrow Cu+SO_2+1/2CO_2+H_2O$ (I-18)

Macken et al.[73] prepared a series of CuO/Al_2O_3 adsorbents that can be reused up to 1500 cycles, and the capacity was only reduced by 25 %. Similarly, Jeong and co-workers[74] also used $CuO/\gamma\text{-}Al_2O_3$ to remove SO_2 in fluidized-bed reactor.

Ma and co-workers[75] studied the synergistic effect between NO_x and SO_2 for the adsorption and reaction on gamma alumina. They conducted TPD and *in situ* DRIFTS experiments and concluded that SO_2 (200 ppmv) could only form tetravalent sulfur species on alumina surface without NO_2 in air stream at 303 K. On the other hand, in the presence of NO, the TPD results clearly showed that S (VI) existed on the sorbent surface. As shown in Figure I.8A, the peak shown around 393 K corresponds to the desorption of weakly adsorbed aluminum sulfite species in the absence of NO; while, in Figure I.8B, the SO_2 desorption peak centered at 1223 K can be attributed to the decomposition of aluminum sulfate species. Similar results was also observed by other researchers[76,77], whose decomposition temperature for $Al_2(SO_4)_3$ was around 1205 K.

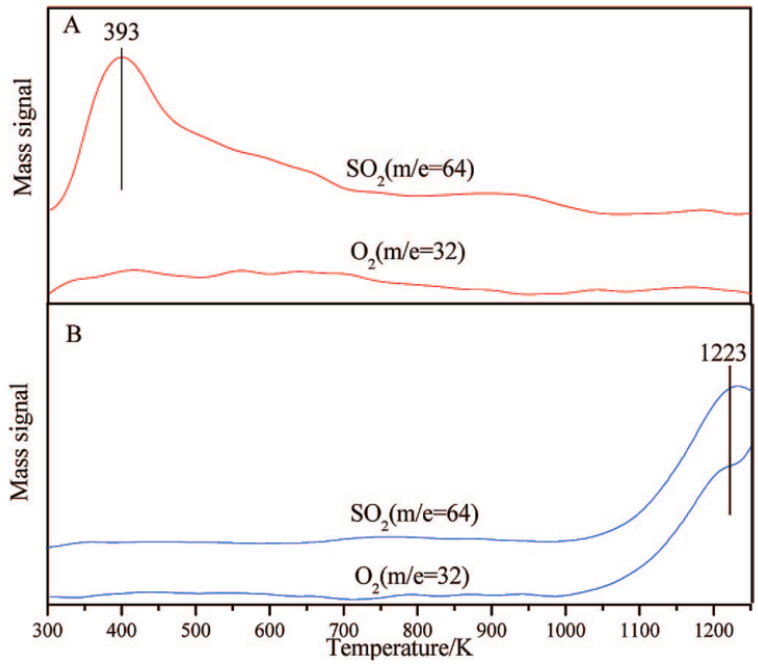

Figure I.8 TPD spectra of SO_2 and O_2 of gamma alumina reacted with SO_2 (200 ppmv) in air at room temperature (A) in the absence of NO and (B) in the presence of NO (200 ppmv).

Xue et al.[78] investigated Pt (0.1 ~ 5 wt.%) supported on gamma alumina about oxidation of NO and SO_2. With flow rate of 400 $cm^3 \cdot min^{-1}$, 50 ppmv of SO_2, 10 vol.% of O_2, and balanced in N_2, they optimized conditions and their materials could achieve 100 % conversion when the temperature was around 350-400 °C, and 2.0-5.0 wt.% Pt loading on alumina. In addition, Pt/Al_2O_3 was not a series of size-dependent materials. Eighteen years later, Hamzehlouyan et al[79] also used Pt/Al_2O_3 to oxidize SO_2 (varied between 100 and 149 ppmv) under a flow rate of 300 $mL \cdot min^{-1}$ in the temperature range of 350-400 °C. They primarily developed a Langmuir-Hinshelwood based model, which was able to predict the

experimental results of Pt/Al_2O_3 accurately. Their model shows that at low temperatures, SO_3 occupied the active sites required for oxygen adsorption, thus inhibiting SO_2 oxidation reaction. The model is demonstrated as follows:

$$SO_2(g)+Pt \rightarrow Pt\text{-}SO_2 \quad \text{(I-19)}$$

$$O_2(g)+2Pt \rightarrow 2Pt\text{-}O \quad \text{(I-20)}$$

$$Pt\text{-}SO_2+Pt\text{-}O \rightarrow Pt\text{-}SO_3+Pt \quad \text{(I-21)}$$

$$Pt\text{-}SO_3 \rightarrow SO_3(g)+Pt \quad \text{(I-22)}$$

Schreier and the co-workers[77] test various metal oxides supported on mesoporous Al_2O_3 in the temperature region of 50-600 °C. Among all that metal oxides, calcium and barium are the most effective components for SO_x removal. They stated that the optimized materials were able to remove about 97 % SO_2 in the stream (50 ppmv SO_2, 6 % O_2, and 5 % CO_2). In addition, Mn (acted as oxidant as well as sulfur storage element) and Na (additional storage component for sulfur) species based on alumina and calcium oxide supports further improved the SO_2 uptake. It is worth mention that the performance of the sulfur trap was improved to a large extent with the incorporation of 10 wt.% sodium, especially for the Ca-containing material.

I.4.3.2 Oxides Supported on Titania/Titania Based Sorbents

Titania (or Titanium dioxide) is the most widely used material used in chemical industry and oil refineries for SO_2 removal, typically through Claus reaction[80]. It is also well know that TiO_2 is a potential excellent photocatalyst material for environmental purification, such as organosulfur selective adsorption[81].

Ao et al.[82] applied TiO_2 (P25) coated on glass fiber filter as a photocatalyst to simultaneously remove SO_2, NO_x, and BTEX (benzene, toluene, ethylbenzene, and o-xylene) at trace level (ppb) concentrations. After the adsorption process, sulfate ion was generated upon the surface of TiO_2 glass fiber filter according to the ion chromatography results. They also stated that the sulfate ion occupied the adsorption sites on TiO_2 that intended to react with NO_x to form nitrate ion. Baltrusaitis et al.[83] further confirmed that the majority surface species after SO_2 adsorption on TiO_2 (4-32 nm nanoparticles) was adsorbed sulfite without light. Whereas, adsorbed sulfate was generated with UV/vis irradiation during SO_2 adsorption. Additionally, the sulfur species adsorbed was influenced by hydroxyl groups and molecularly adsorbed water, which was confirmed by XPS technique.

Rodriguez et al.[80] investigated the adsorption and reaction of SO_2 on Au supported on TiO_2 at room temperature. It was found that the gold nanoparticles deposited on TiO_2 (110) were capable of adsorbing and dissociating SO_2 with high activity. They also concluded that the dispersed gold nanoparticles promoted the activity of titania via facilitating the migration of oxygen vacancies from the bulk toward the titania surface.

I.4.3.3 Other Mixed Oxide Materials

There are many other types of materials to remove SO_2, such as spinels, hydrotalcite (HT)-like compounds. It was reported in literatures that the addition of various metallic oxides such as Ce, Cu, Co, V, Ni, and Fe into HT-like compounds prepared either by impregnation or co-precipitation is favorable for De-SO_x process[57,69,84–88].

Li et al.[89] synthesized silica-supported silver-based adsorbent to remove SO_2 for lean-burn diesel engine emission. The silver particles was capable of oxidizing SO_2 to SO_3, thereby forming Ag_2SO_4. The 5 wt.% Ag-SiO_2 adsorbent removed almost all of the SO_2 in gas stream and it could be fully regenerated around 300-550 °C.

Djamela et al.[63] studied SO_x adsorption on Pt/SiO_2 for SO_2 concentrations ranging from 10 to 50 ppmv at moderate temperatures (200-400 °C). By applying first principle calculations and in situ DRIFT, they proposed that SO_2 was firstly oxidized to SO_3 over Pt surface, as shown in Figure I.9. Then the SO_3 associated with surface hydroxyl groups, thus forming SO_4^{2-} species. This conclusion was further supported that no surface species are formed during blank SiO_2 experiments.

Cantú et al.[31] synthesized MgAlFe HT materials to remove the SO_2 from FCC units. All the materials were prepared by co-precipitation method. It was also mentioned that the materials they prepared outweighed a commercial product not only in adsorption capacity & rates, but also in reduction rates. It was believed that the incorporation of iron increased the reduction capability of the synthesized materials. Furthermore, the cerium was proved efficient in oxidizing SO_2 to SO_3, which is an important factor for SO_2 adsorption capacity.

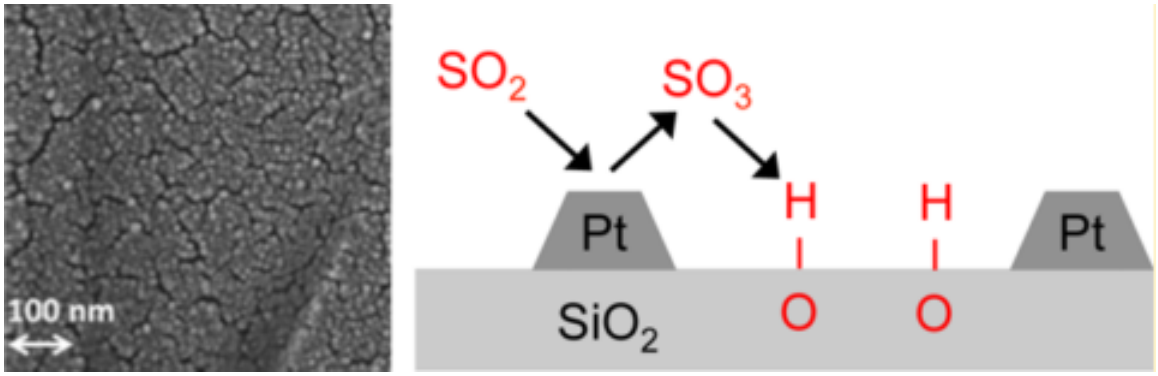

Figure I.9 Mechanism of SO_2 adsorbs onto Pt/SiO_2 surface[63].

Similar work has been done by Pereira et al.[57] using Mn/Mg/Al spinels with Ce incorporation. The researchers concluded that the Ce addition is beneficial for SO_x abatement as well as for the reduction of the sulfated materials. In addition, the best SO_2 adsorption capacity occurred when the sample was prepared with higher Al content.

Zhao et al.[69] synthesized a series of Ni-Al mixed oxides via urea hydrolysis method. In this work, it was proved that the SO_2 adsorption capacity increased with surface basicity and active lattice oxygen species of the materials. When the Ni/Al ratio was three, the surface exhibited highest basicity determined by CO_2-TPD technique. Meanwhile, the small pore size is also beneficial for SO_2 adsorption. Further study conducted by Zhao et al.[67] stated that the lattice oxygen on the surface (the basic sites) may associate with the SO_2 molecule, as shown in Figure I.10.

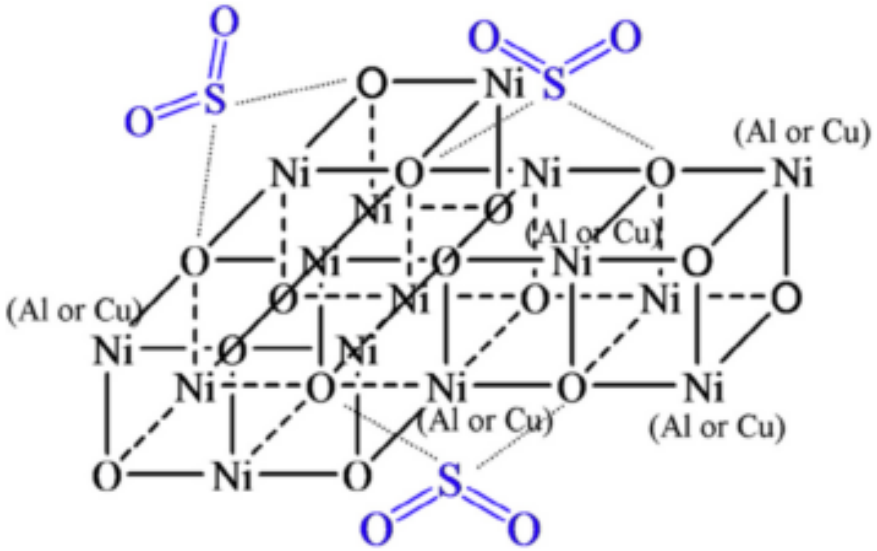

Figure I.10 Sulfur dioxide molecules interact with surface basic lattice oxygen sites[67].

.Tailor et al.[90] synthesized tertiary amine grafted pore-expanded MCM-41 to adsorb SO_2 in the presence of CO_2. This material possessed large saturation capacity, which was 208.6 $mg \cdot g^{-1}$ sorbent under dry conditions at room temperature. Furthermore, it can be fully regenerated at 130 °C in nitrogen atmosphere.

A study by Romano and co-workers[22] prepared a series of Ce-Zr mixed metal oxides (varying Ce/Zr molar ratios) and investigated the reaction mechanisms on the surface by XPS technique. They summarized that the performance of the materials enhanced at higher temperatures or higher Ce content. More importantly, the presence of surface hydroxyl groups or lattice oxygen atoms on the surface was a critical factor in the adsorption process

of SO_2. In addition, they proved that the surface hydroxyl groups could not be fully removed by heating the samples to 673 K under vacuum by analyzing O_{1s} peak.

Peterson et al.[91,92] used zirconium hydroxide (calcined at various temperatures) to remove 765 ppmv SO_2 at 25 °C under 15 % RH. X-ray photoelectron spectroscopy technique was used to quantify the amount of terminal hydroxyl groups and the SO_2 capacity was highly correlated to the percentage of terminal –OH.

Gaudin et al.[93] synthesized mesoporous silica impregnated with Cu and Ce as active metals to remove 250 ppmv SO_2 at 400 °C. It was reported that the CuO-CeO_2 supported on KIT-6 (mesoporous silica) exhibited the much better DeSOx performance than merely use Cu or Ce as active metals. This synergistic effect can be attributed to the high dispersion of CeO_2 particles and interactive electron transfers between Ce and Cu[93].

I.4.4 Oxides Supported on Carbonaceous Materials/Active Charcoal/Active Carbon Fibers

Active carbons are usually prepared starting from activation of coal, wood chip, coconut shell, lignite or biomass products, followed by impregnating with a solution of dehydrating agent, washing, drying, carbonizing in an inert atmosphere, and activating with CO_2 or H_2O[21,94]. They possess a great amount of micropores (pore size less than 2 nm), intricate pore structure, and high surface area (>500 $m^2 \cdot g^{-1}$), which are favorable for adsorption and surface reaction[95,96]. Also, active carbons have been widely used as support for SO_2 removal due to their relatively high efficiency and low cost compared with other materials[42,97–99].

Ma et al.[42] synthesized a series of regenerable AC adsorbents impregnated by $Fe(NO_3)_3$. They investigated effect of desulfurization temperature, regeneration temperature. The performance of 3.5 wt.% Fe/AC product outweighed AC or Fe_2O_3 to a large extent. Furthermore, this type of material can be fully regenerated in NH_3 atmosphere at 350 °C. Several years later, in contrast, Fu et al.[100] synthesized various iron oxides (without support) to deal with 96 ppmv SO_2 balanced in nitrogen and oxygen. According to their preliminary tests, α-Fe_2O_3 and γ-Fe_2O_3 demonstrated the best adsorption ability probably due to the effect of surface hydroxyl species on these iron oxides surface. However, due to the amphoteric properties of the metal surface, the SO_2 adsorbed onto the Lewis base sites tended to strongly interact with the oxygen atoms, thus resulting in chemisorbed sulfate derived from sulfite species rearrangement. Whereas, the SO_2 adsorbed on the Lewis acid sites leading to weakly adsorbed SO_2.

Lee et al.[97] doped KOH onto granular activated carbon (K-IAC) to remove SO_2. They claimed that K-IACs can uptake over 10 times more SO_2 than those of undoped activated carbons. Essentially, the adsorption process occurred because of the surface reaction between K_2SO_4 and H_2O. Moreover, they also investigated the effect of inlet gas concentration, effect of adsorption temperature, as well as linear velocity.

Bagreev and co-workers[98] studied the role of basic nitrogen containing groups (characterized by elemental analysis and XPS technique), basicity (determined by titration) and micropores (analyzed by N_2 physisorption technique) during the catalytic oxidation process. It was discussed that the quaternary and pyridinic type nitrogen observably

increased the adsorption capacity. Similarly, Mangun et al.[101] used ammonia treated ACFs to remove SO_2 from flue gas. It was proved that the incorporation of basic functional groups onto ACFs surface enhanced the adsorption capacity. Furthermore, the ACFs possess much lower pressure drop compared with the conventional granular activated carbons.

Qu and Liu[48,49] investigated the role of Mn species for SO_2 removal of Mn-based activated carbon sorbents. In their work, the Mn-based activated carbon sorbents were impregnated by ultrasound-assisted method by using $Mn(NO_3)_2$ as precursor. Assisted by the XPS technique, it was found that MnO, Mn_3O_4, and Mn_2O_3 were converted into MnO_2 after the SO_2 adsorption process. Additionally, nitric acid pretreatment could remarkably increase the content of surface oxygen functional groups, minimizing MnO grain size, thus improving the SO_2 adsorption capacity. In detail, it was explained that the oxygen in the gas phase firstly adhered onto the reductive manganese oxides, forming lattice oxygen. The lattice oxygen acted as a source of active oxygen in the reaction. As a result, SO_2 reacted with the active oxygen provided by the former step, thereby generating H_2SO_4 with the help of moisture[102]. The possible mechanisms at various temperature for Mn supported on AC are presented as follows:

$$Mn_2O_3+SO_2+H_2O\rightarrow 2MnO_2+H_2SO_4 \quad \text{(I-23)}$$

$$MnO+Mn_3O_4+3SO_2+3O_2+3H_2O\rightarrow 4MnO_2+3H_2SO_4 \quad \text{(I-24)}$$

$$MnO+SO_2+O_2+H_2O\rightarrow MnO_2+H_2SO_4 \quad \text{(I-25)}$$

In this work, since SOFCs are usually operated at elevated temperatures, activated carbon does not possess high thermal stability. Therefore, metal oxides may be good candidates to remove SO_2 in air stream.

I.5 Summary

To sum up, four types of sorbents are described in this Chapter. Because of the long operation time for fuel cells, we hope the breakthrough capacity can be as high as possible. On the other hand, to fully utilize the anode exhaust gas, which will be mentioned in detail in the following chapter, we can regenerate the spent sorbents. Usually, better regenerability means the sorbent is more environmental friendly. In addition, the operation temperature of SOFC is very high compared to other types of fuel cells, we also hope the sorbents can perform very well in a wide temperature range.

In Figure I.12, we can see that the regenerability of hydrotalcite materials is very poor, though they are efficient over a wide temperature range. The calcium based sorbents is fairly efficient at high temperature and the price is very low. However, because of their poor regenerability, it is not practical to use them in the fuel cell filters. Activated carbon is a commonly used sorbent for many applications. The price is affordable and the it can be regenerated multiple cycles. But the disadvantage is that it can only be used below c.a. 250 °C. Exposing activated carbon at high temperature in air can result in combustion. So the most practical sorbents are metal oxides.

Among the oxides of Ca, Ce, Cu, Fe, Mn, Ni, and V, MnO_x is the best candidate for SO_2 adsorption at a wide temperature range (RT~700 °C). According to the thermodynamic calculations, MnO_x has a high desulfurization equilibrium constant from room temperature to 700 °C. Although there are phase transformations occurred at high temperatures, the new phases (Mn_3O_4 or MnO) still possess high $DeSO_x$ ability compared to other metal oxides.

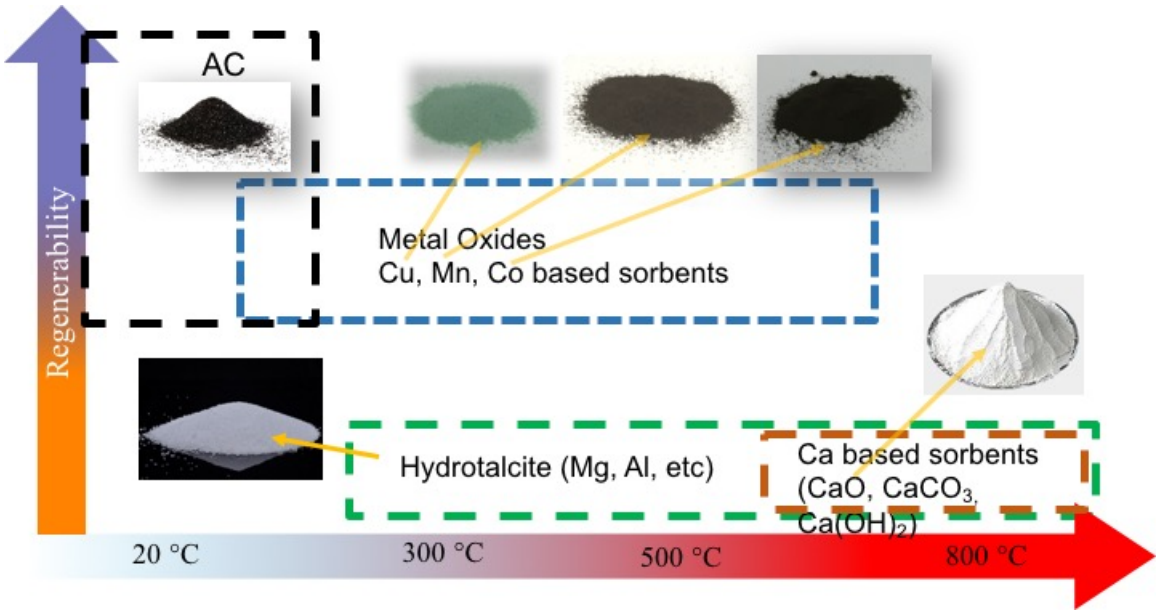

Figure I.11 Various types of SO_2 sorbents and their regenerability and most efficient working temperature.

The biggest issue for MnO_x is the high regeneration temperature for multi-cycle SO_2 adsorption use. However, the regeneration temperature can be decreased by incorporation of transitional metal promotors, such as Ce or Fe. Although manganese based sorbents have been studied by other researchers recently[48,49], there is few literature regarding deep SO_2

removal (< 10 ppmv SO_2 for the inlet) by Mn-containing metal oxides in the presence of high space velocity under a wide temperature range.

Additionally, the role of surface functional groups such as hydroxyl groups as well as the chemical state of manganese oxide (MnO_2, Mn_2O_3, Mn_3O_4, etc.) was investigated in this work. The possible SO_2 adsorption pathway on manganese-containing sorbents was proposed. Multiple characterization techniques were employed to study the physiochemical changes with various preparation approaches. At the same time, the adsorption/reaction mechanisms were also discussed based on the XPS and H_2-TPR results.

Chapter II Experimental Details

II.1 Adsorbent Preparation

In this study, γ-Al_2O_3 (493 $m^2 \cdot g^{-1}$, 0.68 $cc \cdot g^{-1}$) and SiO_2 (293 $m^2 \cdot g^{-1}$, 1.12 $cc \cdot g^{-1}$) were purchased from Sigma-Aldrich. TiO_2 (anatase phase, 150 $m^2 \cdot g^{-1}$, 0.42 $cc \cdot g^{-1}$) was obtained from St. Norpro Grade. ZrO_2 (105 $m^2 \cdot g^{-1}$, 0.33 $cc \cdot g^{-1}$) was purchased from Alfa-Aesar. $Mn(NO_3)_2 \cdot 4H_2O$, and HNO_3 were purchased from Alfa Aesar. The support was firstly crushed and sifted to the desired size. A series of supported MnO_x sorbents were prepared by impregnating γ-Al_2O_3 with corresponding metal nitrates dropwise under vigorous stirring at room temperature. Afterwards, the samples were dried on a hotplate at 323 K for at least 6 h, following aging at 383 K for overnight. The samples were further placed in a crucible with cover and calcined in the presence of stationary air at a desired temperature for 2 h by Lindberg/Blue furnace (Thermo Scientific Inc.). Various heating rates (5-20 K min^{-1}) were maintained up to the final calcination temperature. For comparison, adsorbents were prepared by impregnating γ-Al_2O_3 with HNO_3 as well. $Mn(NO_3)_2$ was completely decomposed after calcination since there was no N_{1s} signal in the survey scan during XPS analysis. All the samples were stored in airtight vials and put in a desiccator until breakthrough test.

II.2 Adsorbent Breakthrough Tests

Breakthrough tests were carried out to evaluate the breakthrough capacity (B.T. Cap.) and breakthrough time for SO_2 removal. Unless specified otherwise, all gases were

purchased from Airgas South (Opelika, AL). The SO_2 source is 50 ppmv balanced in N_2 with ± 5% uncertainty from Airgas Inc (Durham, NC). The adsorbents (ca. 50 mg) were packed into a quartz tubular reactor (4.0 mm I.D). The sorbent bed was supported by quartz wool on both sides (shown in Figure II.1). The reactor was heated by a Thermolyne tubular furnace, whose temperature was measured by a K-type thermocouple attached to the packed bed. Unless elsewhere stated, the breakthrough tests were maintained under the following conditions: SO_2 inlet concentration 10 ppmv, atmospheric pressure, total flow rate 1000 mL min^{-1}. The adsorbent was pretreated at 250 °C for 60 min in UHP nitrogen at a feed of 200 mL min^{-1} for surface cleaning. Subsequently, the reactor was disconnected from the system by switching off the valves at upstream and downstream. Prior to each test, the upstream concentration was monitored for at least 30 min to ensure a constant SO_2 source was generated. Breakthrough experiments were carried out by switching to SO_2 challenge gas. The outlet SO_2 concentration was monitored by MultiRAE pro (shown in Figure II.2) equipped with SO_2 sensor (RAE Systems, CA), whose detection limit can be as low as 5 ppbv. For each sample, the breakthrough test was repeated at least twice.

The total SO_2 uptake capacities are calculated as follows:

$$C_{ads}=\frac{\int_{to}^{tads}(Co-C)dt}{mads}$$

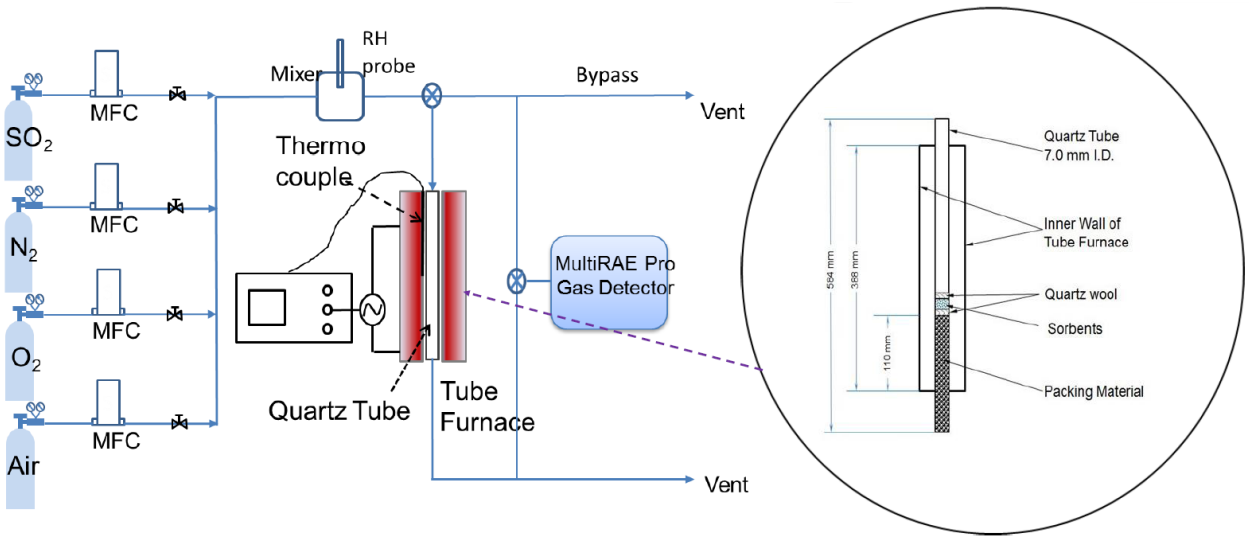

Figure II.1 Schematic of a bench scale unit for SO_2 adsorption test.

Figure II.2 MultiRAE Pro gas detector (RAE system).

II.3 Adsorbent Characterization

II.3.1 Physical Properties

The surface area, pore volume and pore size distribution of adsorbents were measured by nitrogen adsorption-desorption analysis at its normal boiling point (77 K) with a Quantachrome Autosorb-1. The samples were outgassed at 473 K for at least for 5 h under vacuum prior to physisorption measurements, if not otherwise noted. The surface area (S_{BET}) was calculated by the BET method; total pore volume (T.P.V.) was obtained at the point of 0.995 p/p^o; the pore size distribution was calculated by applying the BJH method on the desorption branch of isotherm curve.

X ray powder diffraction (XRD) patterns were obtained on a D8 ADVANCE powder diffractometer (Bruker, Germany) in a 2θ range of 20-70° with a step size of 0.02° using Cu Kα radiation (λ=1.5406 Å, 40 kV, 40 mA). The grain sizes of dispersed metal oxides were estimated by applying Debye-Sherrer equation.

II.3.2 Temperature Programmed Technique

Temperature-programmed reduction in hydrogen (H_2-TPR) analysis was measured in a 4 mm I.D. straight quartz tube. Before analysis, 100 mg of powder sample was loaded above a small amount of quartz wool and pretreated at 523 K for 1 h under 50 mL min^{-1} (controlled by an Alicat Scientific mass flow controller) ultra-high purity (UHP) argon flow to remove the moisture and physisorbed gases. After sample was cooled down to room temperature, the reduction gas mixture (5% H_2 in argon, 50 mL min^{-1}) was shifted. Effluent moisture during reduction was trapped in isopropanol slurry (195 K). The H_2 consumption

was recorded ramping from 303 K to 1123 K (β = 10 K min^{-1}) by online gas chromatograph (SRI 310C) equipped with thermal conductivity detector (TCD). The amount of hydrogen uptake was calibrated by CuO standard sample (99.9995%, Alfa Aesar).

Temperature programmed desorption of oxygen (O_2-TPD) were also conducted in a quartz tube with the same dimension used in H_2-TPR. Approximately 200 mg sample was placed into the tube. Then it was also pretreated under UHP helium flow (50 mL min^{-1}) at 523 K for 1 h. After that, the sample was cooled naturally with the helium flow until at room temperature. The amount of oxygen desorbed was recorded by the GC-TCD from 373 to 1123 K as described in H_2-TPR section.

II.3.3 X-ray Photoelectron Spectroscopy

X-ray photoelectron spectroscopy (XPS) spectra were recorded on an Axis Ultra spectrometer (Kratos Analytical, UK) with monochromatic Al Kα (1486.6 eV) radiation as the excitation source. The X-ray source was operated at 15 kV and 15 mA. Low energy electrons were applied to neutralize the sample. Before each analysis, the powder samples were grinded and pressed into thin disc. Afterwards, the resulting samples were dried overnight in a convection oven at 110 °C. Then, the samples were immediately placed into a vial until test. Before transferring the samples into a loadlock, the thin sheet-sized samples were firmly placed on carbon tape. Charging effects of samples were corrected by setting the binding energy of adventitious carbon (C1s) at 284.6 eV. The spectra were recorded with analyzer pass energy of 160 and 20 eV for survey (step size = 1.0 eV) and

high-resolution spectra (step size = 0.1 eV), respectively. The spectra were fitted by applying XPSPEAK software (Version 4.1) with Shirley-type background subtraction and Lorentzian (20 %)-Gaussian (80 %) decomposition parameters.

II.3.4 Oxygen Chemisorption

Oxygen chemisorption was applied to measure the dispersion of manganese on the support surface. Chemisorption measurement was performed at 250 °C on Quantachrome Autosorb-1 using volumetric method[103]. Oxygen uptake was measured by following a series of *in situ* pretreatment (Table 1).

Table II.1 Pretreatment for Mn supported adsorbents for oxygen chemisorption

Pretreatment step	Temperature (°C)	Operational condition	Time (min)
Surface cleaning	120	Flow helium, evacuate under vacuum	60
Surface reduction	250	Flow hydrogen	120
Physically adsorbed hydrogen removal	250	Evacuate under vacuum	30

The monolayer oxygen uptake was determined by extrapolating the high pressure region of combined isotherm line (including physisorption and chemisorption) to zero pressure, assuming that at zero pressure the amount of physisorbed oxygen is negligible. The adsorption stoichiometry was assumed to be 2 according to the literature has been described elsewhere[62,104].

II.3.5 Infrared Spectroscopy

The adsorbents were also investigated by Infrared Spectroscopy (Perkin Elmer spectrum 400 FT-IR/FT-NIR Spectrometer, USA). For each sample, c.a. 1-2 mg of finely grounded adsorbent was pressed into wafers. The wafers were loaded into a cell and preheated at 250 °C under vacuum atmosphere for 1 h. After that, the samples were naturally cooled down to room temperature. Prior to measurement, the background spectra were collected (600-4000 cm^{-1}) in the absence of samples. Then, the background spectra were subtracted from the sample spectra. It is worth mention that all the spectra were recorded with a resolution of 4 cm^{-1} and with an accumulation of 32 sweeps.

II.3.6 Composition Analysis for Adsorbents

The manganese content in the adsorbents was determined by using an AAnalyst 400 atomic absorption spectrometer (Perkin Elmer, USA) operated by Hazen Research, Inc. The sample preparation steps are listed as follows:

(1) Approximately 100 mg of each sample was weighed and transferred into a Teflon beaker;

(2) The samples were dissolved with 5 mL each of HCl, HNO_3, $HClO_4$, and 2 mL of HF to moist salts;

(3) The resulting salts were heated with 50 mL of 50 % HCl to redissolve the salts;

(4) The solutions were cooled naturally and then diluted to 100 mL with DI water;

(5) Any possible insoluble residue was filtered by filter paper.

Chapter III Sulfur Dioxide Adsorption by Manganese Supported Adsorbents for SOFCs Cathode Protection– Optimization and Characterization

III.1 Screening of Various Active Species for SO_2 adsorption

Literature mentioned that the incorporation of various metallic oxides such as Mn, Ce, Cu, Co, Fe, V to HTLC either by impregnation or co-precipitation as the best way to generate the mixed oxides for $DeSO_x$ process[57]. The preliminary SO_2 breakthrough data were collected at room temperature by conventional dynamic test method. Fe, Co, Ni, Ag, and Mn were transition metals supported on commercial γ-Al_2O_3. In each test, 2 ppmv SO_2 source at a face velocity of 133 cm s^{-1} passed through a packed bed containing ca. 100 mg of adsorbent. The breakthrough point was defined at 0.1 ppmv. The calculated breakthrough capacities are shown in Figure III.1. All of the adsorbents were crushed and sieved to the same particle size range prior to breakthrough test.

Most transition metal oxide doped sorbents exhibited higher breakthrough capacity than BASF commercial sulfur removal sorbent. It was observed that Mn dopant exhibited the highest SO_2 capacity of 8.73 mg SO_2/g sorbent, which was twice as much as BASF sorbent (3.26 mg SO_2/g sorbent). The capacity of Ag-doped alumina and Ni-doped alumina ranked as second and third place at room temperature, respectively. Essentially, for the adsorption process, the active metal oxides dispersed on the surface of support oxidized

SO_2 to SO_3, prompting the formation of corresponding metal sulfates[78,105]. Thermodynamically, the nano-dispersed MnO_x and Ag_2O particles are able to oxidize SO_2 with less effort since they possess much larger equilibrium constant than the others. Another possible explanation is that the incorporation of Mn or Ag can increase surface oxygen (O_{suf}) ratio, which is an important factor for oxidation ability[106].

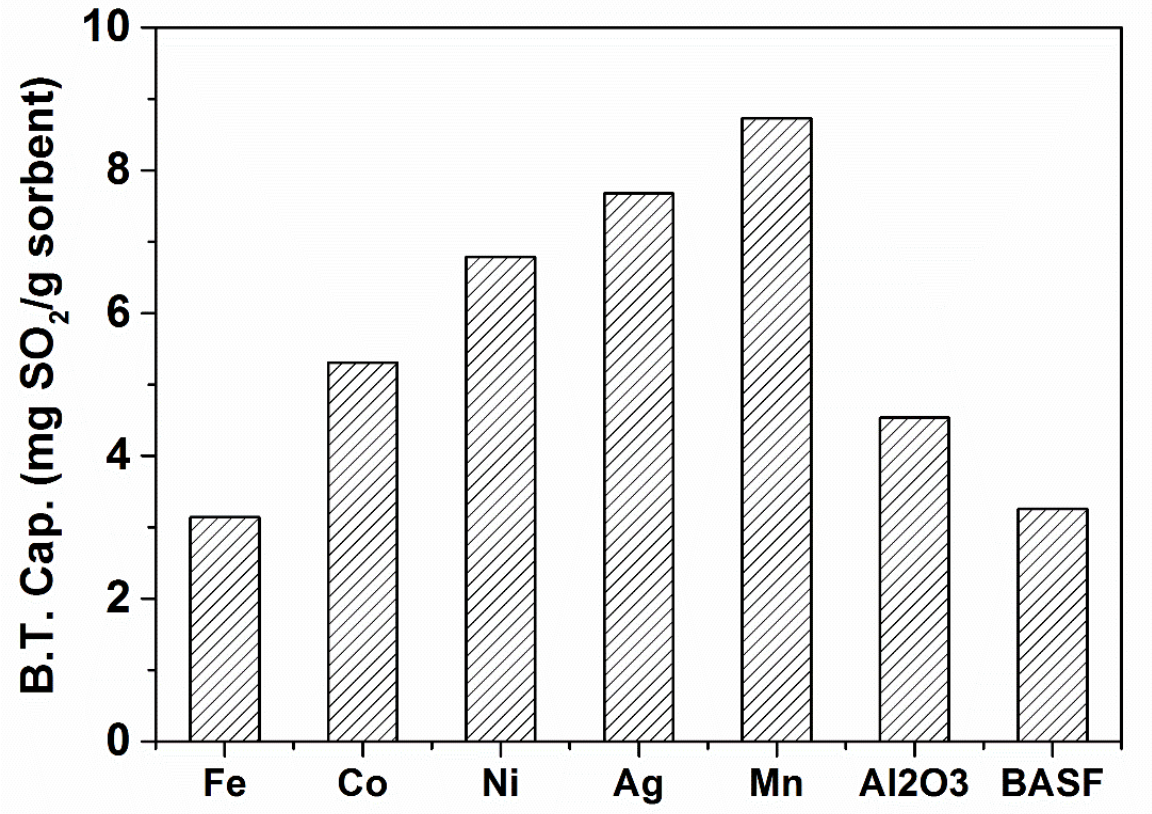

Figure III.1 Breakthrough capacities of 5.0 wt.% transition metal ions supported on γ-Al_2O_3 tested with 2 ppmv SO_2 at room temperature (Commercial BASF SG 9201 adsorbent listed as comparison).

It was also shown in Figure III.1 that the addition of Fe was not a suitable candidate for SO_2 removal. As reported earlier, incorporation of iron enhanced reduction capability of alumina based sorbents while sacrificed its adsorption capacity to a certain extent[31,42]. In terms of industrial application, manganese was applied in this work because of its relatively low expense and high breakthrough performance. To elucidate the role of manganese oxide for oxidative adsorption, several aspects of the binary system need to be characterized such

as the Mn loading on the surface with respect to average oxidation state, surface morphology, and the presence of surface oxygen among others.

III.2 Effect of Manganese Loading

In the previous section, all the metal loadings were kept at 5.0 wt.% and manganese turned out to be the most promising candidate. However, since it is well known that metal loading affects its dispersion, average oxidation state, and interaction with the support, MnO_x/Al_2O_3 adsorbents with various loadings between 2.5 and 10 wt.% were prepared by incipient wetness impregnation method and their SO_2 breakthrough performances are displayed in Figure III.2. Obviously, 5.0 wt.% Mn supported on γ-Al_2O_3 exhibited the best performance. There was marginal capacity loss at lower or higher loadings. These results suggest that 5 wt.% is the optimal Mn loading if manganese nitrate is used as precursor of MnO_x. The reasons why this certain amount of manganese loading exhibited the best breakthrough performance are explained in terms of surface area, oxidation state, and active metal dispersion in the following section.

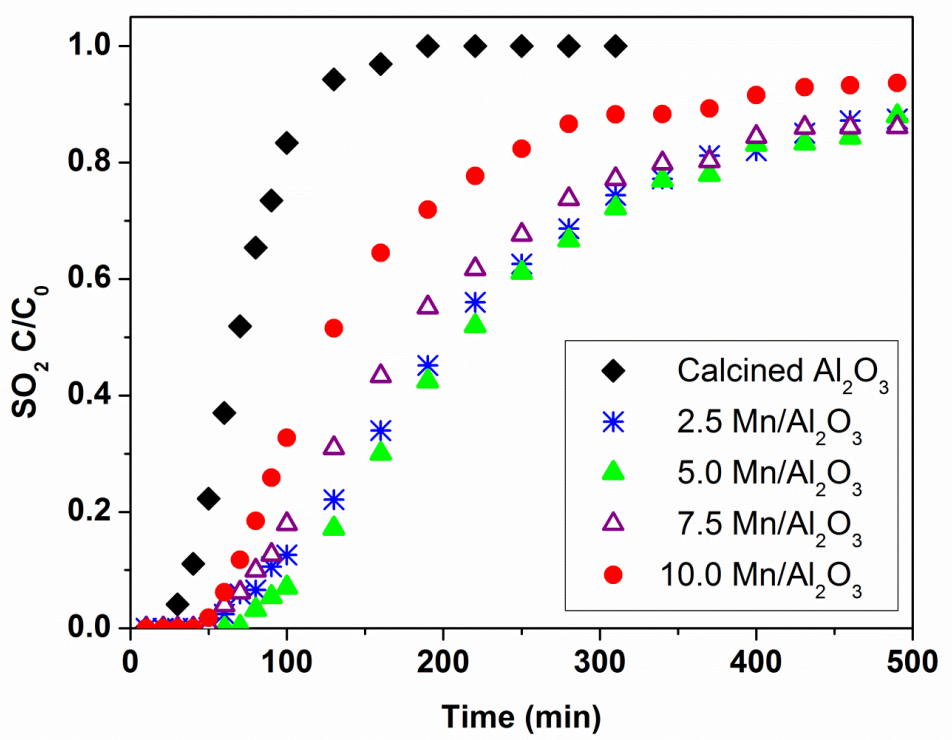

Figure III.2 Breakthrough performance of calcined Mn/Al_2O_3 sorbent with various Mn loading between 2.5 wt.% and 10.0 wt.% for 2 ppmv SO_2 at room temperature. Total flow rate: 1000 $mL \cdot min^{-1}$.

III.3 Characterization of Various Manganese-containing Adsorbents

X-ray powder diffraction analysis in Figure III.3 was carried out to characterize the MnO_x crystallite sizes with respect to different Mn loadings calcined at 550 °C. The diffraction peaks at $2\theta = 23.3^o$, 33.0^o, 38.3^o, 49.5^o, 55.2^o, and 65.9^o are ascribed to Mn_2O_3 phase (JCPDS 65-7467). However, in this case, when the samples were calcined at 550 °C, Mn_2O_3 was not well crystallized, and the only observable phase is Mn_2O_3 (222). The peaks of diffractograms at 28.6^o, 37.4^o, 42.8^o, 56.7^o, and 59.4^o correspond to MnO_2 phase (JCPDS 24-0735). The MnO_2 peaks intensity increased gradually with increasing Mn loading, indicating the buildup of MnO_2 phase on the support material. The XRD patterns of 2.5 wt.% Mn loading reveal that manganese oxides are presented in finely dispersed nanoparticles, which may located onto the inner wall of porous structure. Also, this is a significant indication that manganese was in a highly dispersed state or the MnO_x crystallites generated are less than 5 nm[62]. The sharp diffraction peaks with smaller FWHM for the 10 wt.% Mn loading are ascribed to the existence of well crystallized MnO_2 and Mn_2O_3 phases.

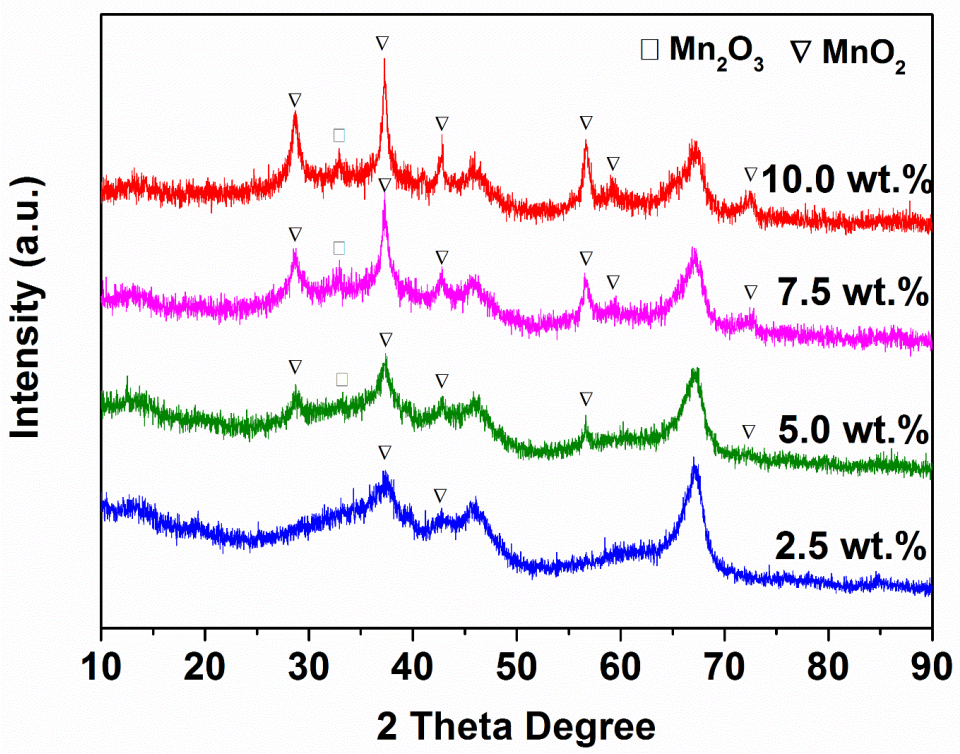

Figure III.3 X-ray diffraction patterns of various Mn loading.

Table III.1 Crystallite size, structural parameters of calcined Mn/Al_2O_3 adsorbents

Mn loading (wt.%)	Surface area[a] ($m^2\ g^{-1}$)	Pore volume[b] ($cm^3\ g^{-1}$)	Crystallite size[c] (nm)	
			MnO_2	Mn_2O_3
2.5	370	0.62	5.6	-
5.0	351	0.60	7.3	12.7
7.5	326	0.54	10.0	14.3
10.0	279	0.47	12.3	19.9

a. Surface area was calculated by BET method, in p/p^o range from 0.05 to 0.35.

b. Total pore volume was determined at p/p^o value of 0.995.

c. Grain size was calculated using Scherrer equation.

Table III.2 Surface properties determined by O_2-chemisorption

Mn loading (wt.%)	O_2 uptake (μmol g^{-1})	Metal surface area ($m^2\ g^{-1}$)	Dispersion (%)	Average crystallite size (nm)
γ-Al_2O_3	7.1	-	-	-
2.5 (2.78)	126.4	10.9	49.9	2.1
5.0 (5.98)	170.5	14.7	37.5	2.8
7.5 (8.93)	252.8	21.7	31.1	3.3
10.0 (9.95)	270.7	23.3	29.9	3.5

The surface morphology parameters of the as-synthesized and calcined Mn/Al_2O_3 samples are summarized in Table III.1. The BET surface area and pore volume decreased monotonically with increasing loading of manganese, which follows a conventional trend for impregnated sorbents. For the active species on the supports, the higher the Mn loading, the larger the crystallite size for both Mn_2O_3 and MnO_2.

Because of the limitation for XRD to detect crystallite size smaller than 5 nm, various Mn/Al_2O_3 samples were further examined by O_2 chemisorption technique. The results are listed in Table III.2. It is shown that the average crystallite size increased from 2.7 to 4.8 nm while dispersion decreased from 34.5 % to 19.5 % when the Mn loading increased from 2.5 to 10.0 wt.%. It is noteworthy that for 2.5 and 5.0 wt.% Mn loading, the metal dispersion as well as the manganese crystallite size was almost the same. In addition, because of higher metal loading results in more active metal surface area (active sites) for adsorption, the breakthrough performance of 5 wt.% outweighed that of 2.5 wt.%. However, further increasing metal loading basically causes the agglomeration of manganese particles, thus reducing the active metal dispersion significantly[13,62,107]. As a result, despite the increase in active metal surface area with higher metal loading, there was a continuous loss in SO_2 breakthrough capacity. The results imply that the SO_2 breakthrough capacity is related to the "highly dispersed" active metal surface area. The larger crystallite size may not be the ideal adsorption sites for SO_2 removal or the sites possibly were blocked by the larger Mn crystallites[13]. In other word, smaller crystallites possess much higher surface concentration of reactive sites. Generally, the chemisorption

results are consistent with the XRD results and can explain the breakthrough trend in Figure III.2 that the breakthrough capacity of the adsorbents increased in the order of $2.5Mn/Al_2O_3$ $<10Mn/Al_2O_3$ $<7.5Mn/Al_2O_3$ $<5.0Mn/Al_2O_3$. Some other possible factors such as surface oxygen amount and the ratio of $Mn^{4+}/(Mn^{4+}+Mn^{3+})$ are under further investigation.

Table III.3 H_2-TPR summary of MnO_x/Al_2O_3 samples

Mn loading (wt.%)	T (°C)			H_2 consumption μmol·(g sorbent)$^{-1}$	AOS of Mn
	T_1	T_2	T_3		
2.5	243	442	725	259	3.30
5.0	372	450	738	393	3.76
7.5	381	455	752	738	3.92
10.0	398	478	780	1154	3.84

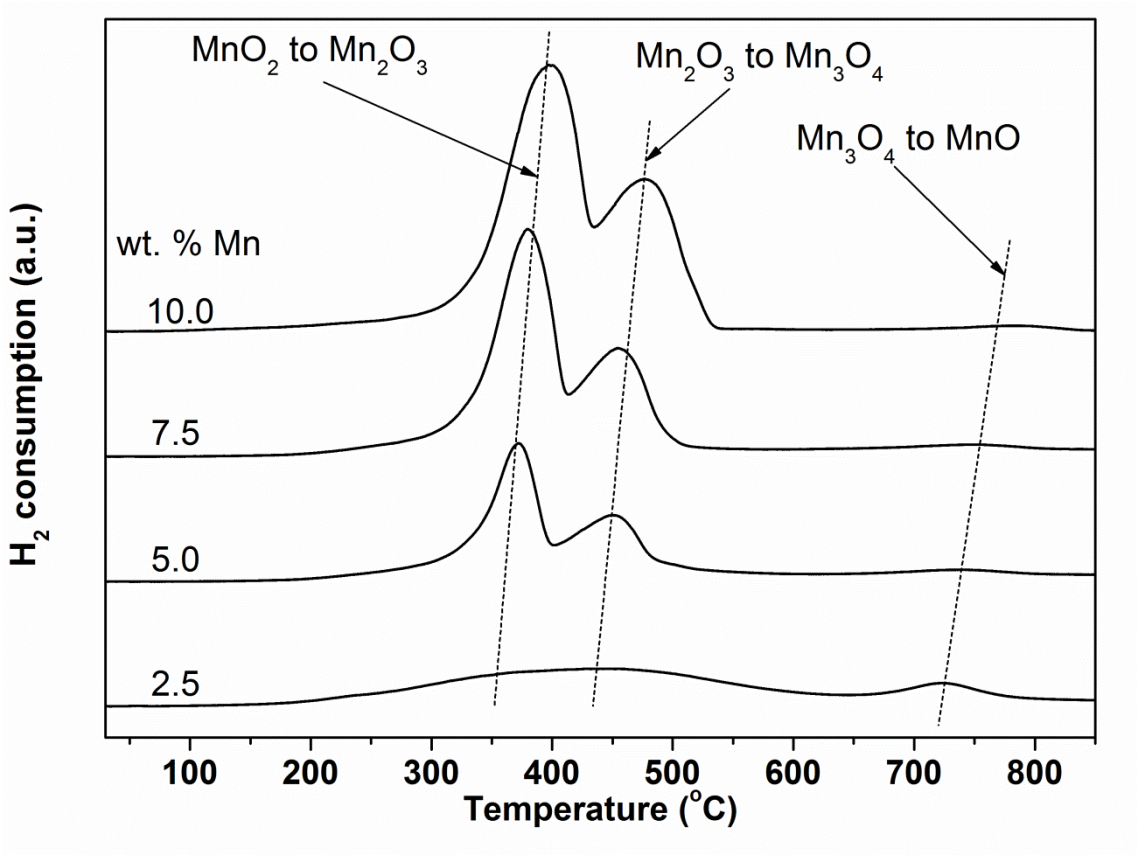

Figure III.4 H_2-TPR patterns of calcined $MnOx/Al_2O_3$ samples.

H_2-TPR was applied in this work to study the O/Mn ratio of various loadings of manganese deposited on the γ-Al_2O_3 support and relate the O/Mn ratio values to breakthrough performance of the adsorbents. The profiles of different Mn/Al_2O_3 samples as well as barely alumina support are presented in Figure III.4. The reduction peaks (T_i), integral H_2 consumption, and the O/Mn ratio are summarized in Table III.3. It is worth mention that the O/Mn ratio was converted from hydrogen consumption of each sample, assuming that MnO was the final product after reduction for thermodynamic reason[55,103,108–110]. After H_2-TPR experiment, the sample color converted from black to green, which is in accordance with the color of bulk MnO[111]. According to literatures, the stepwise reduction process of Mn deposited on alumina is considered to be: $MnO_2 \rightarrow Mn_2O_3 \rightarrow Mn_3O_4 \rightarrow MnO$[59,104,112]. Correspondingly, three-step reduction patterns occurred for all of the supported adsorbents. The first two peaks are ascribed to the reduction of $MnO_2 \rightarrow Mn_2O_3$ and $Mn_2O_3 \rightarrow Mn_3O_4$, respectively. These two peaks are distinct and clear, while the third peak is weak and broad, which is possibly attributed to the complete reduction of the remaining Mn_3O_4 to MnO. In Figure III.4, the peak temperature of lower Mn loading for reducing the dispersed MnO_x is lower than that of higher Mn loading (the peak temperature values are listed in Table III.3), suggesting that the former sample is easier to be reduced compared with the latter one. A plausible explanation could be due to the effect of smaller crystallite size, being more easily accessible to hydrogen[107]. In other words, highly dispersed manganese oxide species on support can be more easily reduced than bulk MnO_x particles[113]. This is in agreement with the XRD and O_2 chemisorption results.

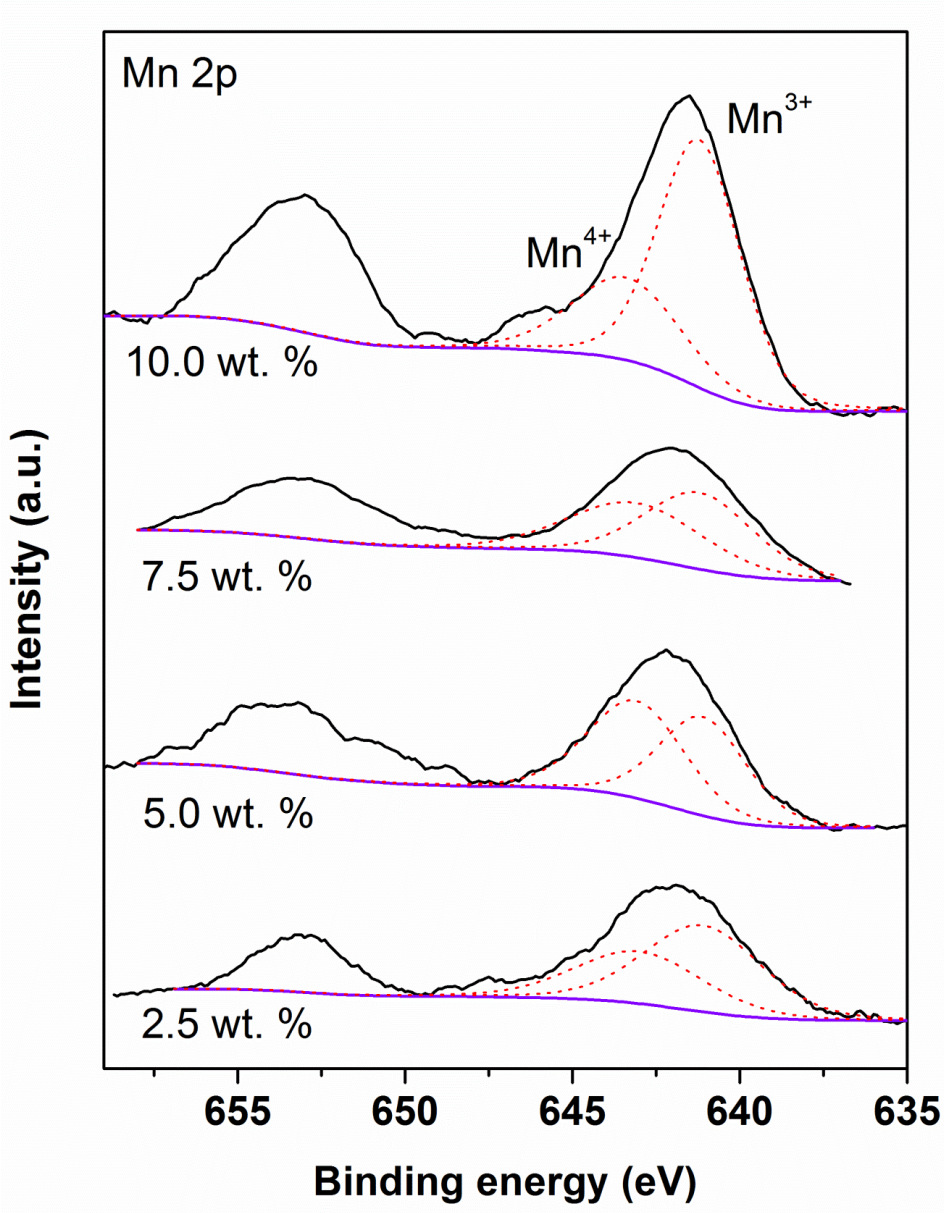

Figure III.5 XPS Mn 2p spectra for various Mn loading supported on Al_2O_3.

The sorbents of Mn supported on γ-Al_2O_3 (Sigma-Aldrich) were further applied to investigate the surface chemical states of Mn species. Figure III.5 shows Mn 2p spectra for various Mn loadings, displaying two peaks centered at about 642 eV and 653 eV for Mn $2p_{3/2}$ and Mn $2p_{1/2}$, respectively, which agrees with the values reported elsewhere[108,114,115].

III.4 Effect of Support Materials

III.4.1 Breakthrough Performance of Various Supported Manganese-containing Adsorbents

As described in the previous chapter, 5 wt.% manganese doped on γ-Al_2O_3 exhibited the best performance for low concentration SO_2 removal. Other than γ-Al_2O_3, some other supports, such as TiO_2[72,80,116], ZrO_2[22,78,116], SiO_2[105], were proved to be promising materials applied in SO_2 abatement. Unlike activated carbons, alumina, zirconia, and titania supported materials are all appeared to be of high activity and thermal stability[113]. High thermal stability prevents the adsorbents from deactivating or sintering since the SOFCs operation temperature is much higher than any other types of fuel cells.

In can be observed in Figure III.6 that manganese supported on silica showed negligible capacity for SO_2 at room temperature. Similar results was observed by other researchers[117]. The silica based adsorbent saturated (reached C/C_o=1.0) in less than 30 min. In contrast, other commercial available supports exhibited much higher breakthrough and saturation capacity for SO_2 adsorption, especially for γ-Al_2O_3. Xue et al.[78] examined platinum

supported on three different types of supports. It was stated that the SiO_2 support contributes very little to the SO_2 adsorption on the Pt-containing materials. The main active sites are Pt sites of Pt/SiO_2[78]. It was also explained that SiO_2 is known as an inert material and the intrinsic activity contributed by Pt was not altered by this support[78]. Wachs stated that the maximum monolayer surface coverages of the surface metal oxides on silica are approximately one tenth compared to other oxide supports (e.g. Al_2O_3, TiO_2, ZrO_2, Nb_2O_5, etc.)[118]. Typically, for the group V-VII transition metal oxides, the monolayer surface coverage of silica is 0.1-0.7 atoms/nm^2; whereas the monolayer surface coverage of other supports is around 4-5 atoms/nm^2. Wachs also indicated that silica is not able to hold the surface metal oxide species very strongly since the surface metal oxide species would migrate from silica to other oxide support if silica is physically mixed with other supports. Hence, the surface metal oxide species tend not to be isolated or dispersed well on the supports, which is not favorable for the adsorption process.

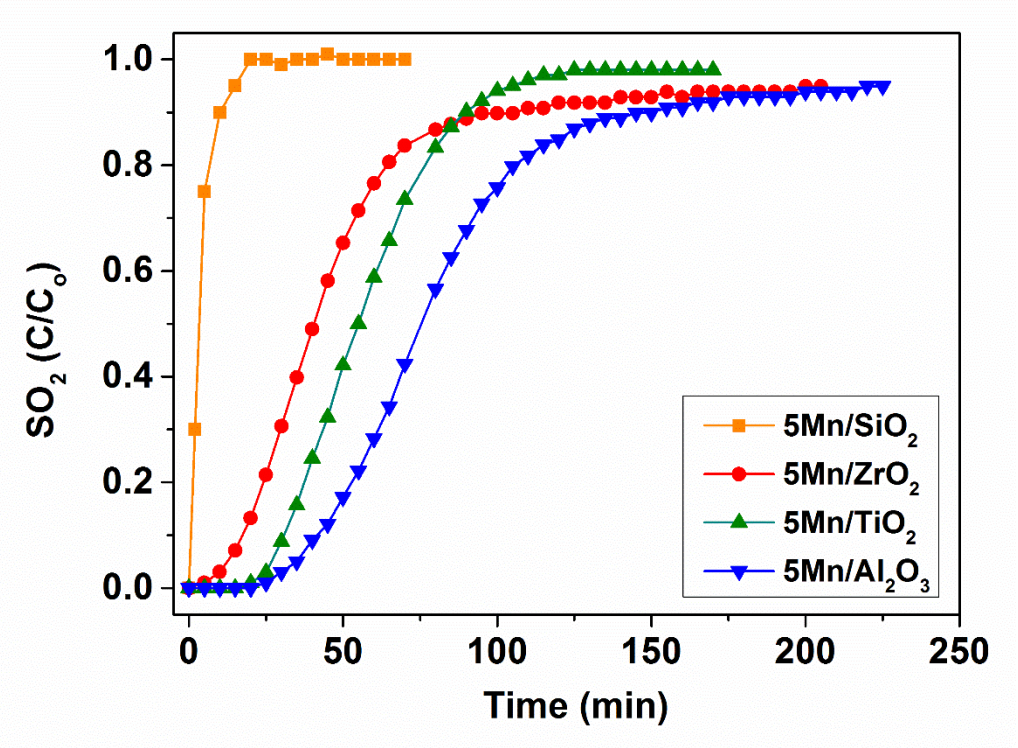

Figure III.6 Breakthrough curve of 5 wt.% Mn supported on various supports. Adsorption conditions: 10 ppmv SO_2, room temperature, 1000 mL min^{-1}.

However, other factors, such as the population of surface hydroxyl groups, and surface chemisorbed oxygen, were not discussed. It was reported in literature that both the surface hydroxyl groups and lattice oxygen are potentially important active sites for SO_2 adsorption on metal oxides[22,83,117,119–122]. Waqif et. al[116] reported that the OH spectra (~3630-3650 cm^{-1}) observed by FTIR were diminished by sulfate formation. Furthermore, Peterson and co-workers[92] revealed that the loss of terminal hydroxyl groups caused by calcination is highly related to the SO_2 removal capacity. The proposed mechanisms for SO_2 reacting with hydroxyl groups and lattice oxygen are listed as follows[123]:

$SO_2(g)+OH^- \rightarrow HSO_3^-$

SO_2 directly interacts with isolated hydroxyl groups to yield bisulfite on the surface of material

$SO_2(g)+2OH^- \rightarrow SO_3^{2-}+H_2O$

SO_2 simultaneously reacts with two hydroxyl groups in close proximity, generating adsorbed water at the same time.

$SO_2(g)+O^{2-} \rightarrow SO_3^{2-}$

However, this reaction plays a less important role in SO_2 adsorption[83]. It was also reported that the surface oxygen atoms are less reactive compared to hydroxyl groups toward sulfur dioxide[119]. Goodman et al. summarized that only O^{2-} with low coordination number (the O^{2-} exists at steps and kinks) is able to react with SO_2[120].

Apart from the reasons stated above, some other important factors, such as the oxidation state of MnOx, are explained in the following part.

III.4.2 Characterization of Various Supported Manganese-containing Adsorbents

III.4.2.1 Temperature Programmed Reduction

The H_2-TPR results were demonstrated in Figure III.7. For each profile, there are two prominent peaks. Similarly, as stated in Figure III.4, these two peaks are attributed to the stepwise reduction of highly dispersed MnO_x to MnO. For Mn/γ-Al_2O_3, there is a broad small peak centered at 673 °C. This high temperature peak can be ascribed to Mn^{3+}-O-Al

(solid solution) species and interact strongly with the alumina surface[55]. Likewise, as manganese supported on ZrO_2, the broad peak centered at 458 °C with a shoulder at 518 °C may be attributed to Mn^{3+}-O-Zr. Compared with Mn/γ-Al_2O_3, all of the reduction peaks shifted to the lower temperature region, which indicates ZrO_2 is capable of enhancing the reducibility of the supported MnO_x. In addition, the peak shoulder existed around 200 °C may be responsible for reduction of surface OH groups.

Table III.4 Content of MnO_2 and Mn_2O_3 for 5wt.% Mn on various supports

Sample	Peak1/Peak2	MnO_2 (wt.%)	Mn_2O_3 (wt.%)
5Mn/γ-Al_2O_3	1.05	37.1	62.9
5Mn/TiO_2	1.30	45.9	54.1
5Mn/ZrO_2	1.56	54.6	45.4
5Mn/SiO_2	1.65	57.5	42.5

Since the first reduction peak is attributed to MnO_2 to Mn_2O_3 and the second peak is Mn_2O_3 to Mn_3O_4, based on the stoichiometry of reduction reaction, the relative content of MnO_2 and Mn_2O_3 can be determined. Herein, we assume there is no Mn_3O_4 or MnO species in the compound, given no corresponding Mn_3O_4 or MnO peaks on the XRD profiles of these materials (not shown). The peak ratio, content of MnO_2 and Mn_2O_3 are listed in Table III.4. The Mn_2O_3 content of various samples from high to low is in the order: 5Mn/γ-Al_2O_3

> 5Mn/TiO_2 > 5Mn/ZrO_2 > 5Mn/SiO_2. Since Mn_2O_3 possess higher equilibrium constant toward SO_2 compared with MnO_2 based on the thermodynamic calculation, it is more feasible for Mn_2O_3 to the remove the SO_2 in air. Therefore, higher Mn_2O_3 ratio corresponds to higher breakthrough performance.

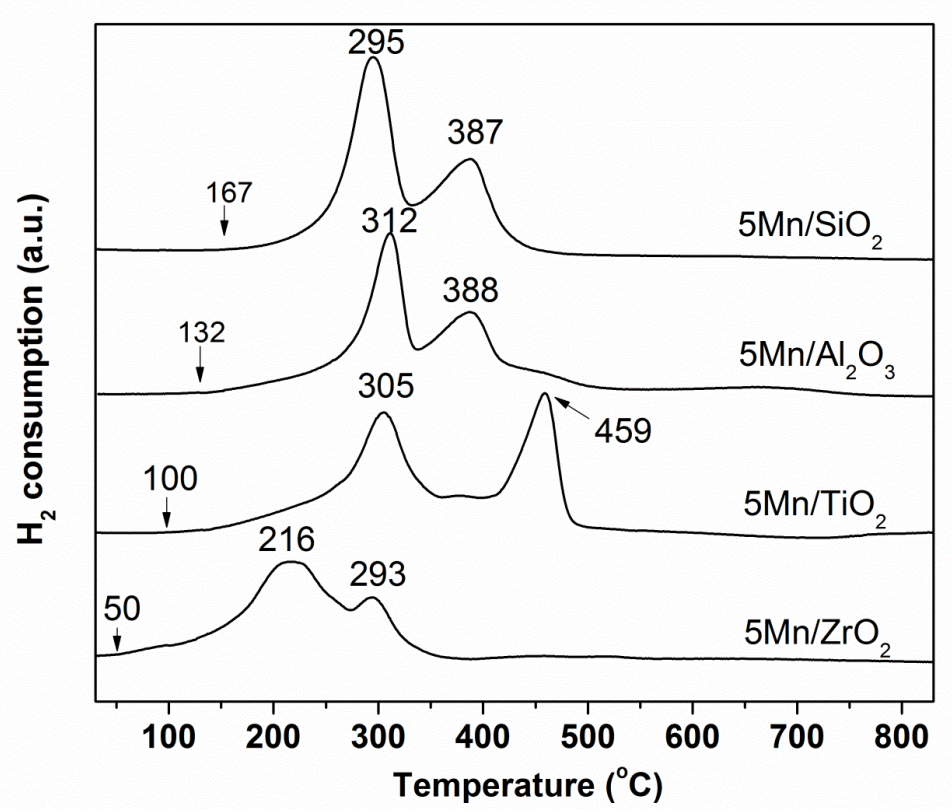

Figure III.7 Temperature programmed reduction profiles of manganese supported on various supports. Conditions: sample weight = 100 mg; reduction mixture = 10% H_2/Ar at 50 mL min^{-1}; heating rate = 10 °C min^{-1}.

III.4.2.2 Temperature Programmed Desorption of Oxygen

Figure III.8 shows O_2-TPD profiles of various Mn-containing adsorbents. It is well known that O_2-TPD is a useful technique to characterize oxygen vacancies and surface hydroxyl groups[54,124]. The species desorbed at low temperatures (normally under 400 °C) was probably ascribed to the surface hydroxyl groups or O^{2-}/O^{-} adsorbed on oxygen vacancies[124]. The peaks centered around 500 °C for each sample may be assigned to the desorption peak of lattice oxygen from MnO_2[64]. Further heat treatment may lead to the decomposition of Mn_2O_3, resulting in a second desorption peak at 789, 737, and 822 °C for $5Mn/Al_2O_3$, $5Mn/TiO_2$, and $5Mn/ZrO_2$, respectively. In addition, it is worth mention that all the samples were pretreated under pure helium flow at 250 °C for 1 h. Consequently, larger area under the TPD curve corresponds to higher amount of oxygen vacancies and surface hydroxyl groups retained on the surface of adsorbent upon thermal treatment.

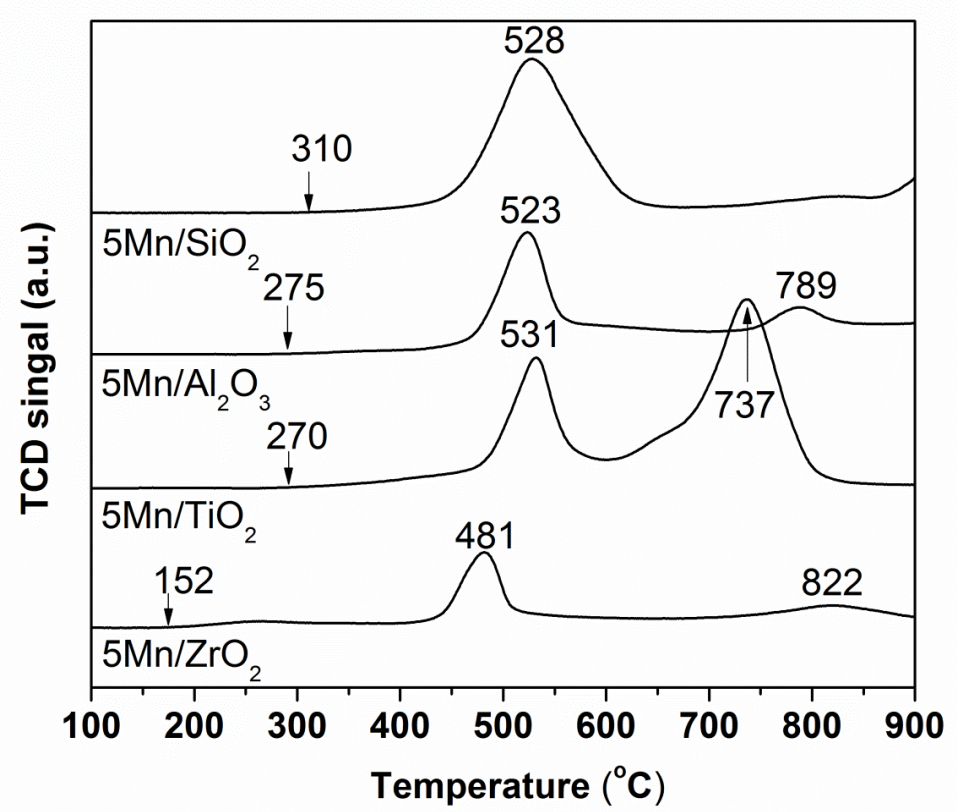

Figure III.8 O_2-TPD patterns of manganese supported on various supports. Conditions: sample weight = 200 mg; Helium flow rate= 50 mL min^{-1}; heating rate = 10 °C min^{-1}.

III.5 Effect of Calcination Conditions

The calcination temperature also affected the performance of MnO_x supported sorbents. As shown in Figure III.9, manganese doped on alumina was capable of improving SO_2 saturation capacity significantly when the samples were calcined above 550 °C. This implies that manganese plays an important role during SO_2 removal process. Among all the trials, 5MnAl-650 exhibited the best breakthrough & saturation capacity. For the samples treated under 400 °C in air, β-MnO_2 was the main manganese oxide species, which

was considered to be the less active component of the adsorbents[48,49]. However, α-Mn_2O_3 or even Mn_3O_4 may coexisted if the samples calcined at 650-800 °C[61]. Low oxidation state (Mn^{2+} and Mn^{3+}) manganese oxide nanoparticles were perceived as the active species in SO_2 adsorption process[48,49]. Furthermore, under calcination temperature of 800 °C, the pore structure of the sorbents was destroyed, which was not beneficial for gas phase adsorption. In spite of this, the desulfurization performance of 5MnAl-800 was higher than that of 5MnAl-550, which indicates that the influence of surface active species to SO_2 removal ability was more crucial than that of surface morphology. Liang et al. concluded that the activities of MnO_x were not significantly correlated with the BET surface areas, which is in agreement with our results[111]. Some other factors, such as surface hydroxyl group coverage and molecularly adsorbed water layer, which were thought to be important active species involved in the SO_2 adsorption process[83], are discussed in the following work.

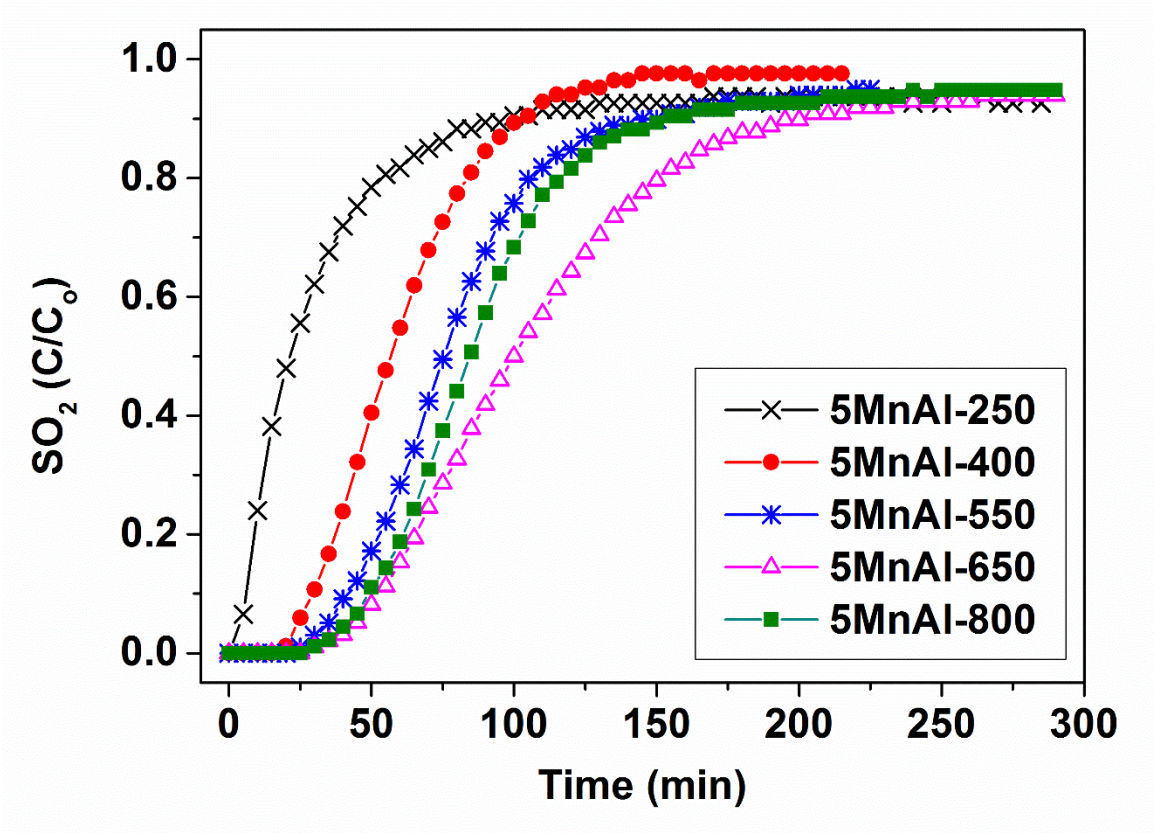

Figure III.9 Breakthrough curve of MnO_x supported on Al_2O_3 calcined at different temperatures. Adsorption conditions: C_o = 10 ppmv SO_2, room temperature, Flow rate=1000 mL min^{-1}.

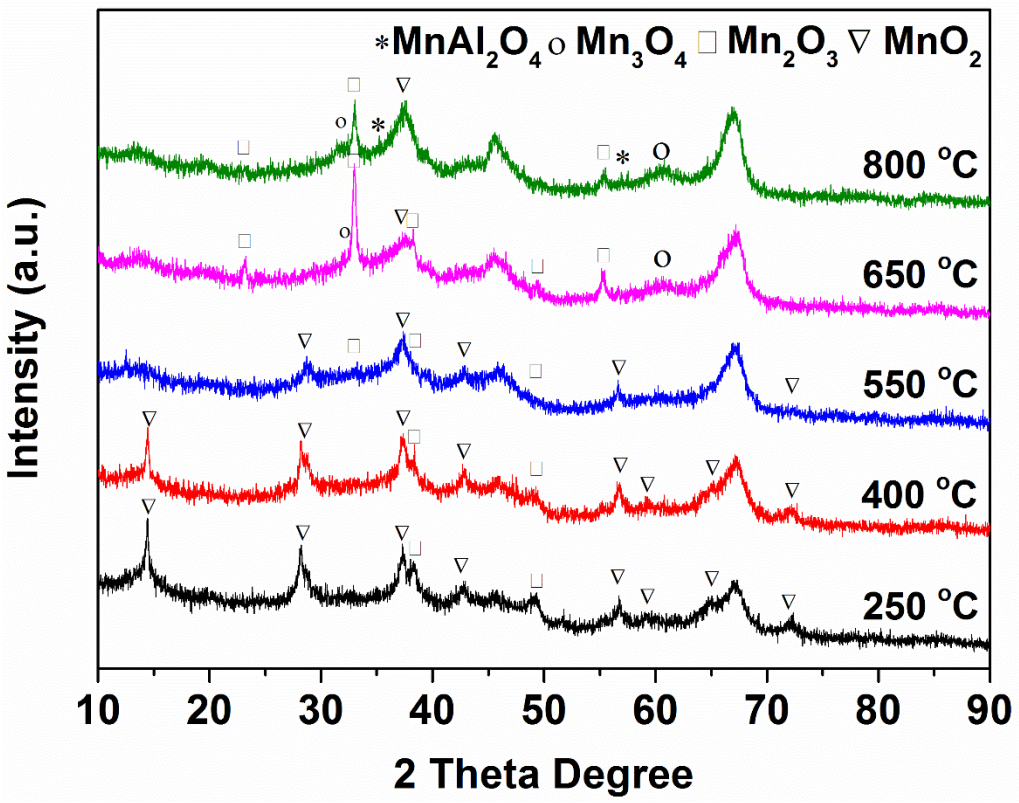

Figure III.10 XRD profiles of 5 wt.% Mn/Al_2O_3 calcined at different temperatures.

Furthermore, to verify the effect of calcination temperature on SO_2 removal performance, ZrO_2 support was also investigated in this study. As displayed in Figure III.10, for ZrO_2 support treated at various temperature, the order of SO_2 adsorption performance was similar to that for Al_2O_3 support.

Furthermore, it is shown in Figure III.10 that the XRD pattern of 5 wt.% Mn supported on γ-Al_2O_3 calcined at various temperature in air atmosphere. It is obvious that MnO_2 was the dominant manganese oxide species when the doped sample was calcined below 400 °C, which is in good accordance with the previous work[60]. The MnO_2 phases were gradually transformed into Mn_2O_3 by further increasing the calcination temperature to 550 °C. This can be attributed to the decomposition of MnO_2 into Mn_2O_3 and O_2 at 550-900 °C[61].

Table III.5 Crystallite size of 5 wt.% Mn/Al_2O_3 calcined at different temperatures

Calcination temp (^oC)	Crystallite Size (nm)		
	MnO_2	Mn_2O_3	Mn_3O_4
250	10.5	-	-
400	10.8	-	-
550	7.3	12.7	-
650	5.7	19.8	5.0
800	5.8	17.9	7.9

In Table III.5, the crystallite size of MnO_2 is diminishing, which implies that the relative content of MnO_2 decrease with increasing calcination temperature. When the calcination temperature was increased to 650 °C, most of the MnO_2 phase disappeared, indicating that the MnO_2 species were converted into Mn_2O_3 or Mn_3O_4. In addition, a small fraction of $MnAl_2O_4$ phase arose when the calcination temperature was 800 °C. It is well known that $MnAl_2O_4$ possesses a stabilized tetrahedral spinel structure, and its reactivity with SO_2 is very low[60]. Additionally, the formation of $MnAl_2O_4$ could cover the active sites such as Mn_2O_3 or Mn_3O_4 originally existed on the surface. Therefore, the SO_2 adsorption

ability of 5MnAl-800 was reduced compared with that of 5MnAl-650 due to the reasons described above.

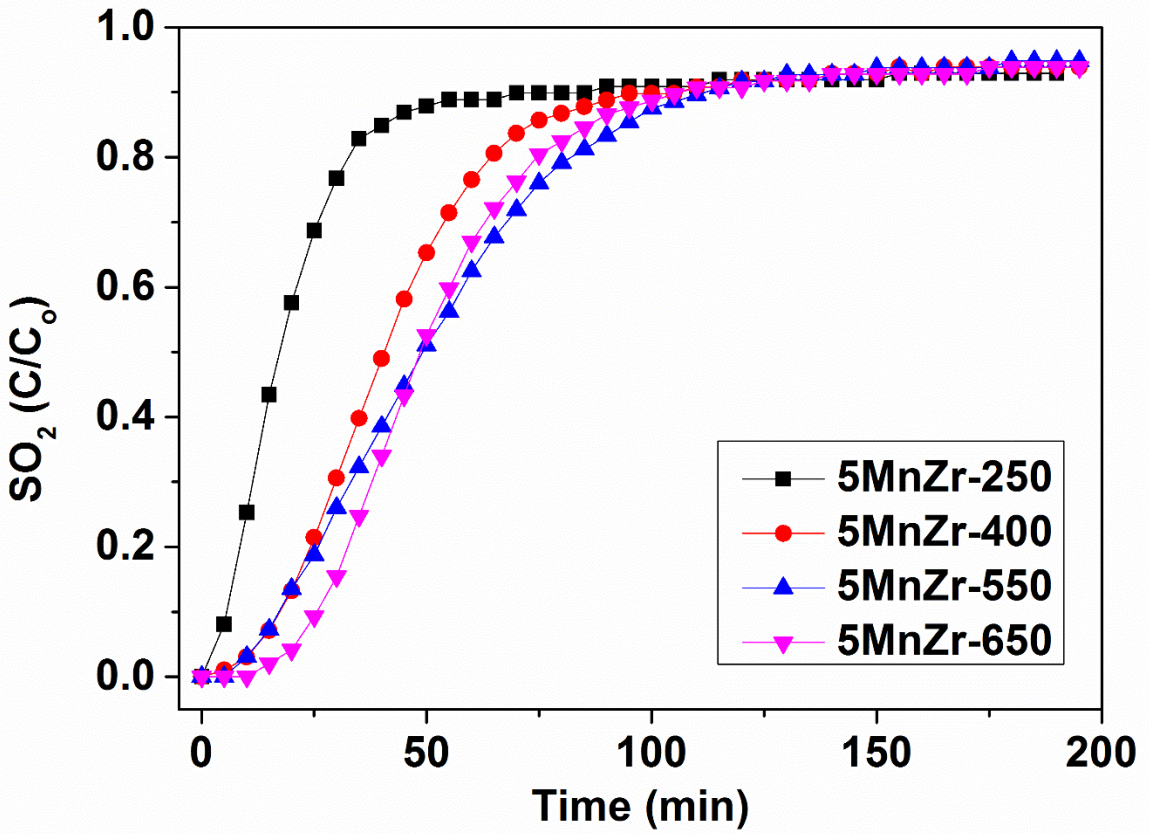

Figure III.11 Breakthrough curve of MnO_x supported on ZrO_2 calcined at different temperatures. Adsorption conditions: C_o = 10 ppmv SO_2, room temperature, Flow rate=1000 mL·min^{-1}.

Furthermore, as shown in Figure III.12, the oxidation state of manganese varied observably with different calcination temperatures. This phenomenon was also noticed by other researchers[60]. Yang et al.[61] synthesized MnO_x compounds by treating γ-MnOOH in air/N_2 from 250 to 1050 °C. With the help of TGA and XRD analysis, β-MnO_2 was the main species when the precursor was heated in the range of 250-400 °C under air atmosphere; α-Mn_2O_3 was formed if the sample was calcined above 550 °C; furthermore, Mn_3O_4 could be converted from α-Mn_2O_3 when the temperature exceeded 850 °C[61]. The plot of O/Mn ratio was displayed in Figure III.13. For the sample calcined at 650 °C in air, α-Mn_2O_3 may be the dominant species as the average oxidation state was close to 1.5, which is in agreement with previous conclusions[60]. With raising calcination temperatures, the two prominent reduction peaks migrated to the higher temperature, especially for the sample calcined at 650 °C. Similar results were reported by others[125]. The peak shift could be attributed to the much stronger interaction between the active species and alumina support when the samples were heated at higher temperature. It was also reported by Lou et al.[125] that the surface Mn concentration was decreased gradually with increasing calcination temperature. High temperature treatment may lead to aggregation and crystallization of MnO_x.

It is also worth mention that there was a shoulder existed at around 300 °C for the sample calcined at 350 °C. Since pure MnO_2 exhibited two separated reduction peaks, the pattern for 350 °C indicated that MnO_2 was the major active species. Another possible explanation is that the low temperature reduction peak was ascribed to the Al_2O_3 support

reduction due to the interaction with MnO_x on the surface[62]. Others also stated that the shoulder observed in the lower temperature region might be due to the decomposition of residual manganese nitrates because of the moderate calcination temperature[125,126]. It was also mentioned by Ettireddy et al.[62] that pure MnO_2 (O/Mn=2.0) and Mn_2O_3 (O/Mn=1.5) could be prepared by decomposing hydrous manganese nitrate under continuous airflow at 420 and 680 °C, respectively. Their statements were in good accordance with our TPR results.

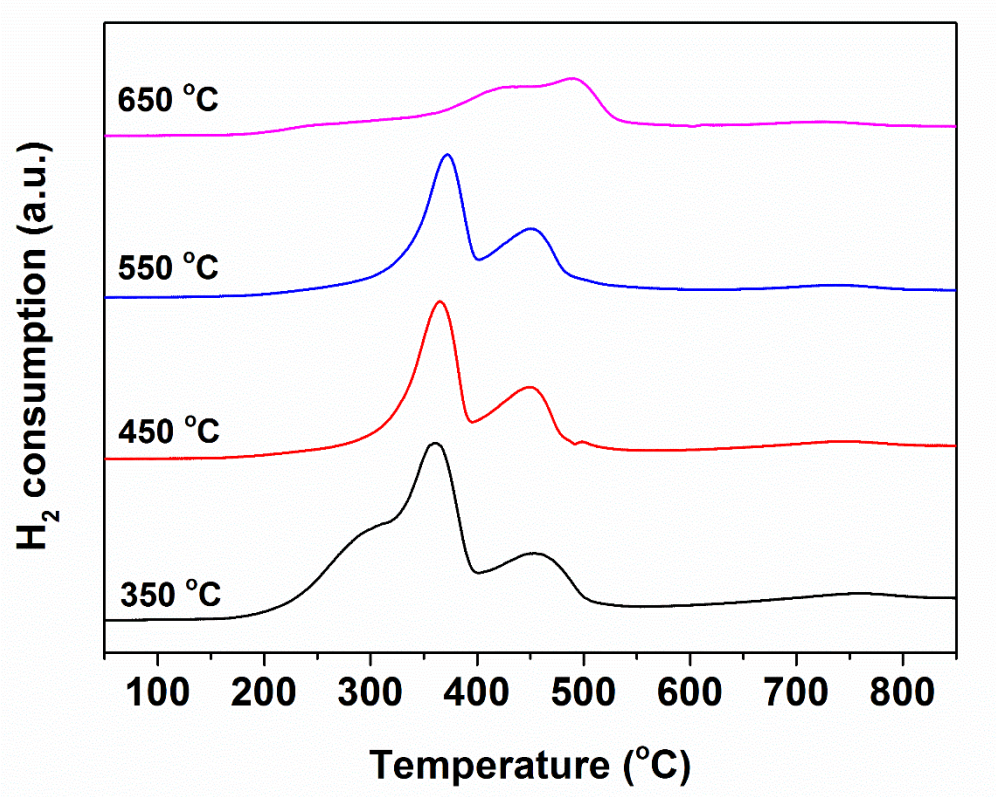

Figure III.12 Temperature programmed reduction profiles of 5 wt.% manganese supported on gamma alumina calcined at various temperatures. Conditions: sample weight = 100 mg; reduction mixture = 5% H_2/Ar at 15 mL min^{-1}; heating rate = 10 °C min^{-1}.

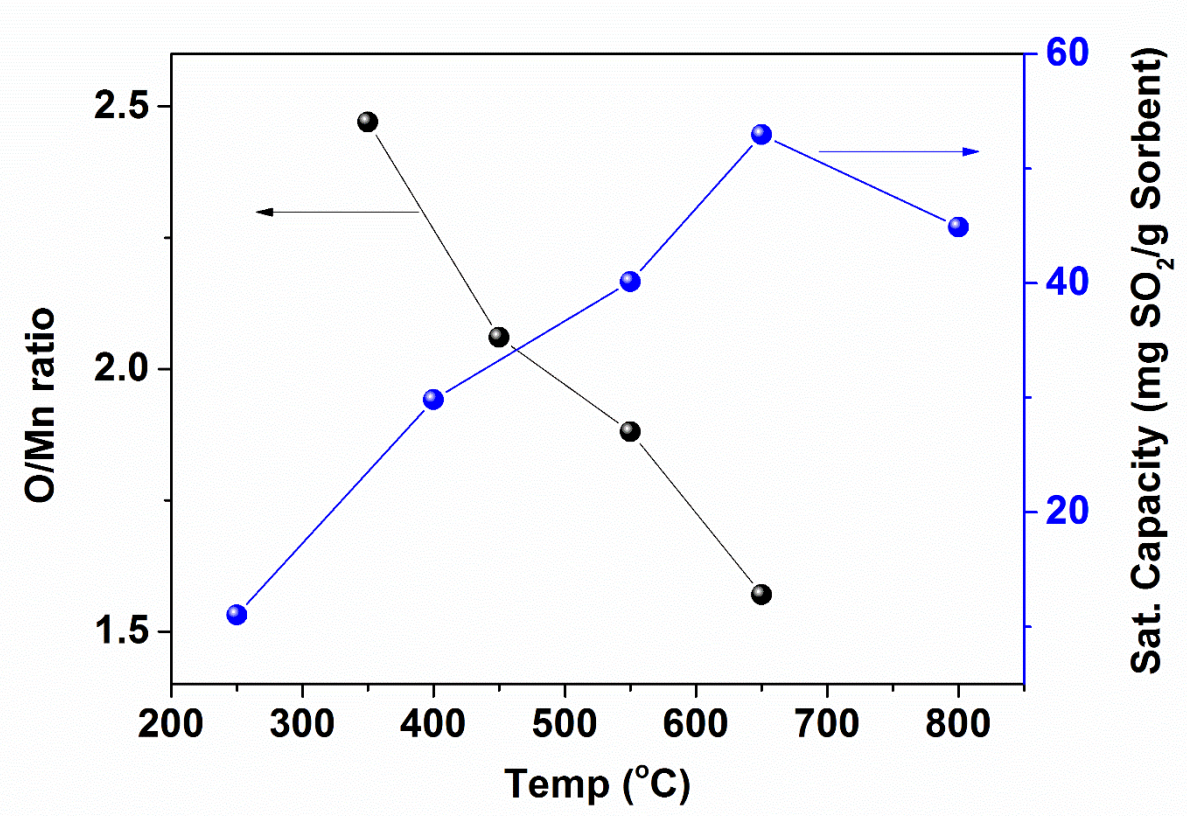

Figure III.13 Effect of calcination temperature on the SO_2 removal performance.

III.6 Regeneration Test

III.6.1 Single Cycle Test

To reduce the operation cost, regeneration study was conducted. Because of the nano-dispersed nature of the MnO_x, both the desulfurization and regeneration performance are improved compared to bulk metal oxide sorbents.

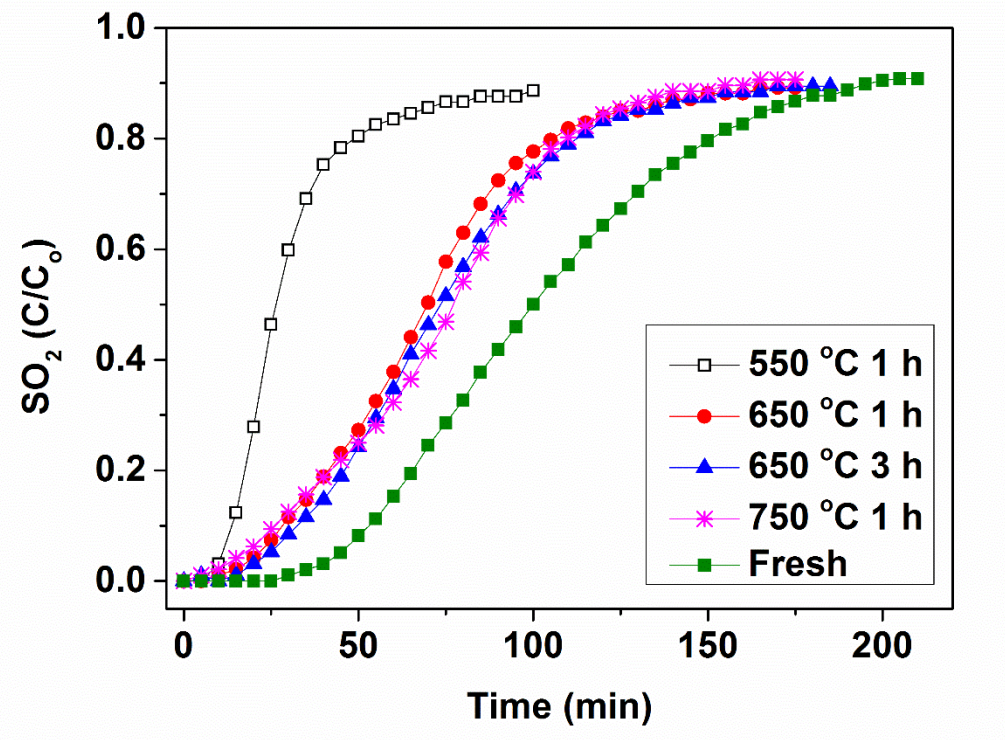

Figure III.14 Single cycle regeneration performance of $5Mn/Al_2O_3$-650 for SO_2 adsorption.

Lowell et al.[28] already stated that the spent Mn-containing sorbents, which is mainly in the form of $MnSO_4$, can be regenerated in air or N_2 atmosphere. However, by heating in

air under high regeneration temperature may result in severe sintering effect for the nano-dispersed MnO_x species. Therefore, all the regeneration tests were conducted in N_2 atmosphere (flow rate = 100 mL min^{-1}).

In can be concluded in Figure III.14 and Table III.6 that when the spent sorbents were regenerated at 650 °C for 1 h, there was a significant SO_2 adsorption capacity loss compared to that of fresh sorbent. Further increase the regeneration temperature to 750 °C enhanced the recovery percentage observably. Usually, higher regeneration temperature and longer regeneration time yields higher recovery percentage[29]. However, at 750 °C, when the regeneration time was increased to 3 h, there was no obvious enhancement of SO_2 adsorption ability. In addition, at regeneration temperature of 850 °C, however, the SO_2 breakthrough capacity was reduced by over 50 % compared to that of 750 °C and no observable increase of saturation capacity. There are several reasons to explain this. First, thermal treatment with longer time and higher temperature may destroy the porous structure of sorbent and lower the surface area. Under high temperature, the γ-Al_2O_3 may transformed into θ-Al_2O_3, whose surface area is usually less than 100 m^2 g^{-1}. Lower surface area is not beneficial for gas adsorption. Moreover, MnO could be formed at 800 °C under inert atmosphere, which can react with Al_2O_3 and generate $MnAl_2O_4$[60]. As mentioned before, the $MnAl_2O_4$ phase is not reactive toward SO_2 molecule and it might block the active sites. In summary, since regeneration time is an important factor for filter system design, shorter regeneration time can reduce the overall desulfurization reactor volume. Therefore, the best regeneration condition for 5Mn/Al_2O_3-650 is at 750 °C for 1 h.

Table III.6 Regeneration test of 5 wt.% Mn supported on Al_2O_3 calcined at 650 °C

Regeneration		5Mn/Al_2O_3-650		
Temp (°C)	Time (h)	B.T. Cap. [a] (mg SO_2/ g Sorbent)	Sat. Cap. (mg SO_2/ g Sorbent)	Recovery Percentage [b] (%)
Fresh		18.6	53.0	-
550	1	4.3	13.8	26
650	1	8.0	37.1	70
650	3	8.4	38.7	73
750	1	3.9	39.2	74

a. Breakthrough time at 0.2 ppmv breakthrough for SO_2.

b. Recovery percentage was defined as : Sat cap of regenerated sorbent/Sat cap of fresh sorbent

III.6.2 Multiple Cycle Test

Figure III.15 shows the multiple cycle desulfurization/regeneration test results for 5Mn/Al_2O_3-650. All of the desulfurization tests were conducted at room temperature with 10 ppmv SO_2 at the inlet, the detailed breakthrough conditions are listed in experimental section. All the regeneration tests were conducted at 750 °C for 1 h under N_2 flow of 200 mL min^{-1}. It can be seen in Figure III.15 that a significant breakthrough & saturation capacity loss occurred after the first cycle. This might be due to the sintering and agglomeration effect of metal oxides when the sorbent was calcined at 750 °C[48]. After that, the desulfurization performance almost unchanged up to 5 cycles. The multiple cycle test indicates that the manganese sulfates in the spent sorbent may not be regenerated completely under thermal treatment.

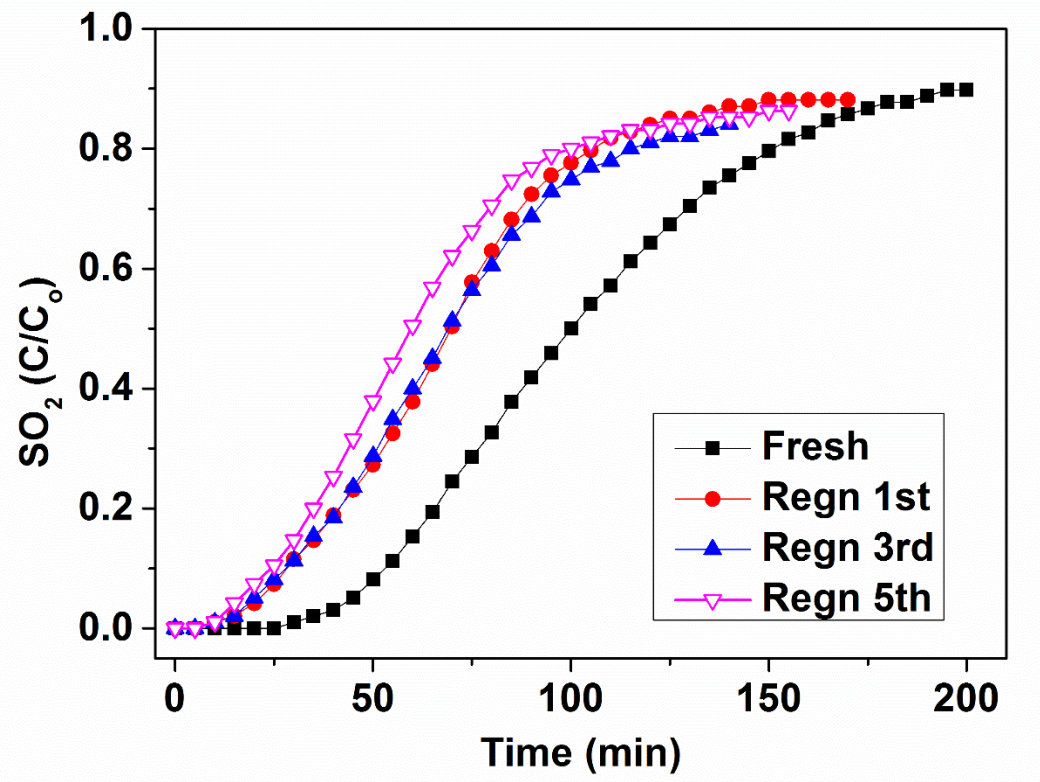

Figure III.15 Multiple cycle performance of 5Mn/Al_2O_3-650 sorbent (regeneration condition: 650 °C for 1 h).

III.7 Aging Test

Many types of sorbents or catalysts possess issues of shelf life[29]. Yang et al claimed that even the sorbent particles were placed in a well-sealed sample containers, the performance was decreased by almost 50 % after underwent one day aging[29].

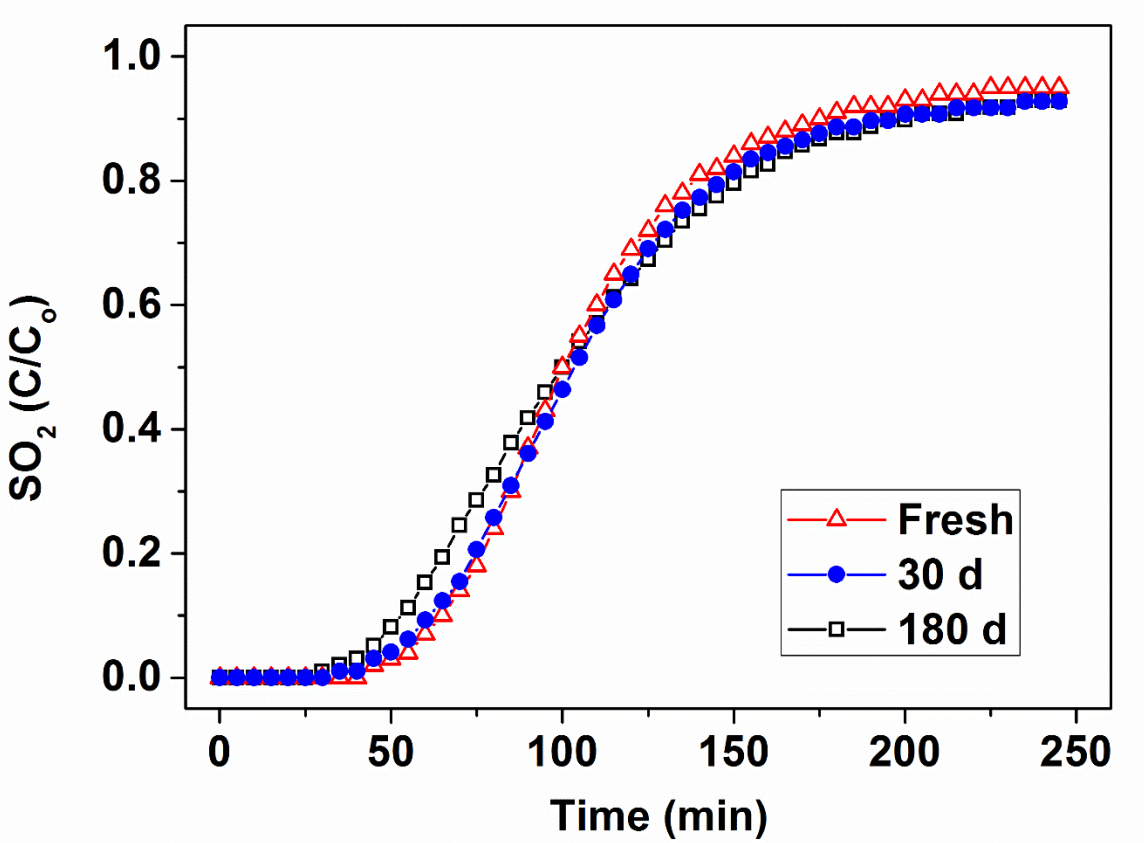

Figure III.16 Aging effect of 5Mn/Al_2O_3-650 Adsorption conditions: 10 ppmv SO_2, T = room temperature, Flow rate=1000 mL·min^{-1}. (Note: samples were calcined at 650 °C).

However, in this work, almost all of the capacity was retained after 30 days storage. As shown in Figure III.16, the slight difference for the two samples might be due to the uncertainty of particle size variation. Figure III.16 also indicates that both of the

breakthrough capacity and saturation capacity did not drop significantly even after the samples were aged for 180 days. More details for aging test are under further investigation.

III.8 Conclusions

In this work, the effect of active metal loadings, support materials, and calcination temperature in SO_2 adsorption performance were systematically studied. Among all the candidates, 5 wt.% Mn supported on γ-Al_2O_3 calcined at 650 °C in air exhibited the highest breakthrough and saturation capacity. A variety of manganese oxides with different valence state could be formed under various preparation conditions. Based on the breakthrough, XRD, and H_2-TPR results for various support materials and calcination temperatures, Mn_2O_3 is the principal active species involved in SO_2 adsorption process. The poor breakthrough performance of 5MnAl-250 revealed that MnO_2 possesses much less adsorption sites for SO_2. Furthermore, the oxygen chemisorption experiments as well as the breakthrough tests for different Mn loadings revealed that the active sites are associated with a highly dispersed oxide phase of Mn. The spent sorbents can be regenerated at 750 °C using nitrogen with minimal capacity loss up to 5 regeneration cycles. In addition, aging effect of the sorbents is negligible, indicating that the sorbents developed were ideal for long-term operation.

For Mn supported on various supports, the ratio of surface hydroxyl groups was different based on the XPS study. The SO_2 removal performance was related to the amount

of surface hydroxyl groups. In another words, the –OH groups were potentially important active sites during SO_2 adsorption process. The synergistic effect of Mn species and surface hydroxyl groups are under further investigation.

Chapter IV Kinetic Study of SO_2 Adsorption

IV.1 Introduction

Due to high energy conversion efficiency, extremely low emissions, and simple process for conversion of chemical energy to electrical energy, fuel cell power systems receive increasing attention over decades compared to conventional devices[127]. Among various types of fuel cells, solid oxide fuel cell (SOFC) has unique advantages including fuel flexibility, long term stability, high power density, and geometry flexibility[127]. However, one of the problems to be overcome is sulfur-poisoning effect on the cathode of SOFC, which stem from high-sulfur hydrocarbon fuels (e.g. jet fuel or diesel). The sulfur containing fuels not only cause anode degradation, but the SO_2 generated during combustion can further react with the cathode materials on the grain boundary of SOFC cathode[18]. It has been reported that 5-20 ppm SO_2 can be generated in a typical engine exhaust[11,19,20]. In addition, SOFCs cathode degradation is likely to occur even though SO_2 concentration is around 0.1 ppmv in air[17-19]. There are two approaches to address this problem. The first one is reducing the sulfur content in hydrocarbon fuels before the input fuel pass over its anode, thus alleviating SO_2 emission. But it is relatively expensive to remove sulfur by refining hydrocarbon fuels[128]. To prolong fuel cell service life, a better way is developing SO_2 sorbent with high efficiency and capacity to protect the cathode materials of SOFC.

Traditionally, Ca-based sorbents (e.g. CaO, $CaCO_3$, or $Ca(OH)_2$) are widely-used nowadays due to their low cost. But the spent gypsum waste is difficult to be disposed of[129–131]. Furthermore, the regeneration temperature of Ca-based sorbent is above 1000 °C, which is not practical for industrial application. Besides, the utilization of such sorbent is very low[129] and the remove efficiency can merely reach as high as 95 %[132]. Others also implied that the remove efficiency of conventional Ca-based sorbents is poor at low temperatures (< 100 °C)[133]. Over the recent years, removal of SO_2 with dry regenerable sorbents (mainly metal oxides) has gained increasing attention. The suitability of various metal oxides has been discussed by a number of studies[28,47,134]. It was experimentally explored that the bulk oxides of Mn, Co, and Cu were the most promising candidates to remove SO_2[35,131]. Koballa and Dudukovic[47] proposed various mathematical models and summarized that Ni, Mn, Co, Fe, and Zn are the most suitable metal oxide sorbents for SO_2 adsorption. Many studies have focused on CuO as a dry regenerative sorbent for SO_2 removal[135–137]. However, Cu-based sorbents usually exhibit high activity only at higher temperatures (e.g. 300—500 °C)[35,38]. Due to long start-up time of SOFC, it is expected that the desired sorbents are also effective at room temperature[127]. To best of our knowledge, there are few studies employing CuO as sorbents operated at low temperature. Manganese is a costless material while exhibits high sulfur removal efficiency over a wide range of temperature[48,49,138,139]. Moreover, to enhance the physical strength and utilization of the sorbents, great efforts were taken on the development of supported sorbents. Various porous materials including γ–alumina[134,140–142] and activated carbon[33,46,143] were widely

used as sorbent supports. In our case, activated carbon is not sustainable during adsorption (especially for regenerable applications) as the sorbent bed may expose in a high temperature oxidative environment.

Of the above, manganese oxide supported on γ-alumina is a promising candidate with several advantages, such as feasibility for desulfurization in wide temperature range, higher capacity compared to other candidates, and good performance for multiple adsorption/desorption cycles without significant capacity loss. Limited contacting efficiency within airstream, low mass transfer rate, limited duration of effectiveness, and high pressure drops are among the numerous problems within filtration systems. To further address these issues, a novel sorbent structure, microfibrous entrapped sorbents (MFES) were developed by Auburn University[144]. Typically, sorbents with various sizes (20-300 μm) can be entrapped into microfibrous networks. Based on application requirements, different types of sintered microfibrous media (e.g. metal, polymer, glass, and ceramic fibers) have been manufactured and commercialized. Detailed procedure for preparation of MFES is described elsewhere[29,145–147]. High void fraction and structural uniformity can be achieved using MFES, which helps minimize intrabed channeling or flow maldistributions[145]. Still further, the ease of pleating for microfibrous media helps lower the pressure drop significantly, thus minimizing parasitic power loss for the fuel cell power system[147]. A series of studies explored the functions and advantages of microfibrous media. Kalluri et al. concluded that the sorption capabilities of MFES outperformed packed beds due to high void fraction and uniform flow distributions present in microfibrous

materials[145]. Yang et al. investigated hydrogen sulfide removal using microfibrous entrapped zinc oxide sorbents, summarizing that MFES enhanced H_2S removal observably[148].

Furthermore, a reliable kinetic model is required to optimize and predict the desulfurization process. Over decades, various mathematical models have been studied by many researchers, which can be grouped as grain model[149–151], unreacted shrinking core model[130,133,149,152], deactivation model[153–158], random pore model[131], non-ideal adsorption model[129,159], and surface coverage model[160]. Unreacted shrinking core model was first developed by Levenspiel[161] and widely used to investigate gas solid reactions. Usually the conversion of sorbent is determined by a thermobalance. However, if two or more weight gain reactions occur simultaneously, it is difficult to distinguish between the weight gain by sulfation and by other side reactions. Similarly, kinetic studies of grain model are also conducted with the help of thermogravimetric analyzer. Some other researchers also investigated SO_2 adsorption process using the two models in a differential reactor[149]. In a word, both grain model and unreacted shrinking core model require analytical instrument with high precision. Other kinetic models such as non-ideal adsorption model and surface coverage model typically incorporate multiple parameters, which often have no actual physical meanings[132,159]. Furthermore, for non-ideal adsorption model, plausible empirical interpretation had to be introduced to match Arrhenius law[159]. The surface coverage model is actually derived from unreacted shrinking core model, so high experimental precision is also required throughout the adsorption process[132]. In the literature, deactivation models

were successfully employed in predicting breakthrough curves for various gas solid reaction systems[153,155–158,162,163]. For the deactivation models, a deactivation rate constant was introduced to describe the process during which SO_2 reacts with the sorbent to generate a dense sulfate layer. As the reaction progresses, diffusion resistance through this product layer causes a time-dependent decrease in the sorbent activity. Other physiochemical variations, such as pore structure, surface area, and active site distribution are also perceived as the factors to cause activation loss during sulfation process. In addition, in most literatures, deactivation of the solid reactant was assumed position-independent.

The objective of this article is to investigate the adsorption process between MnO_x/γ-Al_2O_3 and SO_2 at various temperatures, evaluating the effect of face velocity, inlet concentration, bed dilution, and so forth. Deactivation mechanism associated with dispersion model was proposed and breakthrough curves under different conditions can be predicted successfully. The mathematical model developed in this study can be applied for similar industrial gas adsorption systems.

IV.2 Experimental

IV.2.1 Sorbents Preparation and Characterization

Supported MnO_x sorbents were prepared by conventional incipient wetness impregnation method, using $Mn(NO_3)_2 \cdot 4H_2O$ (Alfa Aesar) as precursor and γ-Al_2O_3 (493 m^2/g, 0.68 cc/g, Sigma-Aldrich) as support, respectively. In the first step of sorbent

preparation, desired amount of manganese nitrate was doped upon the γ-Al_2O_3 particles (crushed and sifted) under vigorous stirring at room temperature. Thereafter, the samples were dried on a hotplate at 40 °C for 12 h, followed by aging at 120 °C overnight. It was further calcined in a box furnace (Lindberg/Blue M, Thermo Scientific) at 650 °C for 2 h with a ramp of 5 °C/min. The Mn loading on support was further confirmed by ICP-AES (Hazen Research) with uncertainty of $\pm$5 %.

The surface area, pore volume, and pore size distribution were measured by nitrogen adsorption-desorption analysis at -196 °C with Quantachrome Autosorb-1. The sorbents were outgassed at 200 °C for overnight under vacuum prior to measurements. The surface area (S_{BET}) was calculated by BET method; total pore volume was determined at p/p^o = 0.995; the pore distribution was obtained by applying BJH method on the desorption branch of isotherm curve.

X ray powder diffraction (XRD) patterns were obtained on a D8 Advance powder diffractometer (Bruker, Germany) in a 2θ range of 20-70° with a step size of 0.02° using Cu Kα radiation (λ=1.5406 Å, 40kV, 40mA). The grain sizes of dispersed metal oxides were estimated by applying Debye-Sherrer equation.

IV.2.2 MFES Preparation Approach

A conventional wet layup papermaking process was employed to prepare MFES: 6 g stainless steel (SS) fibers (12 μm dia. Type 316L, IntraMicron, Inc) and 1 g cellulose (as a binder in the preform) were dispersed in water and stirred vigorously in a blender for 2

min. A uniform suspension was formed and transferred into a headbox, and the preform media was cast after excess water was drained away. After that, the preform was pressed and dried in a convection oven at 120 °C for 2 h. Subsequently, the SS fiber sheet was pre-oxidized at 500 °C for 1 h in air to remove the bulk of the cellulose. Finally, the preform was sintered at c.a. 1 200 °C for 0.5 h in a reducing atmosphere (10 vol.% H_2 balanced in N_2, 1 000 mL min^{-1}), after which a sinter-locked network that is capable of entrapping particulates was formed. A protective layer, containing 8 μm dia. SS fibers, was prepared using a similar approach. The final media was composed of a particle-entrapping layer (top layer) and a protective layer (bottom layer) as shown in Fig. 1(a). Then, the calcined sorbent particles were dispersed into the top layer of the fiber matrix. Great care was taken to ensure that the sorbents were dispersed evenly, Fig. 1(b). Thereafter, circular disks were punched out from the sintered media to 105-108 % of the inner diameter of the reactor, which ensures good contact between the fibers and the inner wall of the reactor, Fig. 1(c). An SEM image of calcined sorbents entrapped in a 1:1 ratio of 8 and 12 μm microfibers is shown in Fig. 1(d).

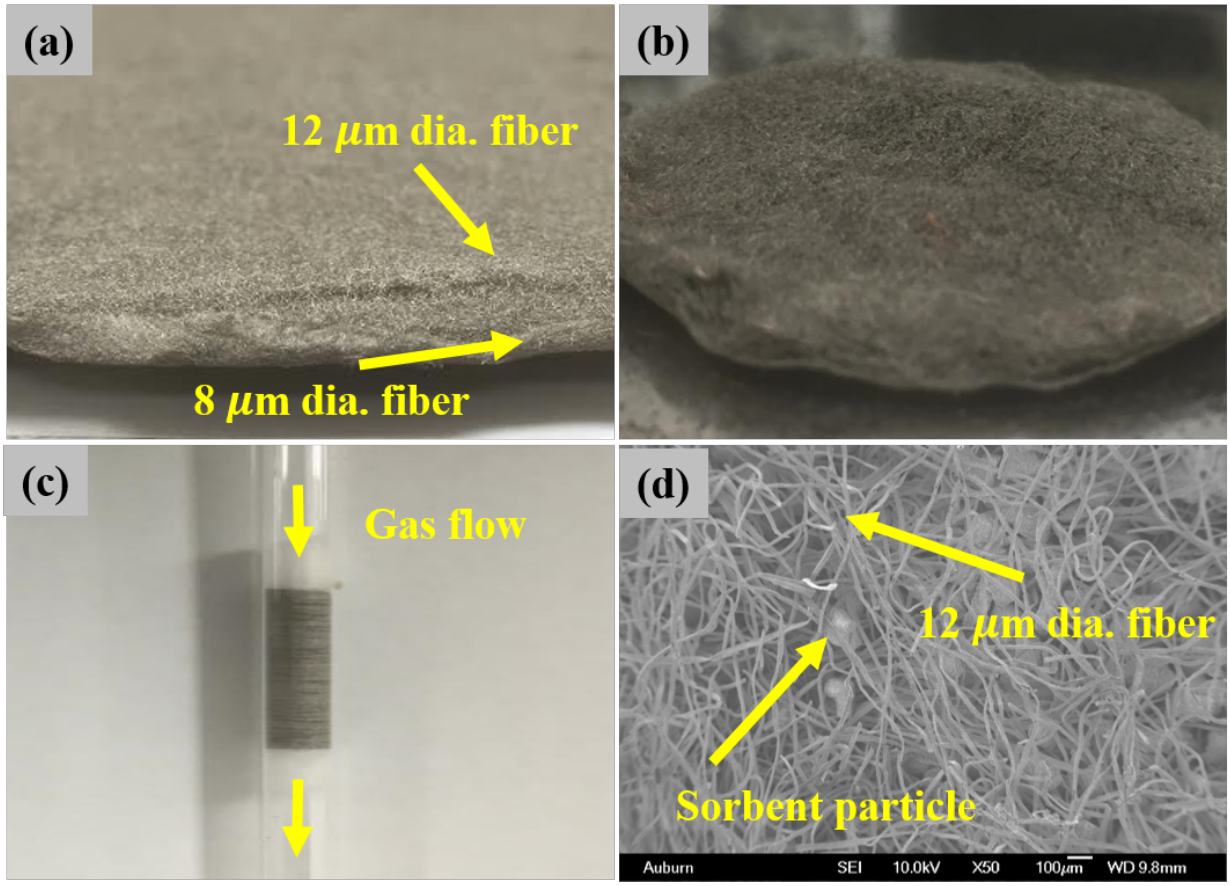

Figure IV.1 (a) Stainless steel fiber after sintering, (b) sorbent particles entrapped into stainless steel fiber sinter-locked network, (c) MFES loaded into quartz tube prior to breakthrough test, and (d) An SEM image of SS-MFES with 5Mn/γ-Al_2O_3 sorbents.

IV.2.3 Experimental Apparatus and Breakthrough Tests

If not otherwise mentioned, a vertical adsorption column made of quartz with an inner diameter of 3.8 mm was employed for the sorption experiments at various conditions. Prior to each experiment, the sorbent materials were heated to 120 °C with flowing N_2 (100 mL

min^{-1}) and held for 1 h, followed by adjusting to the desired temperature and holding for 1 h before the challenge gas was introduced. The gas mixture was flowing downward. A 50 ppm SO_2 in N_2 (Airgas Inc.) was used as the sulfur source. The SO_2 concentration was monitored by a MultiRAE pro equipped with an SO_2 sensor (RAE Systems), which was calibrated with 5.0 ppm SO_2 standard gas. The breakthrough tests were repeated at least twice for each sample, thus the experimental points reported are generated by taking the mean value. All the regeneration tests were conducted in anode exhaust gas (AEG), whose temperature usually varies between 600 and 900 °C. The AEG from the solid oxide fuel cell is typically comprised of CO_2, CO, H_2O, and H_2. In this study, the molar composition of the model AEG was kept as follows: $15CO_2$:20CO:$20H_2O$:$45H_2$. During regeneration process, the flow rate of the gas mixture was 100 mL min^{-1}. The sulfated sorbents were regenerated at 650 °C for 1 h. It is worth to mention that the regenerated samples were dried in flowing air at 110 °C for 1 h before the next breakthrough tests.

Three types of bed configurations were examined in this study. The first one is a PB of MnO_x supported on γ-Al_2O_3. The second is the sorbents diluted by inert particles (α-Al_2O_3). The third case is a microfiber entrapped MnO_x/γ-Al_2O_3 sorbent with the same volumetric sorbent loading as the diluted PB. The punched-out circular MFES disks were placed into the adsorption column with a glass rod. Extreme care was taken during the packing process. All the sorbent materials were captured between two quartz wool plugs.

IV.3 Mathematical Model

IV.3.1 Mass Balance

Assuming there was no radial concentration gradient, the concentration of the reactant (SO_2) passing through adsorbent bed is a function of axial distance (z) and time on stream (t). The following conservation equation can be derived based on differential mass balance of SO_2 in axial direction in the bed

$$\frac{\partial C}{\partial t} = D_z \frac{\partial^2 C}{\partial z^2} - \frac{u}{\varepsilon_b}\frac{\partial C}{\partial z} + r_{SO2} \tag{IV-1}$$

where,

$$\varepsilon_b = 1 - \rho_b/\rho_s \tag{IV-2}$$

The following initial and boundary conditions were applied in this study

I.C. $c(0, z) = 0,$ $at\ t = 0$ (IV-3)

B.C.1. $c(t, 0) = c_0 + \frac{\varepsilon_b D_z}{u}\frac{\partial c}{\partial z},$ $at\ z = 0$ (IV-4)

B.C.2. $\frac{\partial c}{\partial z} = 0,$ $at\ z = L$ (IV-5)

IV.3.2 Mass Transfer Resistance

For most adsorption processes, the overall reaction rates are affected by diffusion resistance. There are usually two types of diffusion resistance occurred in the gas-solid

adsorption system: (1) external mass transfer resistance and (2) internal mass transfer resistance. For external mass transfer process, Mear's criterion is employed to learn if mass transfer from the bulk gas phase to the sorbent surface can be neglected[164].

$$C_M = \frac{(-r)\rho_b(d_p/2)}{k_c C_{AO}} < 0.15 \tag{IV-6}$$

where,

$$k_c = \frac{ShD_m}{d_p} \tag{IV-7}$$

The Sherwood number can be estimated by various semi-empirical correlations

For PB, when $0<Re_{dp}<70$, and $0.25<\varepsilon_b<0.50$, Pfeffer's equation can be used as follows[145]:

$$Sh = 1.26(1-\zeta)^{1/5}\frac{(Re_{dp}Sc)^{1/3}}{\psi} \tag{IV-8}$$

For MFES, when $1<Re_{dp}<10000$, Dwivedi-Upadhyay correlation can be employed for materials with higher void fraction ($0.25<\varepsilon_b<0.97$)

$$Sh = \frac{0.455}{\varepsilon_b}(Re_{dp})^{0.59}Sc^{0.33} \tag{IV-9}$$

The internal mass transfer resistance can be estimated using internal effectiveness factor correlation. For first order reaction, which will be mentioned later, Weisz Prater

criterion[164] as well as equations including Thiele modulus can be used to calculated effectiveness factor (η)

$$C_{WP} = \frac{-r_A \rho_b (\frac{d_p}{2})^2}{D_e C_s} \quad \text{(IV-10)}$$

where,

$$D_e = \frac{D_m \varepsilon \sigma}{\tau} \quad \text{(IV-11)}$$

$$C_{WP} = 3(\Phi_1 coth\Phi_1 - 1) \quad \text{(IV-12)}$$

$$\eta = \frac{3}{\Phi_1^2}(\Phi_1 coth\Phi_1 - 1) \quad \text{(IV-13)}$$

IV.3.3 Axial Dispersion Effect

The axial dispersion coefficients as well as Peclet number for packed bed and MFES ($0.008 < Re_{dp} < 50$) can be estimated by the semi-empirical equation as follows[165,166]

$$D_z = 0.73 D_m + \frac{0.5 u_{in} d_p}{1 + \beta \frac{D_m}{u_{in} d_p}} \quad \text{(IV-14)}$$

$$Pe_{dp} = \frac{u d_p}{\varepsilon_b D_z} \quad \text{(IV-15)}$$

The molecular diffusivity (D_m) of SO_2 in the gas mixture can be obtained employing Fuller's method

$$D_m = \frac{10^{-3} T^{1.75} \left(\frac{1}{M_A} + \frac{1}{M_B}\right)^{\frac{1}{2}}}{P\left[(V_A)^{\frac{1}{3}} + (V_B)^{\frac{1}{3}}\right]^2} \quad \text{(IV-16)}$$

IV.3.4 Surface Reaction Mechanism and Governing Equation

Based on XRD results (as discussed in the previous Chapter), the primary metal oxide species presented on the alumina substrate was Mn_2O_3. Therefore, it is assumed that the following reaction took place between the gas-phase reactant and the Mn_2O_3 grains:

$$SO_{2(g)} + \frac{1}{2} Mn_2O_{3(s)} + \frac{1}{4} O_{2(g)} \rightarrow MnSO_{4(s)} \quad \text{(IV-17)}$$

As the reaction proceeded, the formation of $MnSO_4$ layer resulted in an additional resistance for the gas reactant (SO_2) to diffuse through (Gavaskar and Abbasian, 2007; Yasyerli et al., 2001). Noticeable reductions in active surface area and pore structure were expected because the molar volume of the product ($MnSO_4$) was higher than that of the reactant, i.e. Mn_2O_3 in this study (the expansion factor in this study is higher than 2.0). As shown in Fig. 2(a), at the very beginning of the reaction, the external surface of Mn_2O_3 was fully accessible by SO_2 molecules. As the reaction proceeded, a product layer gradually formed upon the surface of Mn_2O_3 grains, which is illustrated in Fig. 2(b and c). These morphological changes resulted in the reduction of available Mn_2O_3 sites for the gas-solid reaction when the product layer grew thicker. In this work, it is hypothesized that the following kinetic behavior takes place in the fixed-bed reactor:

$$-r_{SO2} = k_o \cdot a(t) \cdot C \tag{IV-18}$$

$$-\frac{d[a(t)]}{dt} = k_d \cdot C^m \cdot [a(t)]^q \tag{IV-19}$$

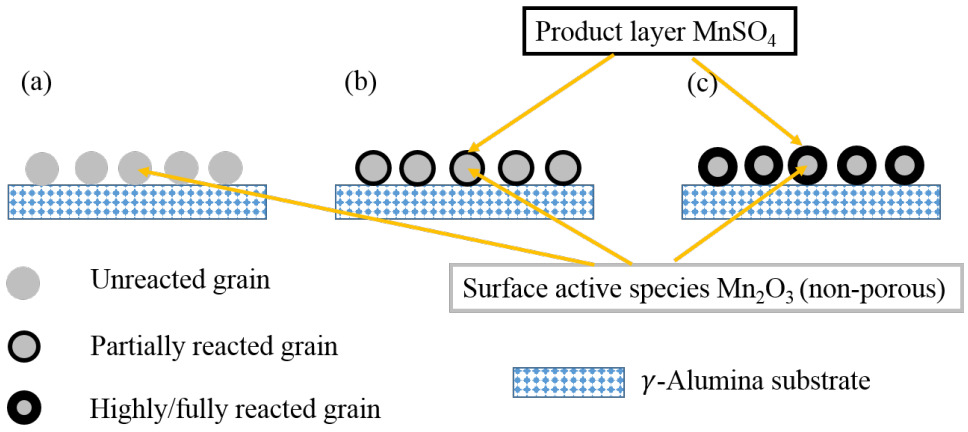

Figure IV.2 Schematic diagrams of surface reaction mechanism of SO_2 interacting with MnO_x grains. The grey circles are the assemblage of nonporous Mn_2O_3 grains.

It is also hypothesized that the values of *m* and *q* were both equal to one. The percentage of available adsorptive sites $a(t)$ is assumed to be 100 % at the beginning of the breakthrough tests (t=0). As the surface reaction proceeds, the adsorptive sites decrease over time. To derive the final governing equation, the major assumptions are as follows:

(1) The bed is isothermal due to low SO_2 concentration.

(2) The external mass-transfer resistance was negligible in this study. Based on Mear's criterion [164], the term $\frac{(-r)\rho_b(d_p/2)}{k_c C_{AO}}$ was much less than 0.15, which indicates that the

mass transfer resistance from the bulk gas phase to the sorbent surface can be ignored.

(3) The pressure drop along the bed is negligible.

(4) The reaction is assumed to be first order with respect to SO_2 [139,151,159]. The reaction rate with respect to oxygen was assumed to be zero [167] since oxygen consumption was negligible compared with its initial concentration during the adsorption process.

(5) There is no SO_2 concentration variance in the radial direction.

Based on the assumptions listed above and combining mass transfer resistance, initial and boundary conditions, axial dispersion effect of adsorbate, and surface reaction mechanism, the governing equation can be derived as follows:

$$\frac{\partial C}{\partial t} = D_z \frac{\partial^2 C}{\partial z^2} - \frac{u}{\varepsilon_b}\frac{\partial C}{\partial z} - \left(\frac{1-\varepsilon_b}{\varepsilon_b}\right) \cdot \eta \cdot k_0 \cdot a(t) \cdot C \qquad \text{(IV-20)}$$

The partial differential equation was solved with MATLAB ver. R2015a (Mathworks, Inc.) numerically. The independent characteristic parameters k_0 and k_d can be determined by minimizing the residual sum of squares between the experimental data points and the model response. The Nelder-Mead search algorithm was employed to obtain k_0 and k_d.

Furthermore, to evaluate the adequacy of the model, the overall error in predicting the experimental breakthrough curves is evaluated using the root mean square error (RMS), which can be defined by equation 21:

$$RMS(\%) = \sqrt{\frac{\sum_n (\frac{C_{model} - C_{exp}}{C_{exp}})^2}{n}} \times 100\% \quad \text{(IV-21)}$$

IV.4 Results and Discussion

IV.4.1 Determination of the k_0 and k_d Values

A 3D plot of SO_2 concentration varying with bed length and time on stream is shown in Fig. IV.3, where the inlet SO_2 concentration was 10 ppm, face velocity 1.33 m s^{-1}, and adsorption temperature 20 °C. The cross section of the 3D curve at z = L corresponds to the breakthrough curve measured experimentally at the outlet. A series of breakthrough curves conducted between 20-300 °C and at 10 ppm SO_2 is shown in Fig. IV.4 along with the simulated results. An increase of the desulfurization temperature shifted the curves to longer time due to an enhancement to the surface reaction rates (Table IV.1). The RMS error of the simulated breakthrough curves is between 2.5 and 4.2 %. The low RMS error allows for the confident use of the determined k_0 and k_d values further in this study.

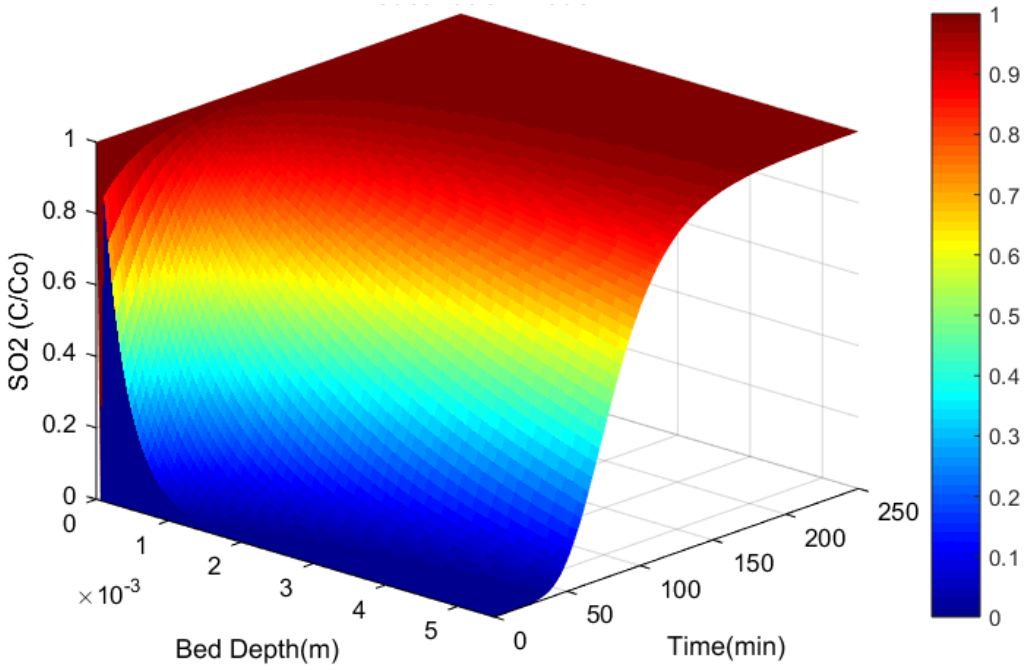

Figure IV.3 Model prediction of SO_2 adsorption process. (C_o = 10 ppm; Face velocity = 1.33 m/s; T = room temperature; Sorbent: $5Mn/Al_2O_3$)

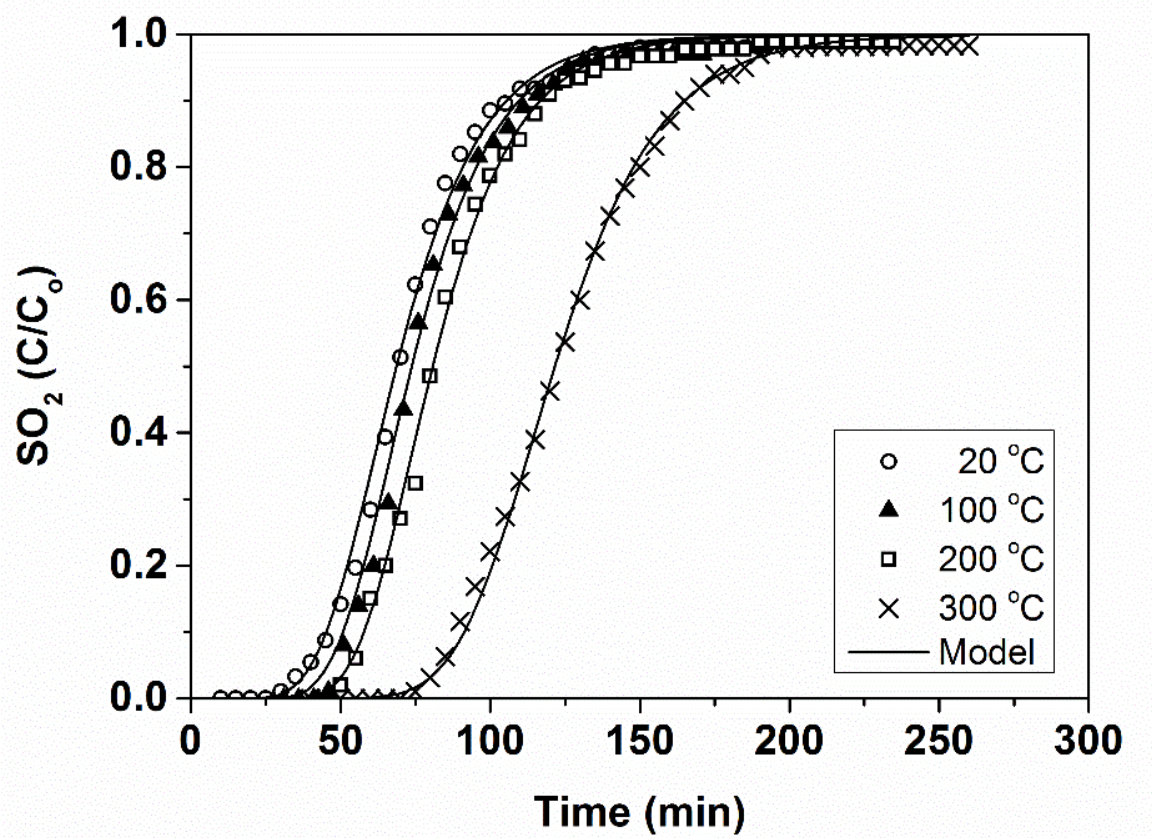

Figure IV.4 Breakthrough curves of 5Mn/γ-Al_2O_3 at various temperatures. In each experiment, 50 mg sorbent was loaded into a quartz tube and tested with 10 ppm SO_2 at a flow rate of 1 000 mL min^{-1}.

Table IV.1 Kinetic parameters obtained from the breakthrough data at various temperatures

T	k_0	k_d	RMS error
°C	s^{-1}	$m^3\ mol^{-1}\ g^{-1}$	%
20	2.33×10^{4}	6.80×10^{-4}	3.8
100	2.78×10^{5}	2.23×10^{-3}	2.5
200	3.05×10^{6}	3.35×10^{-2}	4.2
300	3.75×10^{6}	6.38×10^{-2}	3.5

IV.4.2 Predicted Breakthrough Curves of Varying Face Velocity

To investigate the effect of face velocity, SO_2 breakthrough results were obtained in the range of 0.67-2.67 m s^{-1}, as shown in Fig. IV.5. The predicted breakthrough curve was generated by substituting the predetermined values of k_0 and k_d into equation (IV-20). As expected, the breakthrough time decreased as the flow rate of the challenge gas stream increased. The predicted breakthrough curves (solid lines) agreed well with the experimental results (scattered dots) with RMS error less than 10 % (Table IV.2). The results indicate that k_0 and k_d are not dependent on face velocity. Furthermore, the consistency of saturation capacity shown in Table IV.2 reinstate that the external mass transfer resistance was negligible. However, minor deviations in the high C/C_o region were observed. These deviations can be attributed to the device uncertainty occurring at high or low dimensionless SO_2 concentration region. The other possible reason is that once all the

surface accessible MnO_x species are depleted, the SO_2 molecules start to interact with or adsorbed by the porous γ-Al_2O_3 material, which is much less active compared to MnO_x.

Table IV.2 Saturation capacities of 5Mn/γ-Al_2O_3 at various face velocities

u m s^{-1}	Saturation capacity mgSO_2 (g sorbent)$^{-1}$	RMS error %
2.67	44.7	3.6
2.00	44.3	9.5
1.33	46.3	N.A.
0.67	45.5	5.8

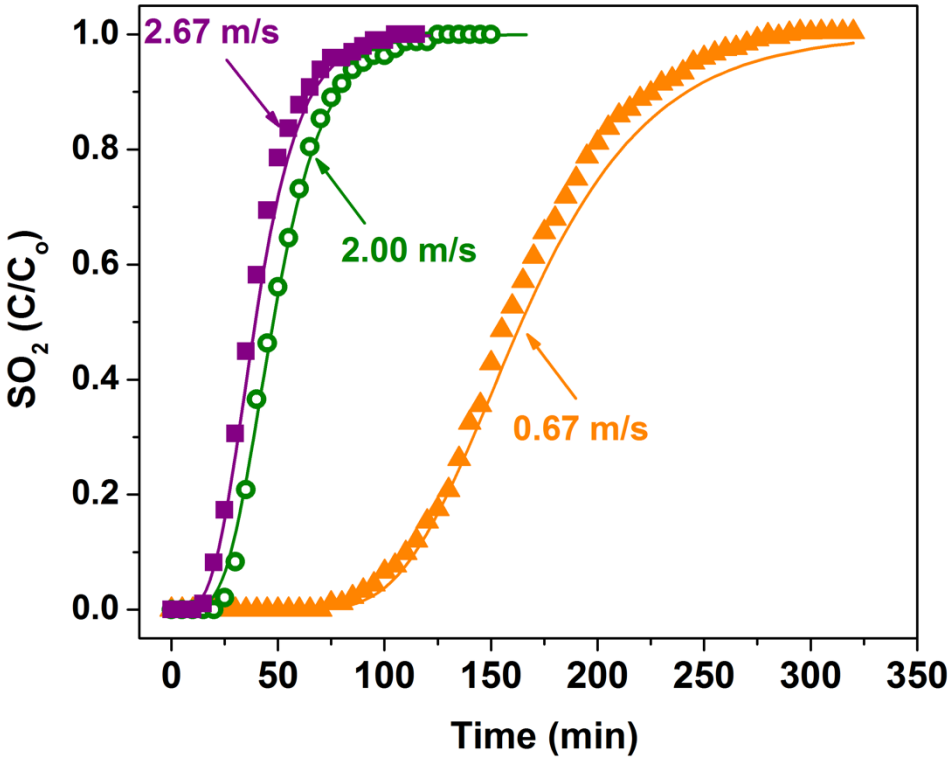

Figure IV.5 Predicted breakthrough curves of 5Mn/γ-Al_2O_3 sorbents at various face velocities. Sorbent (50 mg) was tested at 20 °C with 10 ppm SO_2 in a 3.8 mm I.D. tube. The scattered dots are experimental data. The solid lines correspond to the calculated values generated by MATLAB. The k_o and k_d are adopted from Table IV.1.

IV.4.3 Predicted Breakthrough Curves with Varying Inlet Concentration

The experimental SO_2 breakthrough curves operated at various inlet concentrations are shown in Figure IV.6. Given the RMS error of these tests are around 10 %, the adequacy of the proposed mathematical model is acceptable. It is also worth mention that both the

initial rate constant k_0 and the depletion constant k_d did not vary significantly over the concentration range investigated here. The conclusion is in accordance with the study by other authors [156,168].

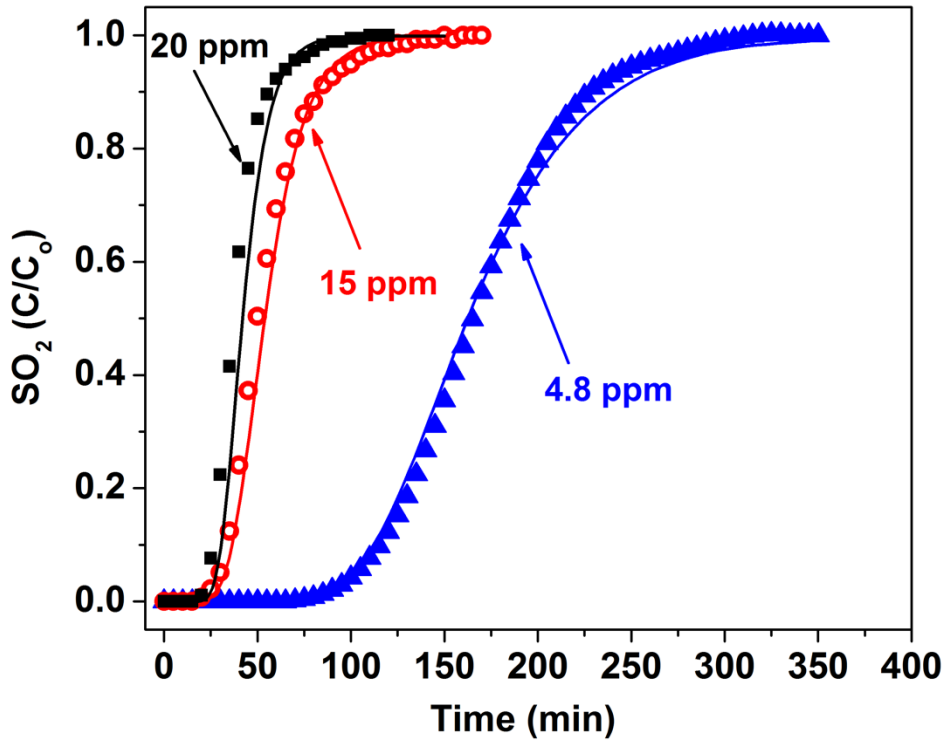

Figure IV.6 Predicted breakthrough curves of 5Mn/γ-Al_2O_3 sorbents at various SO_2 inlet concentrations. Sorbent (50 mg) was tested at 20 °C at a face velocity of 1.33 m s^{-1} in a 3.8 mm I.D. tube. The scattered dots are experimental data. The solid lines correspond to the calculated values generated by MATLAB. k_o and k_d are adopted from Table IV.1.

IV.4.4 Predicted Breakthrough Curves with Varying Adsorbent Particle Size

The experimental breakthrough results of various particle sizes are shown in Fig. IV.7 (a). Due to the lower internal mass transfer resistance, the smaller particle size resulted in higher breakthrough time (30 min). The predicted breakthrough results are shown in Fig. IV.7 (b). It can be seen that the calculated results were in good agreement with the experimental data.

(a)

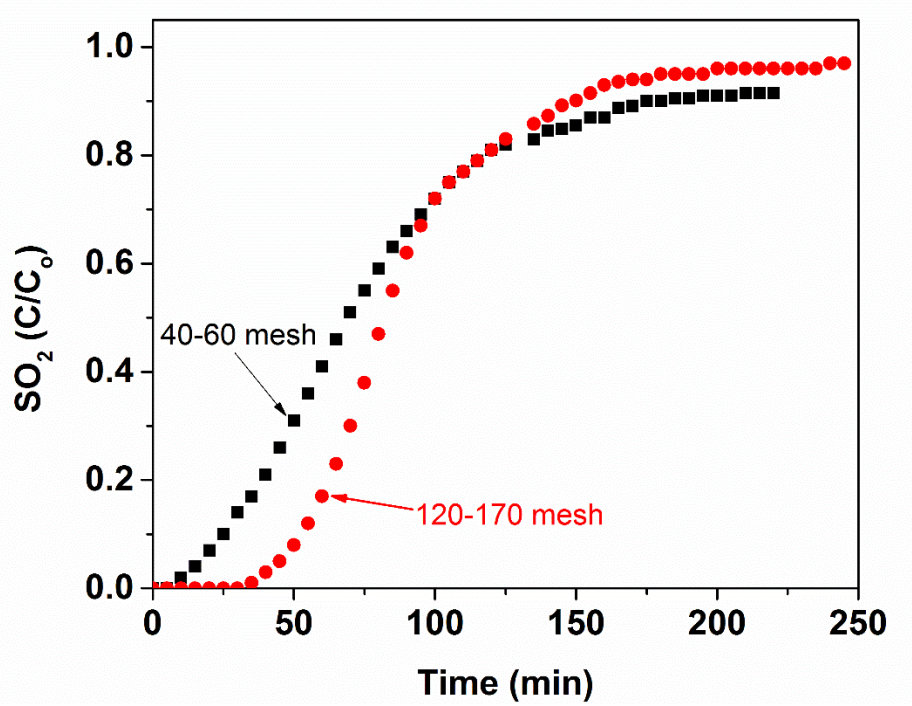

(b)

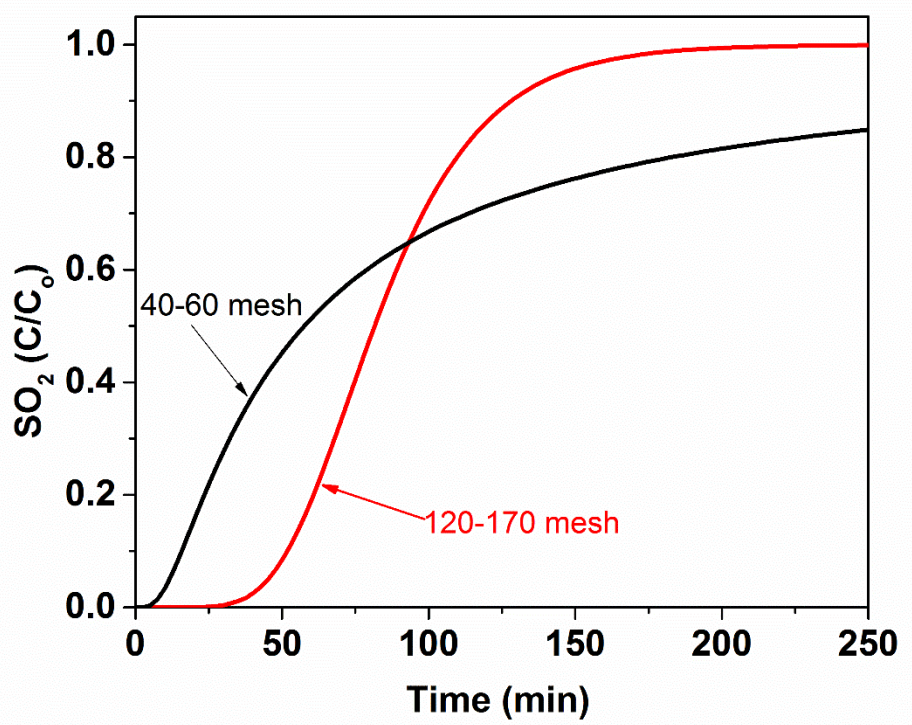

Figure IV.7 Predicted breakthrough curves of 5Mn/γ-Al_2O_3 sorbents at various sorbent particle sizes. Sorbent (50 mg) was tested at 20 °C at a face velocity of 1.33 m s^{-1} in a 3.8 mm I.D. tube. (a) the experimental results conducted when the particle size is 40-60 mesh and 120-170 mesh, respectively; (b) the simulated results when the particle size is 40-60 mesh and 120-170 mesh, respectively.

IV.4.5 Breakthrough Tests Using MFES

The experimental results of the PB, diluted PB, and MFES materials are shown in Fig. IV.8. The bed void fractions are listed in Table IV.3. The particle size of sorbents as well as the diluent (α-Al_2O_3) was in the same range (88-125 μm). As can be seen in Fig. IV.8,

the breakthrough time of the diluted PB was slightly higher than that of the PB without dilution. Moreover, MFES outperformed the PB observably. The breakthrough time for MFES (42.5 min) was about one and a half fold higher compared to PB without dilution (30.1 min), and 1.2 times higher when the PB was diluted (35.3 min).

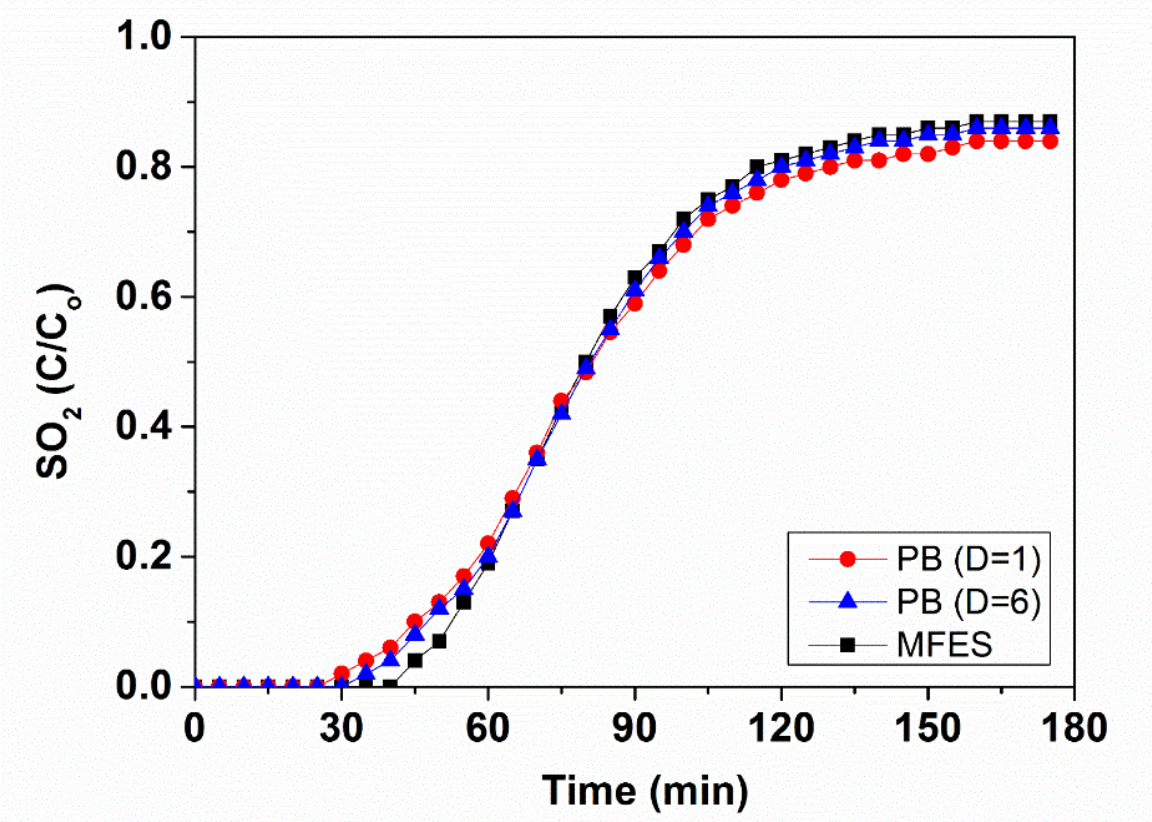

Figure IV.8 Breakthrough curves of PB, diluted PB, and MFES. Sorbents (150 mg) were tested at 20 °C with 10 ppm SO_2 at a face velocity of 1.33 m s^{-1} in a 6.8 mm I.D. tube.

Table IV.3 Properties of PB, diluted PB, and MFES

Type	PB (D=1)	PB (D=6)[a]	MFES

Fiber (vol.%)	N.A.	N.A.	8.5
Void (vol.%)	32.3	32.3	78.7
Sorbents (vol.%)	67.7	11.3	12.8
Residence time (ms)	1.23	7.61	18.7
D_z ($cm^2\ s^{-1}$)	1.95	1.63	0.26

a. α-Al_2O_3 (Surface area < 20 $m^2\ g^{-1}$) was used as diluent.

The better performance was achieved by MFES is because of the increase in void fraction compared to a PB, the gas phase interstitial velocity (u_{in}) within MFES was much lower than that within the PB. Correspondingly, the SO_2 residence time of MFES was higher (shown in Table IV.3) and so was the opportunity for the SO_2 molecules to interact with the adsorptive sites. Moreover, axial dispersion has an important effect on the breakthrough performance. Owing to longer bed length and higher bed void fraction, the axial SO_2 concentration gradient of MFES was smaller than that of PB, resulting in a smaller axial dispersion coefficient for MFES. As Table IV.3 displays, the axial dispersion coefficient (calculated according to equation IV-14) decreases with increasing bed dilution and voidage, which is in accordance with the literature [145]. With higher axial dispersion of SO_2 molecules in the PB, self-broadening concentration fronts exist in the axial direction. Therefore, the breakthrough time of the PB occurred earlier than that of the MFES. It was also worth to mention that the external mass transfer resistance was eliminated in these cases since the superficial velocities were sufficiently high, though the mass transfer coefficient of MFES was actually lower than that of the PB comprised of the same particle

size. Internal mass transfer resistance, which is mainly controlled by particle size and system temperature, was the same for all three cases.

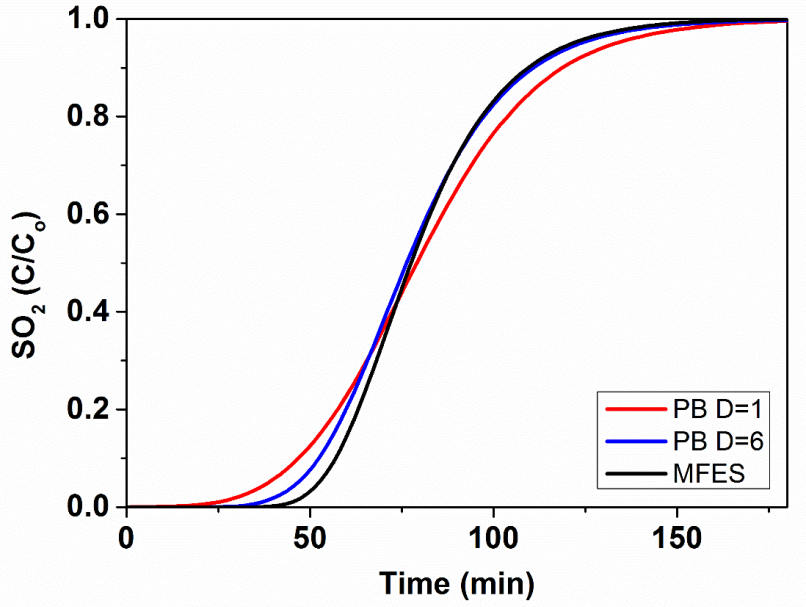

Figure IV.9 Model prediction of breakthrough curves of PB, diluted PB (D=6), and MFES. The breakthrough curves were obtained by MATLAB ver. R2015a employing k_o = 2.33×10^{4} s^{-1} and $k_d = 6.79\times10^{-4}$ $m^3mol^{-1}g^{-1}$.

Table IV.4 Comparison of experimental breakthrough time and predicted breakthrough time for various bed configurations

Bed Type	Experimental breakthrough time @ $C/C_o = 0.01$ (min)	Predicted breakthrough time[a] @ $C/C_o = 0.01$ (min)
PB (D=1)	30.1	30.3
PB (D=6)	35.3	40.2

MFES	42.5	47.4

a. The breakthrough time was predicted by the model using predetermined k_o and k_d listed in Table IV-1 at 293 K.

Channeling or flow maldistribution is another important factor which accounts for different breakthrough behavior between PB and MFES. It is known that channeling or flow maldistribution can seriously hinder attempts to achieve high conversion in the PB [161]. Accordingly, clustering of small particles as well as the wall effect in a PB plays a negative role in the adsorption process. In contrast, the random orientation of the microfibers provided a uniform flow profile throughout the bed, which minimized channeling and assisted with mixing [148]. This is an important reason for MFES to outperform traditional PB and diluted PB. As can be seen in Table IV-4, the predicted breakthrough time of PB (D=1) is close to the experimental results; whereas the predicted breakthrough time of PB (D=6) and MFES are higher than the experimental results. For a diluted PB, channeling and flow maldistribution still take place. However, the mathematical model did not include this factor. As a result, the breakthrough time was overestimated by the mathematical model. For the MFES, high flow rates can cause void reduction, since the nonwoven media is compressible [169]. Therefore, negative effects such as lower residence time as well as a higher degree of axial dispersion would explain why the experimental breakthrough time was lower than the predicted breakthrough time in the case of MFES. Compared with Fig. IV.8, all the predicted breakthrough curves shown in Fig. IV.9 coincided with the

experimental data, even though there were a few deviations at higher C/C_o. The small deviations might be a result of the uncertainty of the monitoring device in the higher C/C_o region. The mathematical model used does not match the exact shape of the experimental breakthrough curve. However, it is capable of reproducing the experimental trends.

IV.4.6 Comparison of Regeneration Performance between PB and MFES

The desulfurization/regeneration study regarding PB and MFES is shown in Fig. IV.10. Both the PB and MFES contained c.a. 150 mg sorbent and the breakthrough point was defined at C/C_o = 0.01. The gas flow rate was maintained at 3 L min^{-1} and the other adsorption conditions were the same as described in Fig. IV.8. It is demonstrated in Fig. IV.10 that significant breakthrough time (capacity) losses occurred for the first regeneration cycle regardless of bed configurations. This is attributed to considerable crystallite size increase resulting from thermal treatment [29]. After the first cycle, the breakthrough time (capacity) remain unchanged up to 5 cycles. The regeneration performance can be enhanced by using MFES. Based on the results, MFES was capable of retaining 67 % breakthrough capacity after the first regeneration cycle; whereas, PB could only achieve about 51 % of the original breakthrough capacity. It was well-known that, sorbents could undergo attrition during *in situ* thermal regeneration, resulting in a higher degree of channeling or sorbent clustering [170]. On the other hand, owing to the sinter-locked microstructure, MFES can prevent the adsorption bed from further channeling or flow

maldistribution in the presence of high temperature or face velocities. Furthermore, the SEM image in Fig. IV.11 indicates that the stainless steel microfibrous structure was robust after multiple adsorption/regeneration cycles. In practical filtration application, the noteworthy improvement of breakthrough performance due to the use of MFES can bring considerable economic benefits.

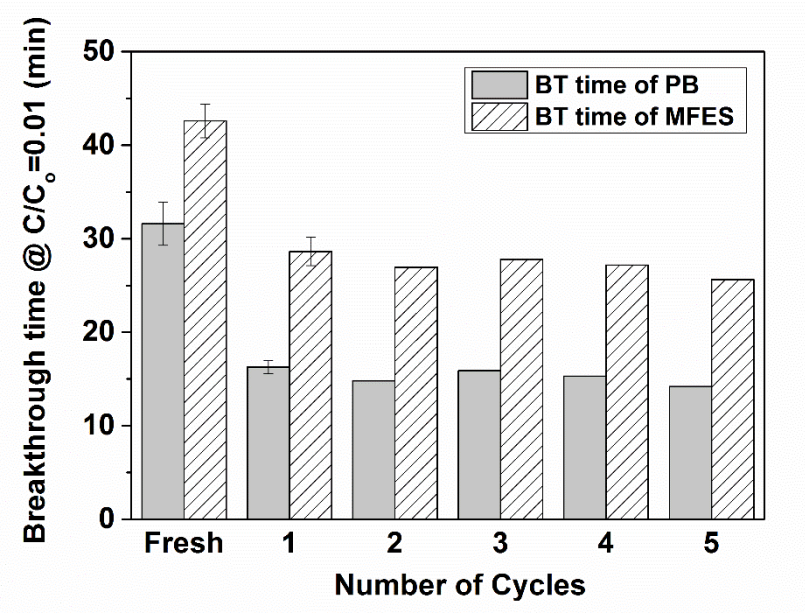

Figure IV.10 Breakthrough time of PB and MFES of multiple adsorption/regeneration cycles. Sorbents (150 mg) were tested at 20 °C with 10 ppm SO_2 at a face velocity of 1.33 m s^{-1} in a 6.8 mm I.D. reactor. Regeneration tests were conducted *in situ* at 650 °C in model AEG for 1 h.

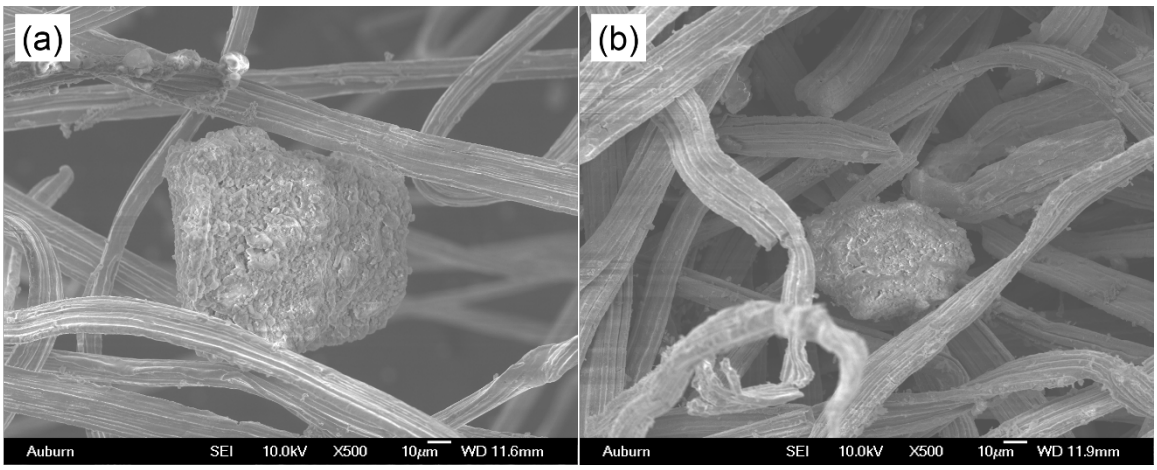

Figure IV.11 SEM images of (a) fresh 5Mn/γ-Al_2O_3 entrapped in SS MFES, and (b) regenerated 5Mn/γ-Al_2O_3 entrapped in SS MFES after the 5th cycle. (SS fiber, 12 μm; 5Mn/γ-Al_2O_3 particles, 88-125 μm.)

IV.5 Conclusion

The mathematical model based on axial dispersion, diffusion resistance, and surface reaction mechanism has been successfully established to describe the breakthrough behavior under various conditions. The calculated breakthrough curves of the PB agreed with the experimental results with RMS errors less than 9.5 %, which indicates the efficacy of this model in predicting the performance of the sorbents with satisfactory accuracy. The trend of the breakthrough performance of various fixed bed configurations (i.e. diluted PB, MFES bed) containing the equivalent amount of sorbent could also be reproduced by this model. The model developed in this work can be extended to design practical gas filtration

system with pleated MFES. Additionally, this model developed herein may also be employed to other non-catalytic heterogeneous reaction/adsorption processes including but not limited to CO_2 adsorption, H_2S removal.

The uniform flow distributions and negligible bed channeling inherent in MFES lead to superior breakthrough performance compared to a conventional PB. This unique advantage of MFES enhanced the breakthrough performance of the regenerated samples. It is believed that the rigidity of the sinter-locked metal fibers is capable of keeping the bed frozen in place over multiple cycles, significantly reducing flow maldistributions. The 5 wt.% Mn/γ-Al_2O_3 is a promising regenerable sorbent for SO_2 removal. The sorbent maintained its breakthrough capacity after multiple adsorption/regeneration cycles by utilizing the AEG from SOFC with 10 ppm SO_2 challenge. Thus, the sorbent developed in this work entrapped in the stainless steel microfibrous media is applicable for onboard SOFC cathode protection. Further study will be focused on the development of composite beds where MFES works as an efficient polishing layer.

Nomenclature

$a(t)$	activity of the sorbent at time t, assuming $a(0) = 1$
C	SO_2 concentration in adsorbent bed (mol/m^3)
C_o	SO_2 inlet concentration (mol/m^3)
C_{exp}	SO_2 outlet concentration determined experimentally (mol/m^3)
C_M	Mear's criterion, $C_M = \frac{(-r)\rho_b(d_p/2)}{k_c C_{AO}}$
C_{WP}	Weisz Prater criterion, $C_{WP} = \frac{-r_A \rho_b (\frac{d_p}{2})^2}{D_e C_s}$
C_{model}	SO_2 concentration predicted by mathematical model derived in this study at a given time (mol/m^3)
C_s	SO_2 concentration at the sorbent surface (mol/m^3)
D_e	SO_2 effective diffusivity in sorbent pores, $D_e = \frac{D_m \varepsilon \sigma}{\tau}$
D_m	molecular diffusivity of SO_2 in gas mixture (m^2/s)
d_p	mean particle size (m)
D_z	axial dispersion coefficient (m^2/s)
k_o	initial sorption rate constant ($1/s$)
k_c	external mass transfer coefficient (m/s), $k_c = \frac{Sh D_m}{d_p}$

k_d	deactivation rate constant ($m^3/mol/g$)
M_A, M_B	molecular weight of species A and B, respectively (g/mol)
n	number of experimental points
P	pressure (Pa)
Pe_{dp}	particle Peclet number
q	order of deactivation
r_A	measured sorption rate of component A ($mol/g\ sorbent/s$)
Re_{dp}	particle Reynolds number, ($Re_{dp} = \frac{d_p u \rho}{\mu(1-\varepsilon_b)}$)
Sc	Schmidt number, ($Sc = \frac{\mu}{\rho D_m}$)
Sh	Sherwood number
t	time on stream (s)
T	temperature (K)
u	superficial velocity of gas mixture (m/s)
u_{in}	interstitial velocity of gas mixture (m/s)
V_A, V_B	diffusion volume of species A and B, respectively (m^3/mol)
z	axial length (m)

Greek symbols

β	dispersion parameter
ε_b	bed voidage
η	internal mass transfer effectiveness factor
σ	constriction factor
τ	tortuosity factor
μ	gas mixture viscosity (*kg/m/s*)
Φ_1	Thiele modulus for first order reaction
ρ_a	density of gas mixture (kg/m^3)
ρ_b	bulk density of sorbents (kg/m^3)
ρ_s	particle density (kg/m^3)
ζ	function of bed voidage, ($\zeta = (1 - \varepsilon_b)^{1/3}$)
ψ	function of ζ, ($\psi = 2 - 3\zeta + 3\zeta^5 - 2\zeta^6$)

Chapter V Development of High Performance Filtration Systems Using Novel Bed Configuration Design

V.1 Introduction

Solid Oxide Fuel Cell (SOFC) has been widely used in the US military for recent years because of its high power density, high efficiency, and almost zero emissions. However, due to the high sulfur containing fuels utilized in SOFC, a great amount of SO_2 will be released into the atmosphere. The cathode materials of SOFC can be degraded by the SO_2 after combustion over time. It was reported that the cathode of LSCF6428 (one type of SOFC) could be degraded even it was under 0.1 ppm of SO_2 balanced in air [24]. The most straightforward way to address this issue is installing cathode air filters to eliminate the potential contaminant. However, filters to be used for the onboard fuel cell systems need to be optimized. The effectiveness, durableness, and parasitic power loss are the most important considerations for cathode filter design. Usually, higher efficiency and longer breakthrough time result in higher pressure drop, which means more parasitic power loss.

The objective of this work is minimizing the parasitic power loss of the filter and at the same time the filter still possesses its high remove efficiency and breakthrough capacity towards SO_2. Novel filter configuration designs, primarily composite sorbent bed and multi-element structured array (MESA), are employed in this study. A mathematical adsorption model was proposed in this study to describe the gas-solid adsorption process. Breakthrough data was obtained and further used to determine the adsorption parameters (initial sorption rate constant and depletion rate constant). Other operation parameters of a typical SOFC were obtained from the literatures[171,172]. Based on the predetermined kinetics and operation parameters, the relationship between parasitic power loss, filter dimension, and the targeted breakthrough time can be established. Essentially, the optimization process is a trade-off between the power reduction due to the degradation of the cathode poisoning effect and the parasitic power loss originated from the filtration process. The simulation results demonstrated that the overall performance of a SOFC can be warranted by installing air filters.

V.2 Experimental

The experimental setup for breakthrough test and pressure drop measurement is displayed in Fig. 1. Air (breathing quality) was purchased from Airgas Inc., and dehumidified using silica gel. The sources of SO_2 were 50 ppm SO_2-N_2 mixture. The desired SO_2 challenge gases used in this work were prepared by adjusting the flowrates of 50 ppm SO_2-N_2, dry air, and the ultrahigh purity O_2 and N_2. All the gas streams were

controlled by mass flow controllers (Alicat Scientific). The gas mixture was flowing through a mixer before entering the adsorption column. Prior to each test, the challenge gas was passed through the bypass line for 10 min to ensure the compositions of the gas mixture were stable. The SO_2 concentrations were measured at the inlet and outlet by a MultiRAE pro equipped with an SO_2 sensor, which is able to detect SO_2 concentrations down to 0.1 ppm.

The pressure drop across the sorbents/MFES was determined using an Omega differential pressure transmitter (Model No. PX154-025DI). The sorbent of each size range were loaded into a quartz tube. For MFES and composite bed, microfibrous media with entrapped sorbents were stacked layer-by-layer. Air was passed through the packed bed/MFES/composite bed at room temperature. First, the total pressure drops were measured at various face velocities. Then the pressure drop contributed by the setup (e.g. packing materials) was also measured at the same face velocities. The pressure drop generated by the packed bed/MFES/composite bed equals the total pressure drops minus the pressure drops caused by the packing materials.

A series of supported MnO_x and CuO sorbents were prepared via incipient wetness impregnation, using manganese nitrate tetrahydrate (99.99 %, Sigma-Aldrich) and copper nitrate trihydrate (98.0-103 %, Sigma-Aldrich) as a precursor, respectively. γ-Al_2O_3 (pellets, Sigma-Aldrich) as a support was also purchased from Sigma-Aldrich. For sorbent preparation procedure, typically γ-Al_2O_3 was ground and sifted to the desired sizes (250-

420 µm and 88-125 µm). Thereafter, the metal nitrate solution was added onto the support with vigorous stirring at room temperature. The sample was then dried overnight at 120 °C and calcined at different temperatures for 2 h in static air. For example, the sorbent written as 5MnAl-650 denotes 5wt. % Mn was doped on the γ-Al_2O_3 support and calcined at 650 °C for 2 h.

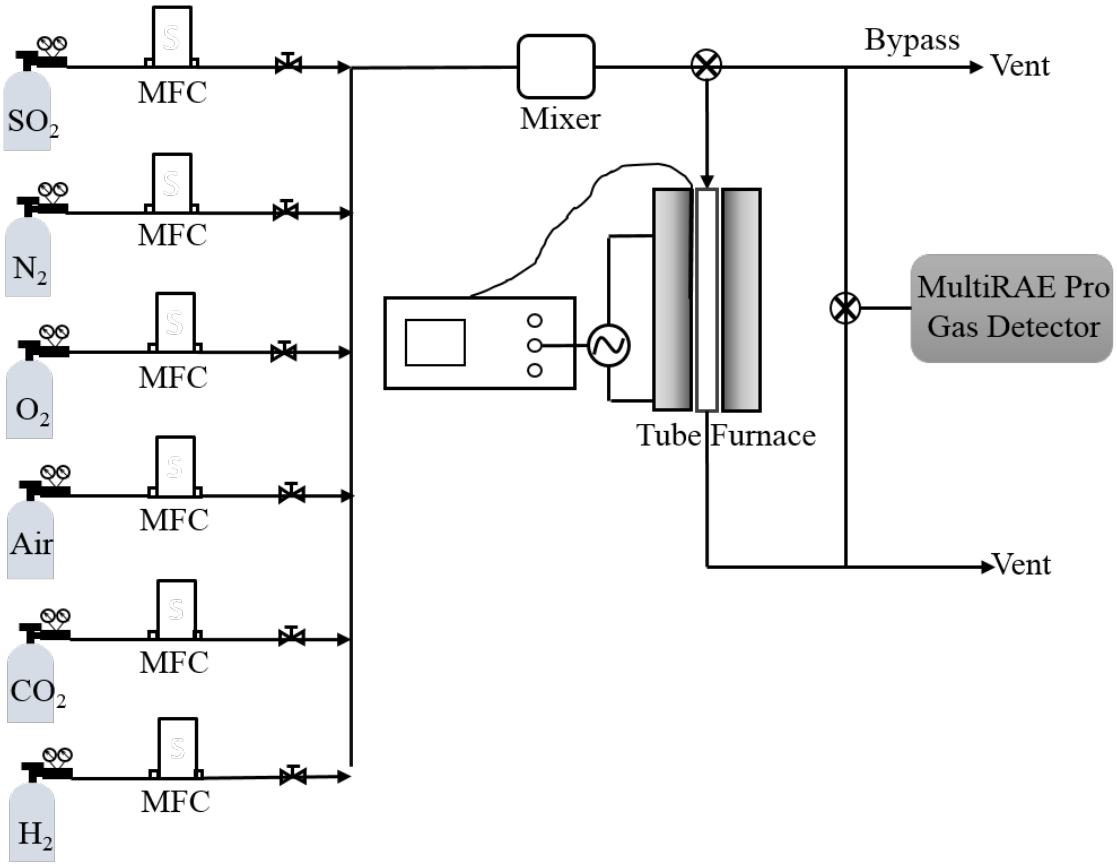

Figure V.1 Schematic diagram of SO_2 adsorption setup. (MFC: mass flow controller)

The SS MFES was manufactured by a conventional wet layup papermaking process. The details of preparing the microfibrous structure can be found elsewhere (citation needed). Then, the calcined sorbents mentioned earlier were dispersed evenly into the fiber matrix.

V.3 Results and Discussion

V.3.1 Active Metal Screening

In this study, γ-Al_2O_3 was selected as the sorbent support due to its high surface area and excellent thermo stability. Other commercial available supports such as SiO_2 and ZrO_2 were also evaluated but the breakthrough capacities were less than γ-Al_2O_3. Three candidates (CuO/ γ-Al_2O_3, MnO_x/ γ-Al_2O_3, and CCP104) were tested at 20 and 200 ^oC, respectively, as shown in Fig. 2. In each breakthrough performance evaluation, a packed bed containing 50 mg of sorbent (bed depth: 5.1 mm) was challenged with 10 ppm SO_2 at a face velocity of 1.33 m/s. The Mn doped on γ-Al_2O_3 demonstrated the highest breakthrough time at elevated temperature (200 ^oC). Although CCP104 possessed longer breakthrough time than MnO_x/ γ-Al_2O_3, the sorbent performance decreased significantly at higher temperature due to the decomposition of $KMnO_4$. Therefore, MnO_x/ γ-Al_2O_3 was chosen for the following investigation.

V.3.2 Effect of Calcination Temperature

The performance of γ-Al_2O_3-supported MnO_x sorbent can be affected by the calcination temperature. It was reported in the literature that MnO_x species with lower

oxidation states (such as Mn_3O_4 and MnO) exhibited better SO_2 removal performance[49]. However, the phase diagram of MnO_x under various temperature and oxygen partial pressure (shown in Fig. S1(a)) suggests that the lower oxidation states of Mn are more likely to be generated at higher temperatures. In addition, high calcination temperature usually causes surface area loss and active species sintering, which is not favorable for gas-solid reaction. Hence, under certain condition, there should be an optimum calcination temperature demonstrating the highest SO_2 breakthrough capacity.

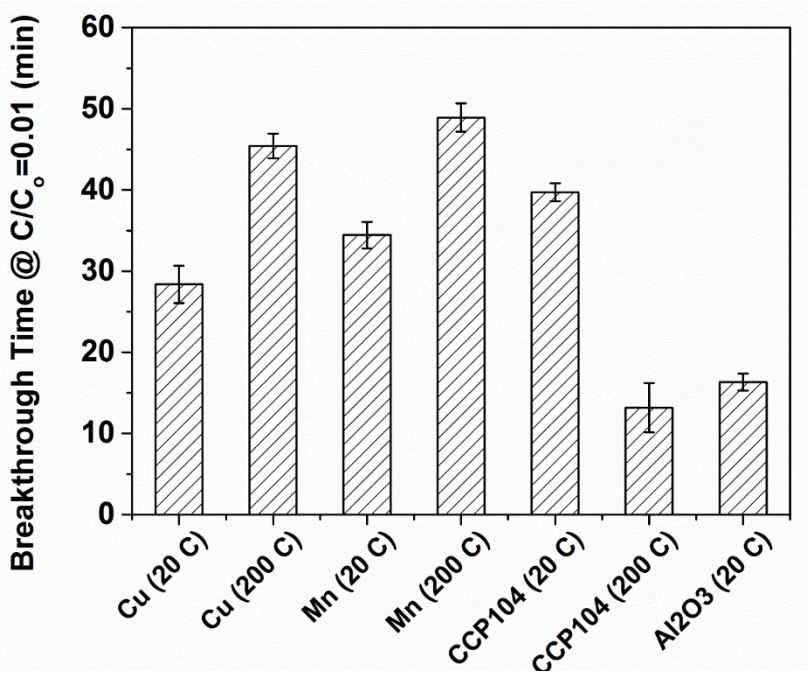

Figure V.2 Active metal screening test. (Cu: 8 wt.% Cu on γ-Al_2O_3; Mn: 5 wt.% Mn on γ-Al_2O_3; CCP104: 4 wt.% $KMnO_4$ on γ-Al_2O_3; Al_2O_3: γ-Al_2O_3 calcined at 650 ^oC.)

(a)

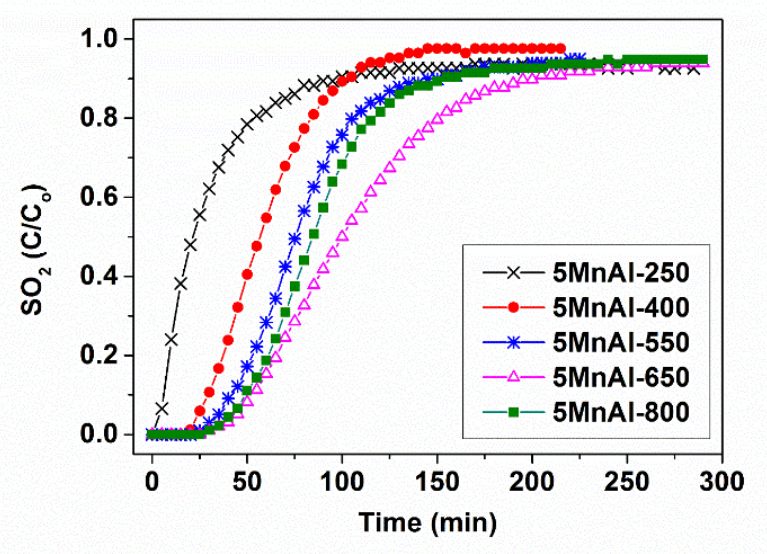

(b)

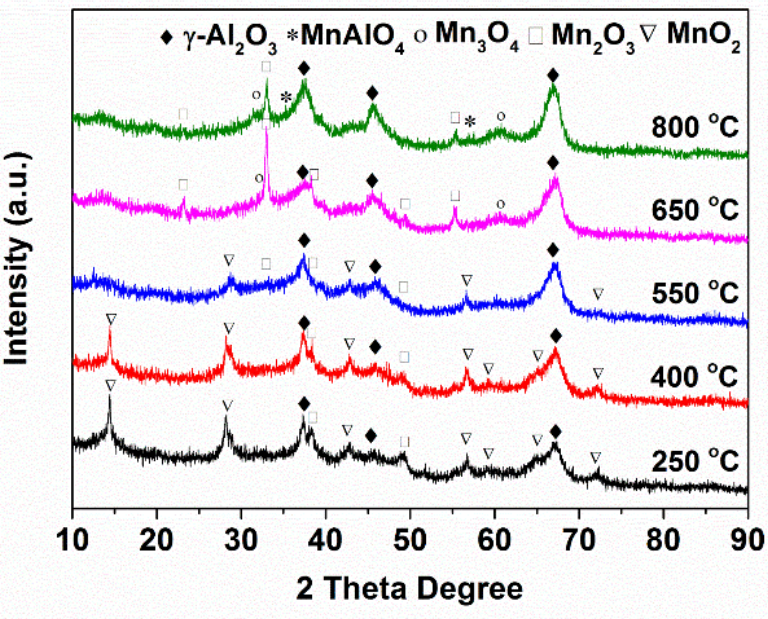

Figure V.3 (a) Effect of calcination temperature on the breakthrough performance for 5 wt.% Mn doped on γ-Al_2O_3; (b) XRD patterns of calcined sorbents.

The breakthrough tests for 5 wt.% Mn on γ-Al_2O_3 are shown in Fig.V.3(a). As mentioned before, 10 ppm SO_2 passed through a packed bed containing 50 mg of sorbent calcined at various temperatures. Apparently, the candidate 5MnAl-650 showed the highest breakthrough time (30.1 min), decreased in the order of 5MnAl-800, 5MnAl-550, 5MnAl-400, and 5MnAl-250. The MnO_x species were verified by XRD. The XRD pattern in Fig. 3(b) indicates that the primary component of 5MnAl-650 is Mn_2O_3, with a small amount of Mn_3O_4. Lower calcination temperature leaded to the tendency of more MnO_2 phases emerging on the γ-Al_2O_3. Higher calcination temperature (i.e. 800 ^oC) resulted in $MnAlO_4$ phases. It was believed that $MnAl_2O_4$ shows low reactivity due to its tetrahedral spinel structure[60]. Further increase the calcination temperature can lead to severe surface area loss and phase transformation of γ-Al_2O_3 to α-Al_2O_3[173]. The five candidates calcined at 250-800 °C do not show much difference in surface area. This indicates that the variation of adsorption performance was predominately due to the reactivity of the active species. Based on the results shown in this part, 5MnAl-650 was employed for the subsequent study.

V.3.3 Microfiber Screening

As discussed earlier, microfibrous entrapped sorbent can promote the sorbent performance due to the reduction of flow maldistribution and axial dispersion. Three different microfibers (glass, Ni, and SS fiber) were tested in this study. Glass fiber was not considered as a candidate because the sinter-lock structure was not able to entrap enough particles after the sintering process. Ni fiber could be oxidized/sulfated in the presence of oxygen when the adsorption process occurred at moderate temperature (i.e. 200 °C).

Furthermore, Ni fiber could also be vaporized in reducing atmosphere when the regeneration temperature was 650 °C, resulting in deposited Ni at the downstream, as shown in Fig. 4(a). At the same time, shrinkage of the Ni-MFES was observed. SS fiber was quite inert and there was no tendency of vaporization. After the first regeneration cycle, the sinter-locked structure of Ni fiber collapsed, as shown in Fig. 4(b). The SS fiber could withstand reducing and oxidizing atmosphere even at high temperatures. Fig. 4(c) shows that the SS fiber could still maintain its original structure after the 5th regeneration cycle. It is desired that the sorbent can be used for multiple cycles to reduce the overall cost. Based on the discussion above, SS fiber is the best choice for SO_2 removal.

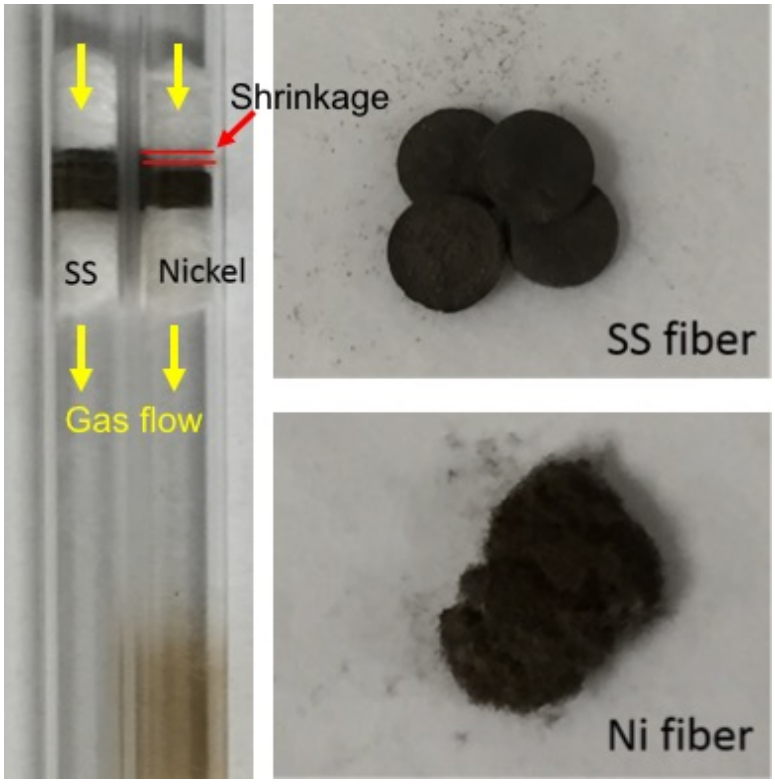

Figure V.4 (a) Comparison of SS and Ni fiber after the 1st regeneration cycle; (b) spent Ni-MFES after the 1st regeneration cycle; (c) spent SS-MFES after the 5th regeneration cycle. (Adsorption condition: 10 ppm SO_2 passed through a fixed bed at a face velocity of 1.37 m/s at 200 °C; regeneration condition: Model AEG passed through the sulfated sample at a face velocity of 0.13 m/s. The reactor I.D. was 6.8 mm.)

V.3.4 Composite Bed

Despite MFES can provide uniform flow pattern throughout the bed and minimize axial dispersion effect, it cannot achieve high breakthrough capacity in terms of per unit volume due to its low sorbent loading[29,145]. Moreover, in order to fulfill a longer breakthrough time

requirement, MFES requires a thicker filter and more parasitic power[23]. The best way to take advantage of the two bed configurations is to construct a composite bed. The breakthrough curves of a packed bed, a polisher layer (1 layer of SS-MFES), and the corresponding composite bed are demonstrated in Fig. 5. The tests were conducted in a quartz tube (I.D. 6.8 mm) with 10 ppm SO_2 at a face velocity of 1.37 m/s at 20 °C. The packed bed was comprised of 150 mg 5MnAl-650 sorbent (particle size: 250-420 μm) with a bed depth of 5.5 mm. The SS-MFES (or called polisher) has a thickness of 2 mm. As shown in Fig. 5, the overall composite bed thickness was 7.5 mm.

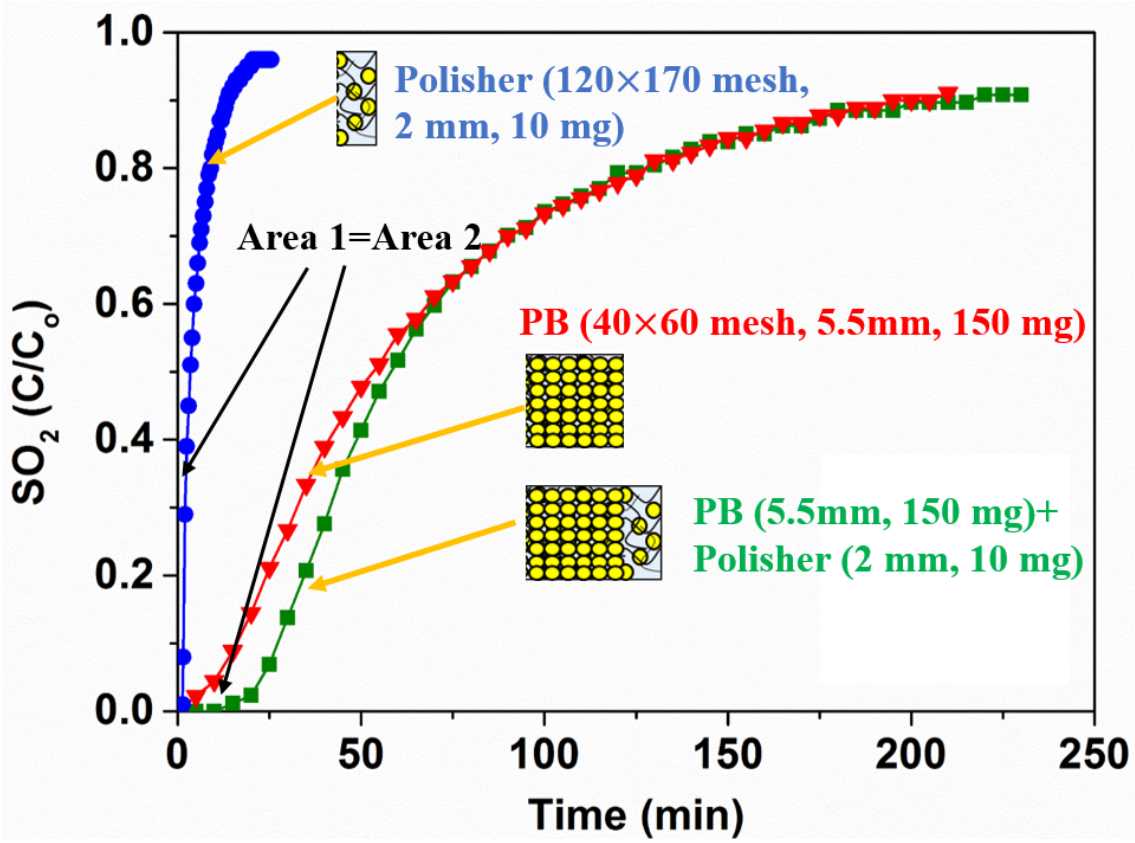

Figure V.5 Breakthrough curves of conventional PB, MFES, and composite bed

V.3.5 Design Algorithm for the Fuel Cell Power System

The mathematical model we proposed in our previous work (citation here) can predict the breakthrough time very precisely. Along with the pressure drop tests and parameters of the fuel cell power system, the design algorithm can be established.

V.3.5.1 Mathematical Model to Predict the Breakthrough Time

Several models can be employed to predict the breakthrough time, such as deactivation model and Yoon-Nelson model. However, the accuracy of the prediction depends on the adsorbate-adsorbent system. In this work, a mathematical model coupled with internal and external mass transfer, axial dispersion, and surface reaction can be utilized to predicted the breakthrough time of the cathode air filter. The governing equation is listed as follows:

$$\frac{\partial C}{\partial t} = D_z \frac{\partial^2 C}{\partial z^2} - \frac{u}{\varepsilon_b}\frac{\partial C}{\partial z} + \left(\frac{1-\varepsilon_b}{\varepsilon_b}\right) \cdot \eta \cdot r_{SO2} \tag{V-1}$$

Based on the operation condition, the initial and boundary conditions are shown below:

I.C. $c(0, z) = 0,$ at $t = 0$ (V-2)

B.C.1. $c(t, 0) = c_0 + \frac{\varepsilon_b D_z}{u}\frac{\partial c}{\partial z},$ at $z = 0$ (V-3)

B.C.2. $\frac{\partial c}{\partial z} = 0,$ at $z = L$ (V-4)

And (put into appendix)

$$\varepsilon_b = 1 - \rho_b/\rho_s \tag{V-5}$$

For this particular adsorption condition, due to the high face velocity flowing through the bed and the small sorbent particles, the external mass transfer resistance can be neglected. For internal mass transfer resistance, Weisz Prater criterion can be applied to calculate the internal effectiveness factor (η). See Appendix for derivation details.

The axial dispersion effect in this work cannot be completely ignored, especially for the packed bed. The coefficient of axial dispersion (D_z) can be estimated by the following semi-empirical equations[174]:

$$D_z = 0.73D_m + \frac{0.5u_{in}d_p}{1 + \beta\frac{D_m}{u_{in}d_p}} \tag{V-6}$$

$$Pe_{dp} = \frac{ud_p}{\varepsilon_b D_z} \tag{V-7}$$

Fuller's method can determine the molecular diffusivity (D_m) of SO_2 in the gas mixture, more details are listed in the Appendix.

Since the main active species presented on the substrate are Mn_2O_3 (Based on the XRD result), it is postulated that the following reaction occurred on the gas-solid interface:

$$SO_{2(g)} + \frac{1}{2}Mn_2O_{3(s)} + \frac{1}{4}O_{2(g)} \rightarrow MnSO_{4(s)} \tag{V-8}$$

In our previous work (reference needed), the following kinetic relationships can be used to describe reaction in equation (7), and the assumptions are listed in the Appendix:

$$-r_{SO2} = k_o \cdot a(t) \cdot C \tag{V-9}$$

$$-\frac{d[a(t)]}{dt} = k_d \cdot C^m \cdot [a(t)]^q \tag{V-10}$$

Based on the discussions above, the governing equation can be derived as follows:

$$\frac{\partial C}{\partial t} = D_z \frac{\partial^2 C}{\partial z^2} - \frac{u}{\varepsilon_b}\frac{\partial C}{\partial z} - (\frac{1-\varepsilon_b}{\varepsilon_b}) \cdot \eta \cdot k_0 \cdot a(t) \cdot C \tag{V-11}$$

The partial differential equation could be solved by MATLAB numerically. By fitting the experimental data (under certain conditions) to the calculated results, the independent parameters k_o and k_d can be determined by minimizing the residual sum of squares. For specific operation conditions, the breakthrough time can be estimated by the calculated results.

V.3.5.2 Pressure Drop Relationship between Filter Thickness and Face Velocity

There are a lot of models to correlate pressure drop with face velocity, bed depth, and void fraction. For example, Ergun equation is usually employed to describe the flow through a packed bed; porous media permeability (PMP) equation is commonly used for a fixed bed when the voidage is higher than 50 %[175]. The relationship between pressure drop, filter thickness, and face velocity can be established by measuring pressure drop as a function of thickness and face velocity. Compared with Ergun and PMP equation, this empirical method is more straightforward and the parameters are easier to be determined. The equation is shown as follows:

$$\Delta P = A_1 L u + A_2 L u^2 \tag{V-12}$$

V.3.5.3 Equations of the SOFC Attributes and Filter Parameters

The following discussion involves the mathematical relationships that describe the SOFC attributes and the filter configurations. Air flow rate of the fuel cells, power of the compressor based on the inlet and outlet attributes, and fuel cell efficiency will be included.

It was derived in Larminie and Dick's book (Fuel cell systems explained, 2nd edition) that the air usage of a typical fuel cell system can be expressed by the following equation (provided that the oxygen molar proportion in air is 0.21 and the molar mass of air is 28.97 kg mol^{-1}):

$$Air\ usage = 5.1 \times 10^4 \times \lambda \times \frac{P_e}{V_c}\ (L\ min^{-1}) \tag{V-13}$$

where P_e is the output of the fuel cell system; V_c is the average voltage through a fuel cell stack. Values between 0.6-0.7 V can be used to represent a typical fuel cell during operation. In this work, 0.65 V was used as a voltage approximation; λ is the stoichiometric ratio (defined as the ratio of total amount of air to the spent air), which is usually 2 for SOFC system.

The compressor parasitic power is shown as follows:

$$P_0 = \frac{\gamma}{\gamma - 1} \times \frac{0.37 T_i}{\eta} \times q_1 \times \left[\left(\frac{P_2}{P_1}\right)^{\frac{\gamma-1}{\gamma}} - 1\right] \tag{V-14}$$

where P_0 is the fuel cell output (kW); γ is the heat capacity ratio (1.4); T_i is the temperature of gas entering the compressor (K); η is the compressor efficiency, which is 0.7 assumed

in this work; q_1 is the volume of gas compressed evaluated at 293 K; P_1 and P_2 are the compressor inlet and outlet pressure (Pa), respectively.

We can also obtain the efficiency of a compressor by employing compressor performance charts. The efficiency of a certain compressor can be determined by the performance chart once given the operation gas flow rate and pressure ratio. For a centrifugal compressor, the highest efficiency can be achieved is around 0.7-0.8, in this work, a value of 0.7 is used.

V.3.6 Case Study of Various Adsorption Bed Configurations

The aforementioned cathode air filter design algorithm was used to a 60 kW output SOFC. In this section, we investigated the parasitic power loss and filter thickness in the configuration of packed bed, MFES, and composite bed. The SOFC system parameters are listed in Table V.1. In the case study, the MFES as well as the polish layer consists of 88-125 μm $5MnO_x/Al_2O_3$ sorbents and the packed bed is composed of the same sorbents but the particle size fell in the range of 250-420 μm. Using these parameters provided and the mathematical equations discuss above, for a certain target of removal efficiency, the parasitic power loss for a 60 kW SOFC can be estimated based on different breakthrough time requirements. The pressure drop data was obtained by differential pressure gauges. For a real condition, the air flow rate and cross section area were assumed 3600 L min^{-1} and 0.045 m^2, respectively.

Table V.1 60 kW SOFC Operation Conditions

Temperature (K)	293	Stoichiometric ratio	2.0
Air flow rate ($L\ min^{-1}$)	3600	Average voltage (V)	0.65
Cross section area (m^2)	0.045	SOFC output (kW)	60
SO_2 inlet concentration (ppm)	10	SOFC inlet pressure (atm)	2.0

Totally three cases (in terms of different inlet and outlet concentrations) were investigated in this research. The three cases are as follows:

(1) Case I: 100 – 0.1 ppm;

(2) Case II: 10 – 0.1 ppm;

(3) Case III: 5 – 0.01 ppm;

For case I, the estimated predicted parasitic power loss for a filter to fulfill the targeted breakthrough time was shown in Figure V.6. This case represents a 3 log removal and requires a relatively high capacity. Because of the high capacity requirement, the PB and CB are much better choice in terms of compressor power. MFES is not effective in reducing the parasitic power when the inlet concentration is high.

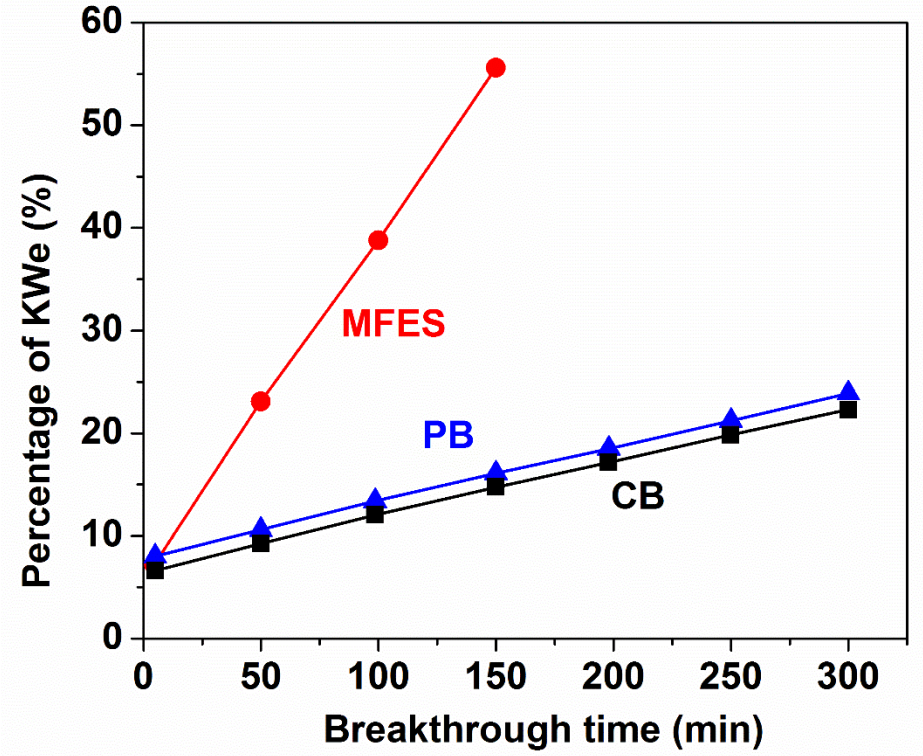

Figure V.6 Estimated parasitic power loss to fulfill different breakthrough time requirements. (Breakthrough point is defined at $C/C_0 = 0.01$, removal from 100 ppm SO_2 to 0.1 ppm)

When the we decreased the inlet concentration (For case II), the advantage of using MFES came out. As shown in Figure V.7, when the required breakthrough time is less than 10 min, MFES is the material that introduces the smallest parasitic power loss. Hence, for short term SOFC cathode protection, MFES is the best choice in terms of lowering the parasitic power. On the other hand, when the SOFC system requires longer protection period, composite bed is the best option to reduce parasitic power loss. As we discussed in

Chapter IV, since MFES can provide uniform flow throughout the adsorption bed, the negative effects such as flow maldistribution could be minimized. However, the microfibrous structure could also introduce additional pressure drop, and the MFES usually contains much less sorbents per unit volume. Hence, when longer period of breakthrough time is required, the advantage of MFES could not offset its drawbacks.

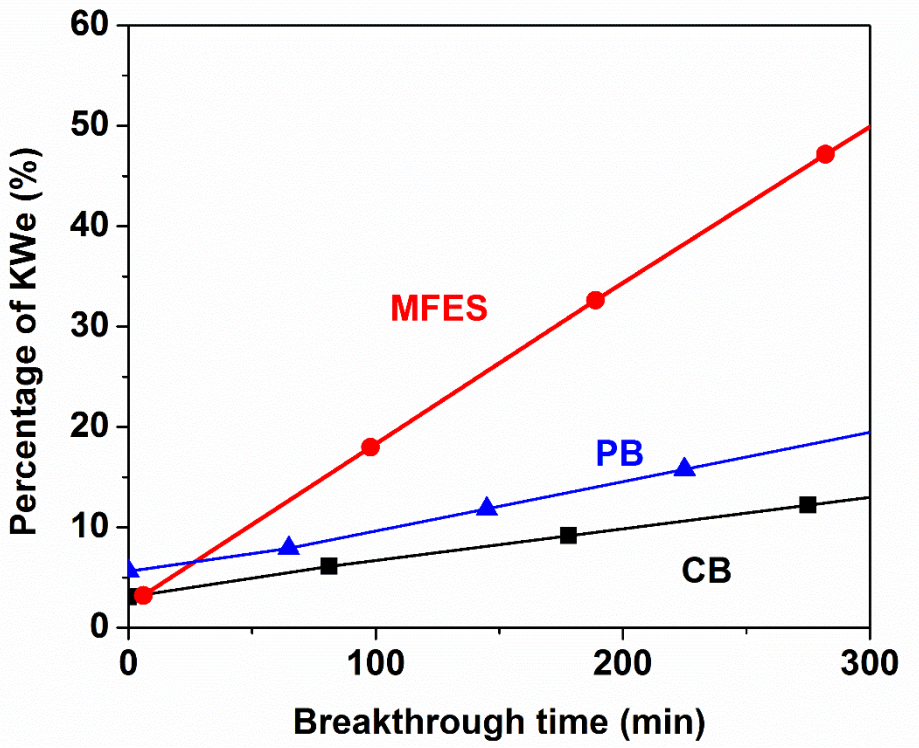

Figure V.7 Estimated parasitic power loss to fulfill different breakthrough time requirements. (Breakthrough point is defined at $C/C_0 = 0.01$, moval from 10 ppm SO_2 to 0.1 ppm)

The last scenario, shown in Figure V.8, indicates that the functionality of MFES was more significant than the case in Figure V.7. It is obvious that microfibrous materials cost the least parasitic power in the presence of air filter if the desired breakthrough time is less than 25 min. However, as the required breakthrough time increases, CB becomes the best choice for the fuel cell system. When the required breakthrough time is over 50 min, it can be seen that the MFES would consume the highest parasitic power. Hence, based on different breakthrough time requirements, totally different bed configuration should be applied.

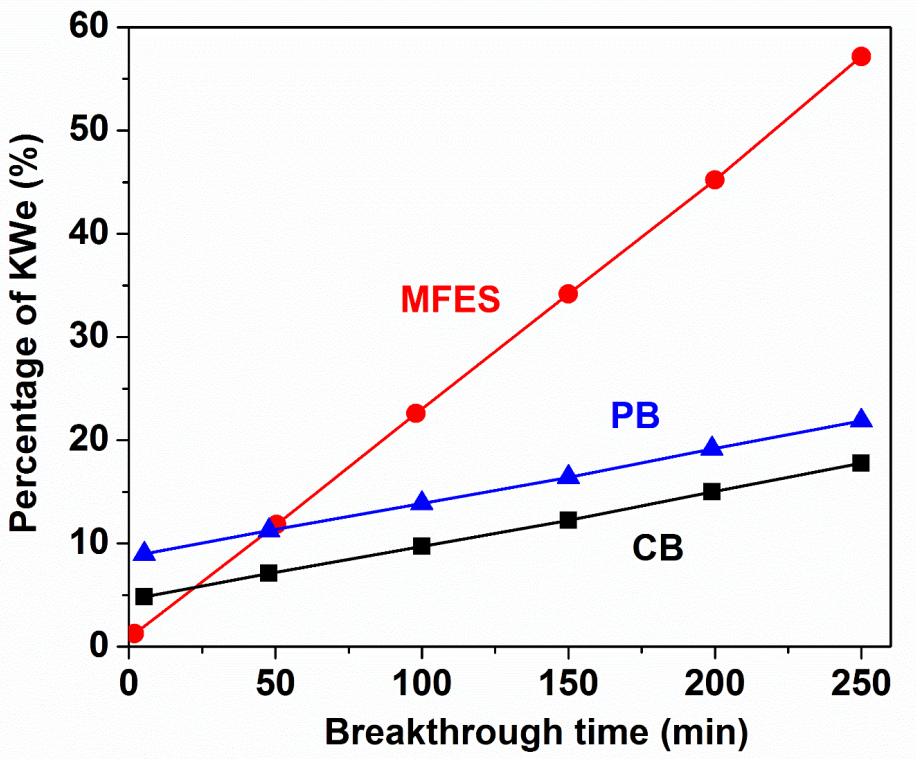

Figure V.8 Estimated parasitic power loss to fulfill different breakthrough time requirements. (Breakthrough point is defined at $C/C_0 = 0.01$, removal from 5 ppm SO_2 to 0.01 ppm)

V.4 Conclusion

In this work, experimental data and mathematical estimation were combined to predict the parasitic power loss in a polluted environment. The prediction can provide a guide about how to choose the best filter configuration to achieve the best fuel cell performance. In this model, most parameters were obtained in the literature or estimated based on a reasonable range.

The simulation results presented in this work indicated a strategy for SOFC cathode protection. Composite bed is the best option since for traditional fuel cell systems, long term protection or longer breakthrough time is our target (most fuel cell systems requires thousands of hours' operation time). The simulation is also important for us to understand the internal working mechanism between the fuel cell stack and its balance of plant components.

Chapter VI PPB-Level Contaminant Removal for Proton Exchange Membrane Fuel Cell (PEMFC) Cathode Air Protection

VI.1 Introduction

Fuel cells are widely used in the modern society. They possess various advantages compared to conventional power sources (internal combustion engines and batteries). The advantages include: 1) fuel cells have a higher efficiency than conventional diesel or gas driven engines; 2) fuel cells have extremely low emissions compared with other engines burning fossil fuels; 3) operating period is much longer than batteries; 4) easy to scale up and good for design and packing.

For low temperature fuel cells (PEMFC), they have low heat generation which makes them ideal for military applications. As shown in Figure VI.1, the PEMFC uses a water-based or mineral acid-based polymer membrane as its electrolyte. Usually PEMFC operates at 20-100 °C so that metal catalysts (e.g. Pt) are used as electrodes to address the sluggish reaction rate. Because of the Pt electrodes, the PEMFC is very vulnerable to gas phase contaminants (e.g. SO_2, NO_x, CO, VOCs, etc). In the old days, the Pt loading is high thus the cost of PEMFC is mainly due to the catalyst. Nowadays, since the development of the membrane technology, low Pt loading is allowed (0.2-1.0 mg/cm^2).

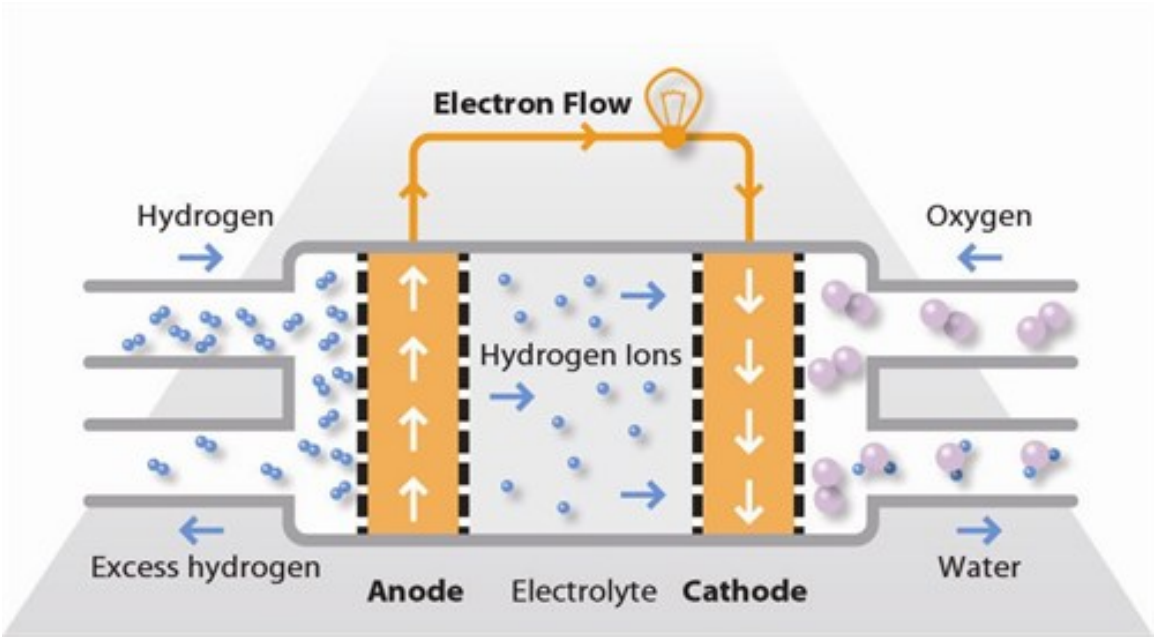

Figure VI.1 Schematic of PEMFC (the anode uses hydrogen as fuel)

For naval ship platforms, the effect of atmospheric impurities cannot be eliminated. VOC is a very common impurity which exists both indoor and outdoor. For the onboard atmosphere, VOC is unavoidable due to the use of fossil fuels and human activities. It was reported that the cell performance underwent a significant decrease in terms of cell voltage when toluene was present in the air stream (5 ppm toluene in air). Furthermore, the poisoning effect was intensified as current density and toluene concentration increase. There are some other factors that have influences on the severity of performance degradation, such as back pressure, air stoichiometry, current density cycling, and so on. Hence, it is vital to remove the VOCs before they enter the cathodes. This work mainly focuses on the cathode air purification of PEMFC.

VI.2 Experimental

VI.2.1 Sorbents Preparation

The sorbents used in this work were primarily activated carbon (AC) and modified activated carbon (MAC). Two types of AC were used: 1) BPL was purchased from Calgon Carbon Corporation (Pittsburgh, PA); 2) Ecosorb CT was purchased from JACOBI (Columbus, OH). All the samples were ground and sieved using US standard sieves to obtain the particle size range from 180-250 μm. Before the breakthrough experiments, each sample was dried in a convection oven at 373 K for at least 24 h, followed by storing in an air tight vial.

The MAC was prepared by "KOH activation" method. About 2 g of AC was mixed with certain amount of KOH and H_2O. Then the suspension was transferred into a Teflon beaker. The suspension was heated at 333 K for 2 h on a hotplate. The resulting slurry was dried in a convection oven at 383 K for 24 h. Afterwards, the sample underwent carbonization.

The carbonization process was carried out in a vertical quartz tube which was placed in a box furnace. The aforementioned sample was transferred into the vertical quartz tube supported by quartz wool on both sides. The sample was heated from room temperature to 1023 K (ramp rate was 5K/min). After reached 1023 K, the temperature was further hold for additional 1 h. During the whole process, 500 mL/min of UHP nitrogen was flowing to

ensure a nitrogen atmosphere. The pyrolyzed sample was washed several times with 1M solution of HCl and then with distilled water. Finally, the sample was outgassed in vacuum at 383 K for 12 h and sealed in a vial prior to breakthrough test.

VI.2.2 Characterization of Sorbents

The BET surface area and pore size distribution of all the samples were tested by N_2 physical adsorption at 77 K using Autosorb-1 (Quantachrome Instruments). The BET surface area was calculated at p/p_0 from 0.1 to 0.35 at the adsorption branch. The pore size distribution was calculated based on the BJH method from the N_2 adsorption isotherms.

VI.2.3 Breakthrough Test

The setup for evaluating the breakthrough performance of the sorbents is shown in Figure VI.2. Compressed house air was treated by oil trap and desiccant before it was introduced into the system. A syringe pump was used to deliver the toluene. A portion of air stream was purging the needle of the syringe in order to vaporize the liquid phase toluene. There was also a bubbler to introduce moisture into the system. The moisture content (or RH) can be adjusted by changing the flow rate of that particular MFC. The breakthrough test was conducted at 298 K. So the test section was placed in a temperature controlled oven. About 0.1 g sorbent was used for each test. A glass tube (24 mm long, 9.4 mm I.D.) was used. The sorbent was supported by glass beads and quartz wool. The challenge gas (the face velocity is 96 cm/s) to the mixer initially passed through a preheating section to the desired temperature before it entered the adsorption column. All

of the tests were conducted in a vertical adsorption column and the gas mixture flowing in the downward direction.

To measure the concentration of the toluene in sub-ppm level, we used a GC-FID equipped with a 100 mL sampling loop. The time for the loop to collect the gas sample was set to 5 min, which allows sufficient time for pre-concentration process. The detection limit of this method can be around 5 ppb.

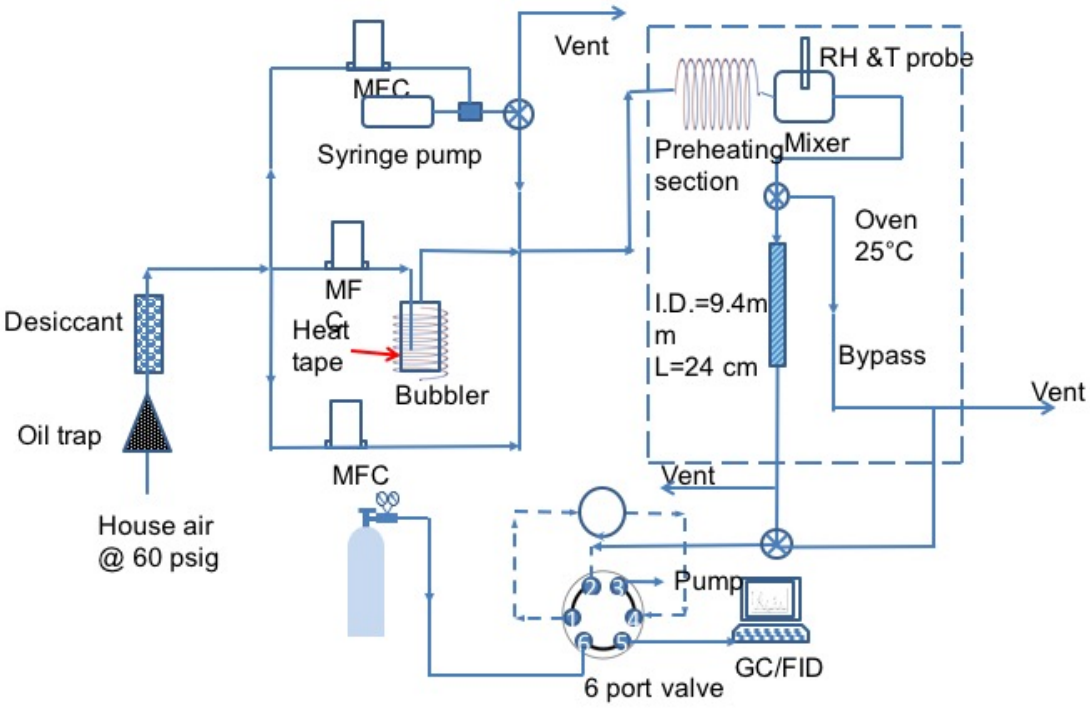

Figure VI.2 Schematic of the breakthrough setup for toluene adsorption

Each breakthrough test was performed by passing the challenge gas mixture and the outlet toluene concentration was measured every 5 min till the concentration of outlet reached the same level of inlet. For the breakthrough tests with moisture, the adsorbents

were initially pre-saturated in humid air (at desired RH). Then the challenge gas was introduced into the gas mixture.

VI.3 Results and Discussion

VI.3.1 Effect of RH on Adsorbent Performance

Since the PEMFC is usually operated in the presence of moisture, we investigated the adsorbent performance under different relative humidity (RH). We firstly applied two commercially available AC to evaluate their performance: Ecosorb CT and BPL. The breakthrough and saturation capacity are shown in the following pictures.

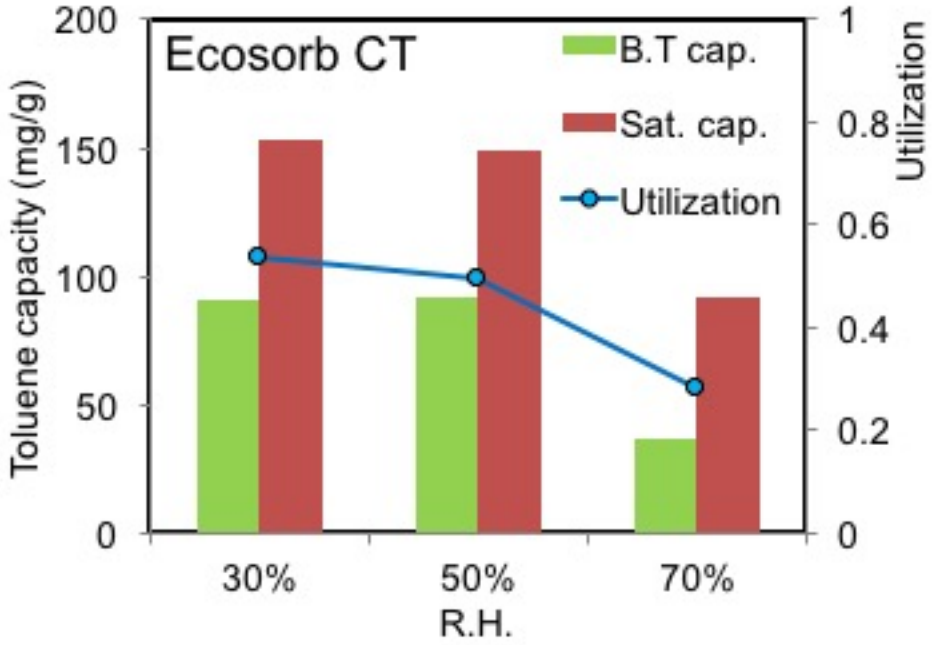

Figure VI.3 Breakthrough capacity and saturation capacity of Ecosorb CT. (Sorbent weight: 0.1 g; Particle size: 180-250μm; Bed depth: 3.5 mm; Inlet toluene concentration: 2 ppm)

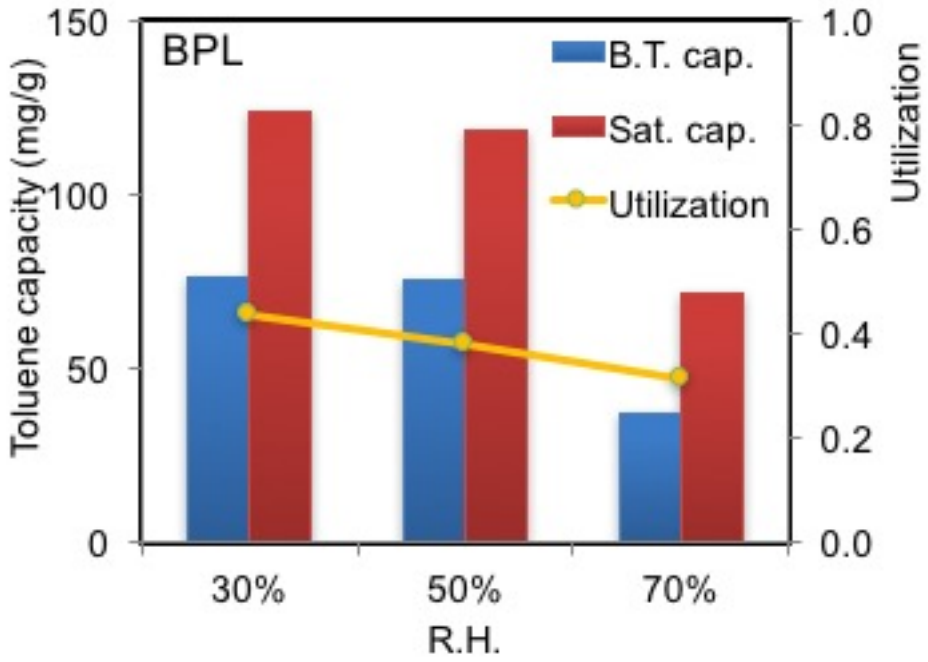

Figure VI.4 Breakthrough capacity and saturation capacity of BPL. (Sorbent weight: 0.1 g; Particle size: 180-250μm; Bed depth: 3.5 mm; Inlet toluene concentration: 2 ppm)

It can be seen from Fig. VI.3 and Fig. VI.4 that when the relative humidity was increased, the breakthrough capacity and saturation capacity was also decreased. There was minor deviation between 30 % RH and 50 % RH. However, when the RH increased to

70 %, significant capacity loss was observed. This is due to the capillary condensation caused by the high RH. As we know, the mechanism of toluene adsorbed on the AC is physisorption. However, the water molecules can occupy the adsorption sites for the toluene be captured. The higher the RH, the less adsorption sites could be available on the AC. The solubility of toluene in water could be neglected (0.5 g/L). Therefore, higher RH hindered the performance of AC.

VI.3.2 Yoon and Nelson Model for the Adsorption Process

There are several mathematical models can be used to describe the process of hydrocarbons adsorb on the AC, such as Mechlenburg model, Amundson model, Wheeler model, and Yoon & Nelson model. Among them, the Yoon and Nelson model is the most widely used for activated carbon. The equation VI-1 reveals the relationship between time and concentration.

$$t = \tau + \frac{1}{k} \cdot ln \frac{C_{out}}{C_{in} - C_{out}} \quad \text{(VI-1)}$$

where,

C_{in}= Inlet concentration of adsorbate, mg/L;

C_{out}= Outlet concentration of adsorbate, mg/L;

τ= Time required to achieve 50 % adsorbate breakthrough, min;

k= Rate constant, min^{-1};

The Fig. VI.5 and Fig. VI.6 shows the comparison between experimental data and simulated result calculated by the Yoon and Nelson model. We can see that the model can fit the experimental data very well. Also, there is minor difference in k when we only changed the RH value.

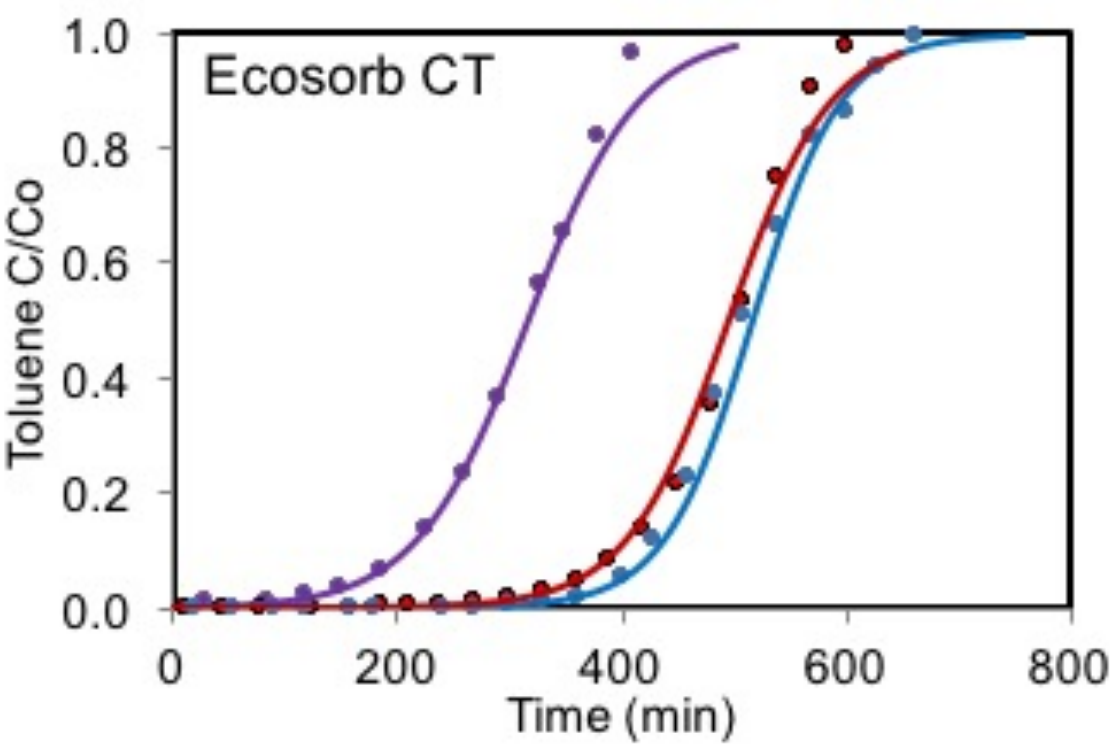

Figure VI.5 Comparison of experimental data (dots) and simulated breakthrough curves (straight lines) for toluene adsorbed on Ecosorb CT. (Sorbent weight: 0.1 g; Particle size: 180-250μm; Bed depth: 3.5 mm; Inlet toluene concentration: 2 ppm)

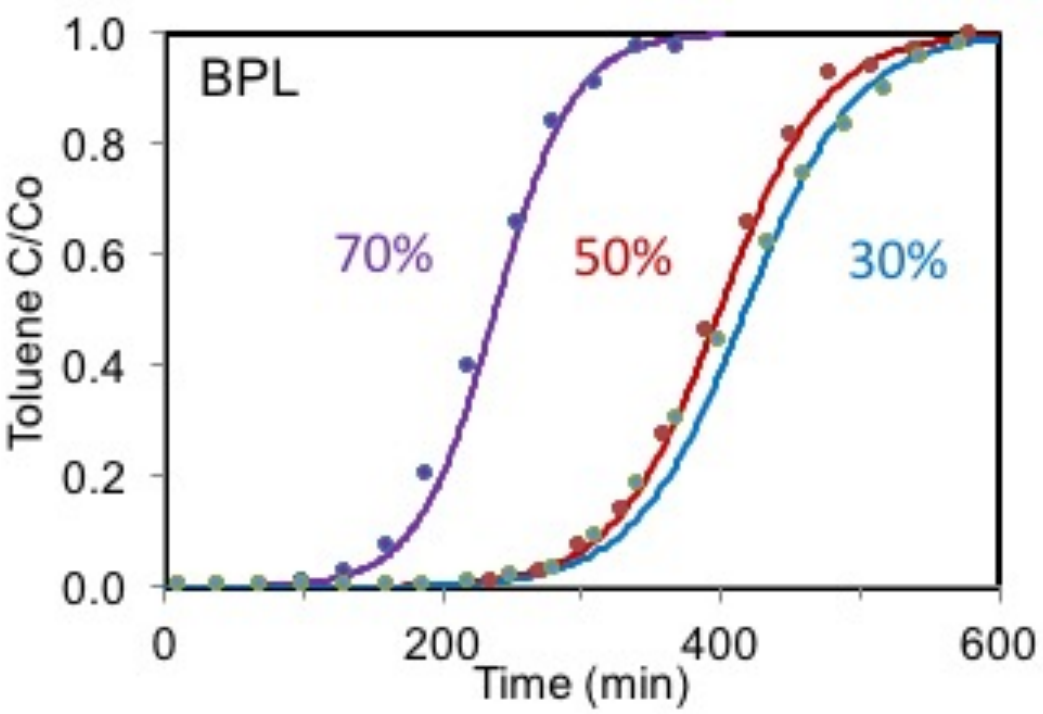

Figure VI.6 Comparison of experimental data (dots) and simulated breakthrough curves (straight lines) for toluene adsorbed on BPL. (Sorbent weight: 0.1 g; Particle size: 180-250μm; Bed depth: 3.5 mm; Inlet toluene concentration: 2 ppm)

VI.3.3 Optimization of AC by KOH Activation

In order to further enhance the performance of the adsorbents, we used a chemical method to modify the morphology of the AC. Since BPL is a coal-based activated carbon, it is easy to alter the surface morphology. Table VI.1 shows various chemical activation methods for BPL. It is shown that the BPL treated with 8 g KOH and 10 g H_2O possessed the highest micropore surface area, which is favorable for toluene adsorption. We also tested the breakthrough performance for the original BPL, Ecosorb, and the modified BPL (Shown in Fig. VI.7). Compared with the original BPL, the modified BPL demonstrated 60 % more breakthrough capacity, though the bed depth of modified BPL increased by 30 %.

Table VI.1 Surface Morphologies of Various Chemical Activation Routes

Samples	S_{BET} (m^2/g)	S_{micro}(m^2/g)	V_{total}(cm^3/g)	V_{micro}(cm^3/g)
BPL	1165	701	0.76	0.60
BPL-8-40	1612	1492	0.94	0.77
BPL-6-10	2007	1870	1.17	0.97
BPL-8-10	2315	2143	1.35	1.11

Note: BPL-8-40 represents 2g BPL was impregnated with 8 g KOH and 40 g H_2O. The detailed method was described in the experimental section.

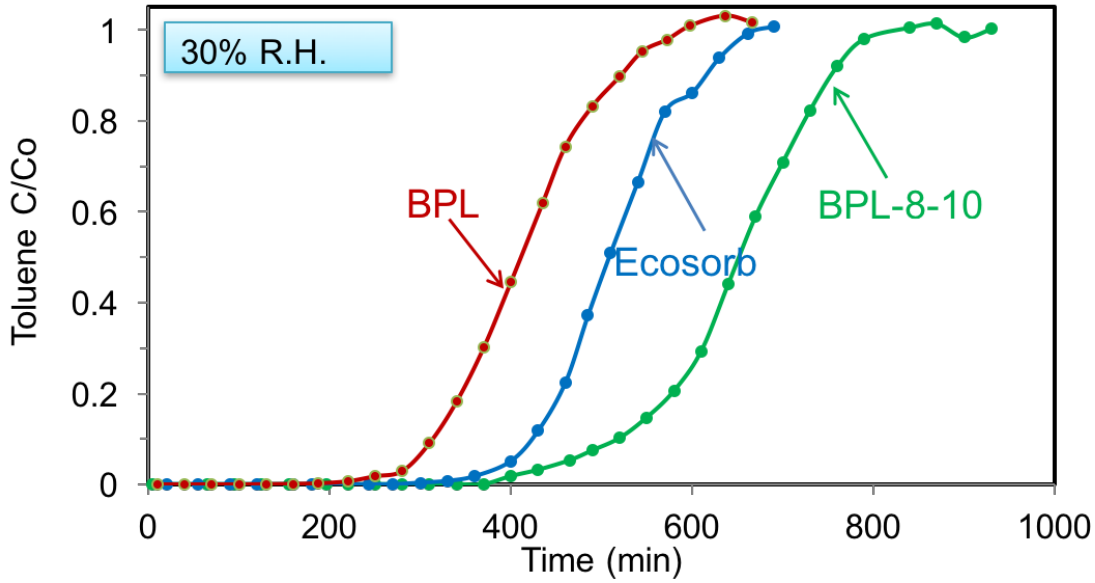

Figure VI.7 Breakthrough curves of BPL, Ecosorb, and modified BPL at 30 %RH. (Sorbent weight: 0.1 g; Particle size: 180-250μm; Inlet toluene concentration: 2 ppm)

VI.4 Conclusion

Based on the results shown in this chapter, we can see that RH is a vital factor in the process of VOC removal. Owing to capillary condensation, higher RH would reduce the effective adsorption sites, thus decreasing the breakthrough capacity. The Yoon and Nelson model can simulate the physisorption process very precisely. Potentially, this model can predict the breakthrough behavior by knowing the predetermined value (τ and k).

By applying the KOH chemical activation method, the micropore surface area could be increased significantly, which is favorable for the toluene adsorption. The modified AC, BPL-8-10, demonstrated the best breakthrough performance among all the other samples.

Chapter VII Recommendations for Future Works

VII.1 Cathode Filtration System Design and Optimization of Solid Oxide Fuel Cells

VII.1.1 Background

Solid Oxide Fuel Cells (SOFCs) technology has been under development for many applications. Because of its fuel flexibility, SOFC can provide clean electricity from a number of hydrocarbon fuels. The scope of SOFC application includes but not limited to portable devices, small-scale power systems (e.g., 5 kW residential power or vehicle auxiliary power units), and distributed generation power plants (e.g., 100-500 kW systems). Furthermore, SOFCs can be integrated with a gas turbine (GT) to build pressurized hybrid systems, whose energy efficiency is much higher (ca. 70 %).

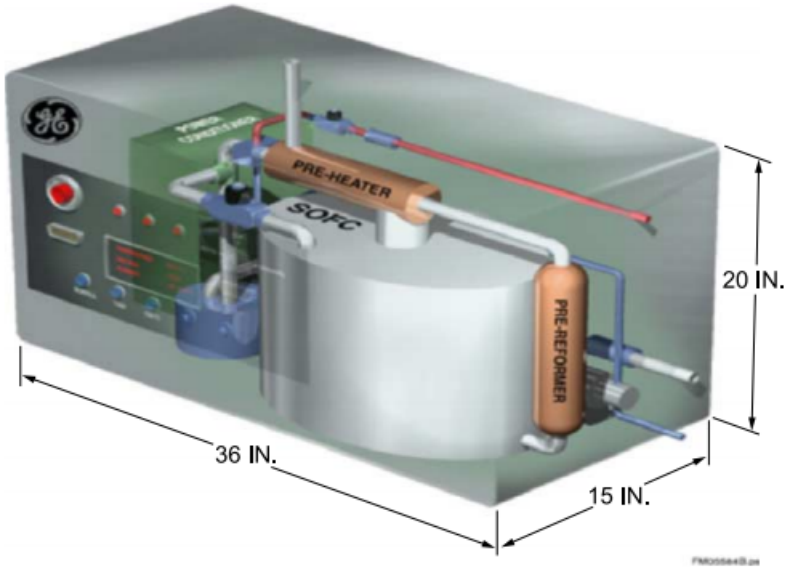

Figure VII.1 SOFC power system (5 kW) [23].

An example of 5 kW power system for stationary applications is shown in Fig. VII.1. The system is comprised of SOFC stacks, fuel processing subsystem, fuel, oxidant delivery subsystem, thermal management subsystem, as well as control and regulating accessories. Additionally, this is usually operated on logistic fuels (JP-8) for military applications. Due to the combustion of high sulfur containing hydrocarbon fuels, such as JP-8 and marine diesel fuels, the performance of SOFC is challenged by the air quality result from sulfur-poisoning. Given the complexity of contaminant species in air stream, the most straightforward solution to mitigate the poisoning effect is employing cathode filtration technique. On the other hand, cathode filter introduces additional pressure drop, which result in observable parasitic power loss. This issue will cause reduction of net power output of SOFC. In general, in consideration of system variety, total system parasitic power loss can be up to 10-20 % of net power output.

Larger scale system, such as Multi-MW SOFC/GT hybrid system, is usually operated in a pressurized environment. The high pressure will further increase the power consumption of the compressor. Therefore, large scale systems (e.g., 100-250 kW combined heat and power SOFC system or SOFC/GT hybrid system) generally bear higher percentage of parasitic power loss. Hence, optimization of cathode filter system is extremely important in terms of enhancing the total efficiency of SOFC.

VII.1.2 Hypothesis

Because of the tradeoff of contamination loss and parasitic loss, there exist an optimum filtration design that can maximize the net power output of SOFC. There are many variables (e.g. operation temperature, pressure, stoichiometric ratio, flow rate, sulfur tolerance, cathode materials, air property, etc.) determining the "sweet spot" of cathode filter configuration. Considering all the operation conditions and parameters of fuel cell, it is viable to develop an optimization procedure to find the optimum point of fuel cell design.

VII.1.3 Experimental and Approach

(1) Filter breakthrough time prediction. The breakthrough time can be predicted by either empirical or theoretical models. Empirical models include Amundson model, Yoon and Nelson model, and Wheeler's model. Theoretical models consist of grain model[149–151], unreacted shrinking core model[130,133,149,152], deactivation model[153–158], random pore model[131], non-ideal adsorption model[129,159], and surface coverage model[160]. A modified deactivation model was applied to predict the breakthrough time in this study. The model parameters (k_o and k_d) were obtained with the help of MATLAB based on Nelder-Mead search algorithm. Other physical parameters are based on filter attributes and air property, including cross-sectional area, filter bed depth, sorbent weight, inlet face velocity, SO_2 concentration, and bed voidage.

(2) Pressure drop model. The pressure drop of conventional packed bed can be estimated by Ergun equation.

$$\frac{\Delta P}{L} = 150\left(\frac{\mu v_0}{d_p^2}\right)\frac{(1-\varepsilon)^2}{\varepsilon^3} + 1.75(\frac{\rho v_0^2}{d_p})\frac{1-\varepsilon}{\varepsilon^3}$$

Due to high voidage of microfibrous media (ε_b>0.5), Ergun equation is no longer applicable in high bed voidage range. Therefore, porous media permeability (PMP) equation has been used to predict the pressure drop of MFES/composite bed.

$$\frac{\Delta P}{T} = 72\frac{\tau^2}{cos^2\theta}\frac{\mu v_0(1-\varepsilon)^2}{\varepsilon^3}\cdot\left[\left(\sum\frac{x_i}{\phi_i D_i}\right)^2 + x_{FD}\sum\frac{x_i}{(\phi_i D_i)^2}\right] +$$

$$6\frac{\tau^3}{cos^3\theta}\frac{\rho v_o^2}{2}\frac{(1-\varepsilon)}{\varepsilon^3}\cdot[C_f + C_{FD}\frac{\varepsilon}{4}]\sum\frac{x_i}{\phi_i D_i}$$

The PMP equation takes form drag losses omitted in Ergun equation into account, which gives an adequate accuracy in predicting the pressure drop of microfibrous media/composite bed.

Another way to predict the pressure drop across the filter is using the empirical equation, which is called Darcy-Forchheimer law.

$$\Delta P = A\cdot u + B\cdot u^2$$

The value of A and B can be predetermined by experimental pressure drop data. This empirical method is handy to use. In addition, cumbersome physical parameter determination is no longer necessary.

VII.2 Pleated Filter Design

VII.2.1 Background

Although MFES, as discussed earlier, can achieve uniform flow pattern and reduce axial dispersion effect throughout the adsorbent bed, it cannot provide high capacity due

to its low sorbent loading per unit volume. MFES has a great potential for removing low concentration gas-phase contaminant. On the other hand, packed bed, despite its flow channeling and higher degree of axial dispersion, it possesses higher breakthrough capacity and saturation capacity per unit volume. As a result, MFES can be employed as a polishing sorbent layer placed behind the packed bed that is named as composite bed (shown in Figure VII.2). It is postulated that one or several layers of polishers are able to extend the breakthrough time significantly while the overall bed thickness increases marginally. Referring to Figure VI.3, because of small particles entrapped into MFM, the breakthrough curve of polisher is very sharp. In contrast, the breakthrough curve of packed bed with larger particles is gentle. Combining the features of MFES and PB result in observable increase of breakthrough time (t_b). The "slope" of the breakthrough curve of composite bed is much sharper than that of PB, which is indicative of the presence of polisher.

Still further, since pressure drop and filtration efficiency trade-off against one another, performance of cathode filter is evaluated in a term as Quality Factor (QF), which is defined as the breakthrough time divided by its corresponding pressure drop. Using extremely small particle size in packed bed is not practical owing to its excessive pressure drop and high-level consumption of parasitic power.

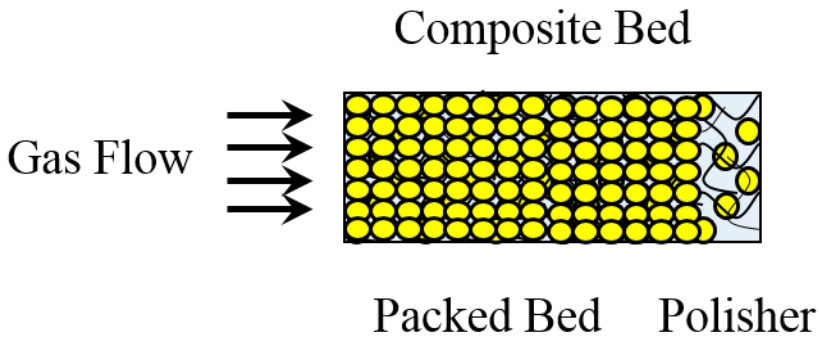

Figure VII.2 Configuration of composite bed

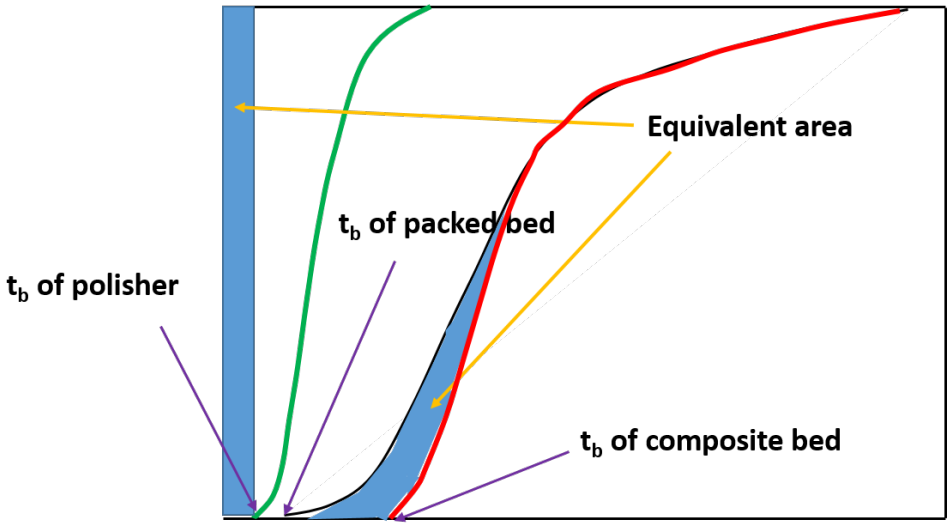

Figure VII.3 Sketch of composite bed enhancing the breakthrough time

The characteristics of composite bed can not only extend the service time of a packed bed with reduced bed volume but also mitigate parasitic power loss.

VII.2.2 Hypothesis

The composite bed is integrated by two separate adsorbent bed. The front bed, which is packed bed comprised of extrudates, acts as SO_2 reservoir. The backup polisher, which

entrapped small sorbent particulates, is of high efficiency to remove SO_2 from the gas stream from the front bed to a lower concentration to fulfill the fuel cell requirements. If the variables (e.g. operation temperature, pressure, flow rate, sulfur tolerance, air property, constraint of bed volume, etc.) are assured, there should be an optimum ratio of front bed to backup polisher.

VII.2.3 Experimental

The figure below shows breakthrough curves of a 5.5 mm thick packed bed of 40-60 mesh sorbents and a composite bed (the same packed bed followed by a 2 mm polishing layer). It can be seen that the breakthrough curve became sharper at low outlet SO_2 concentrations after incorporating the polishing layer at the end of the packed bed. The breakthrough time of composite bed was 19.8 min, which was almost 4 folds compared to packed bed (t_b=5.0 min). Whereas, the overall thickness of the composite bed was only increased by 35 %. It is also expected that for long-term protection, the composite bed should be a much better option in terms of reducing parasitic power loss.

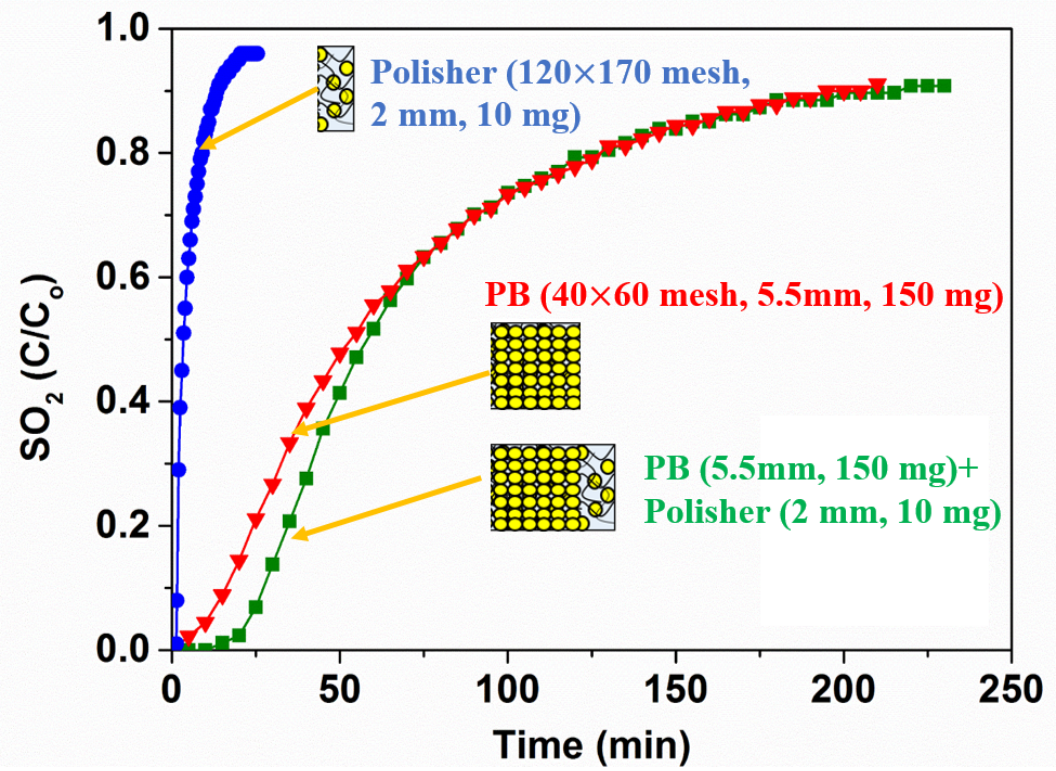

Figure VII.4 Breakthrough curves of a 5.5 mm thick packed bed of 40-60 mesh sorbents and a composite bed (the same packed bed followed by a 2 mm polishing layer of 120-170 mesh sorbents).

VII.3 UV-assisted SO_2 removal using TiO_2

VII.3.1 Background

Peterson et al.[92] reported that the quantity of terminal hydroxyl groups was highly related to the SO_2 removal performance. As shown in Figure VII.5, the capacity increased almost linearly with increasing ratio of hydroxyl groups (determined by XPS). For TiO_2, the electrons can be excited upon UV irradiation.

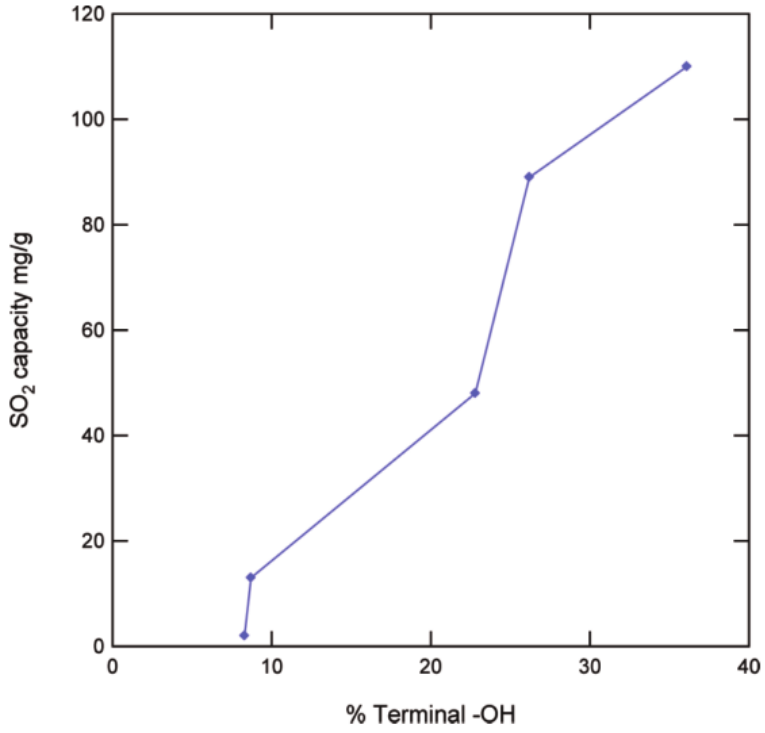

Figure VII.5 XRD SO_2 adsorption capacity as a function of terminal hydroxyl groups[92].

More importantly, surface terminal hydroxyl groups (or called isolated hydroxyl groups) can be generated after the pretreatment of UV irradiation. Baltrusaitis et al. revealed that UV/vis irradiation upon TiO_2 nanoparticles (primarily anatase) during sulfur

dioxide adsorption did lead to an enhancement in the amount of adsorbed sulfur species[83]. They proposed that the adsorbed sulfur increase was caused by the surface hydroxyl groups and molecularly adsorbed water layer.

VII.3.2 Hypothesis

The surface hydroxyl groups are potential active sites for SO_2 removal. The greater the amount of hydroxyl groups on the sorbent surface, the higher SO_2 capacity can be achieved. By introducing UV source onto TiO_2 based sorbents, the surface hydroxyl groups can be excited observably.

VII.3.3 Experimental

In order to confirm the hypothesis described above, prior to the breakthrough test, the adsorbents can be in situ heated up to 400 °C in UHP nitrogen atmosphere for 2 h. After that, the sample is cooled naturally with the nitrogen flow until reaches the desired temperature. Low heating ramp should be applied to avoid significant surface area loss during the thermal treatment. Then, the breakthrough test starts as described in Chapter II.

During the adsorbent preparation process, according to the XPS results, some other surface functional groups might be introduced, such as –C=O and –COOH, which might also interact with the SO_2 molecules during the adsorption process. Nonetheless, considering the adsorbent composition, contribution of these surface functional groups was negligible (BE=533.9 eV). By conducting this experiment, it can help us to understand the role of surface active sites in SO_2 adsorption.

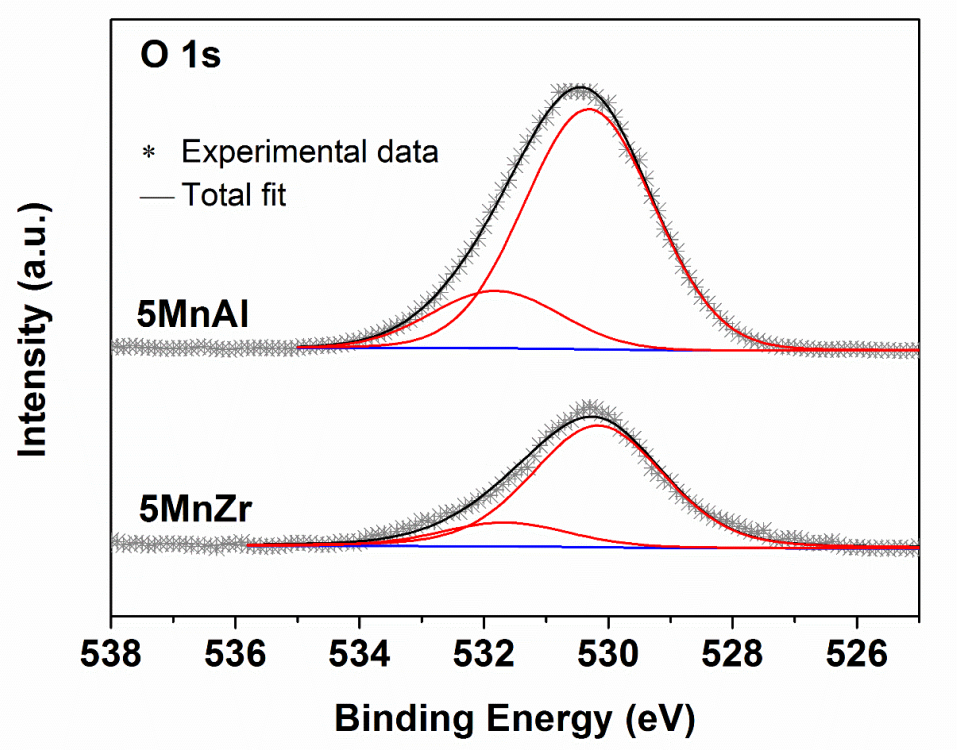

Figure VII.6 High-resolution O_{1s} XPS spectra of 5wt.% Mn supported on Al_2O_3 and ZrO_2 (Both of the sorbents were calcined at 550 °C).

FTIR is a frequently used characterization technique to study the surface hydroxyl groups. It was reported that the IR peaks centered at around 3100-3400 cm^{-1} can be ascribed to the –OH stretching vibrations of perturbed surface hydroxyls[14]. The peaks around 3500-3750 cm^{-1} may ascribe to the –OH stretching vibrations. The preliminary IR spectra of 5MnAl, 5MnSi, 5MnZr, and 5MnTi were demonstrated in Fig. VII.7. In the region between 3100-3750 cm^{-1}, there was no –OH stretching vibration for 5MnSi. However, it is difficult to quantify the amount of hydroxyl groups from FTIR.

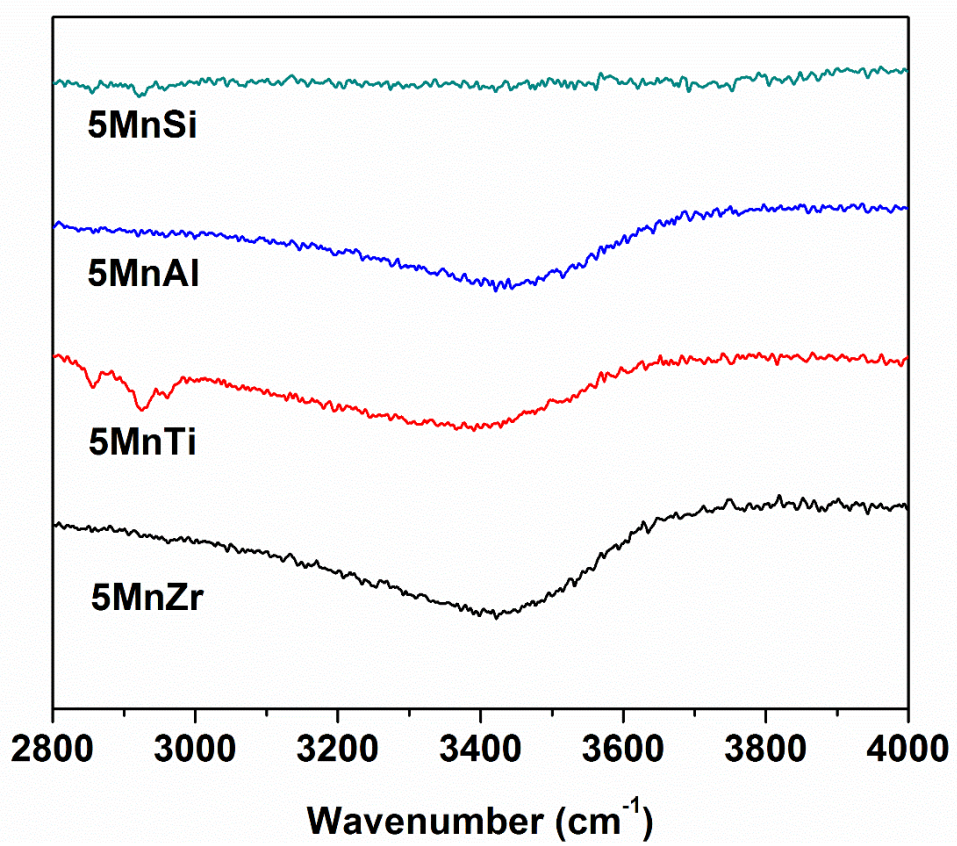

Figure VII.7 IR spectra (transmission mode) of 5 wt.% Mn doped on various supports.

Furthermore, XPS can be used to characterize the actual composition of our adsorbents. As shown in Table VII.1, the binding energy difference of lattice oxygen and surface hydroxyl groups is usually above 1.0 eV, which can be easily discerned under high-resolution XPS spectra. With the help of peak deconvolution software, different oxygen species can be identified and their relative surface concentration can be determined. Furthermore, XPS is a very effective technique in surface atoms determination.

Some preliminary data were shown in Figure VII.5 and Table VII.6. All the high resolution scans were operated with pass energy of 20 eV, dwell time of 1000 ms. Figure VII.5 illustrated the O_{1s} spectra for 5 wt.% Mn on Al_2O_3 and ZrO_2, respectively. Both of the samples were calcined at 550 °C. The peak centered at 530.2-530.3 eV is ascribed to the lattice oxygen (O_α). In addition, the peak at 531.7-531.8 eV is attributed to the terminal hydroxyl groups. The peak parameters were listed in Table VII.2. As discussed in the previous chapter, the surface hydroxyl groups and lattice oxygen are potentially important active sites for SO_2 adsorption on metal oxides[22,83,117,119–122]. Furthermore, the ratios of surface hydroxyl groups of 5MnAl and 5MnZr were 18.8 % and 15.9 %, respectively. Higher ratios implied more –OH groups existed on the surface of the adsorbents. Thus, there are more possibilities for the SO_2 molecule to interact with the surface hydroxyl groups. This XPS results are in agreement with the previous SO_2 breakthrough performance.

Table VII.1 O1s Binding Energy Assignment of Various Adsorbents.

Binding energy of assigned species (eV)		Literature cited
O_α[a]	O_β[b]	
530.6	532.1	Jonas Baltrusaitis et al.[83]
530.2	532.3	Esteban J. Romano et al.[22]
529.7	531.5	Greory W Peterson et al.[91,92]
531.0	532.4	J. van den Brand et al.[176]
529.5	531.3	Maria Roxana Morales et al.[54]
530.5	532.0	Jagdeep Singh et al.[177]
529.6	531.6	Mira Skaf et al.[178]
529.9	531.8	Sang Chai Kim et al.[65]

a. O_α denotes the lattice oxygen.

b. O_β denotes the surface hydroxyl group.

Table VII.2 The XPS results of 5wt.% Mn supported on Al_2O_3 and ZrO_2.

Sorbent	Binding Energy (eV)		FWHM (eV)		$O_\beta/(O_\alpha+O_\beta)$
	O_α[a]	O_β[b]	O_α	O_β	(%)
5MnAl	530.3	531.8	2.5	2.4	18.8
5MnZr	530.2	531.7	2.5	2.4	15.9

a. O_α denotes the lattice oxygen.

b. O_β denotes the surface hydroxyl group.

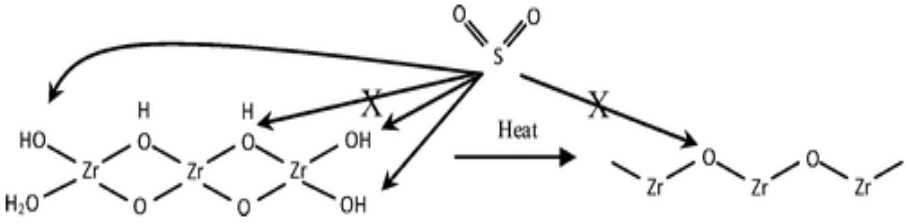

Figure VII.8 Interaction of SO_2 and zirconia polymorphs.

VII.4 Manganese Oxide sorbents for DeSO$_x$ Process under Wide Temperature Range

Since SOFC is a high temperature fuel cell, during operation, the fuel cell system might generate a great amount of heat. Moreover, high operating temperature will result in a much longer start-up time (> 30 min) than other fuel cells. During the cold start-up of SOFC system, the cathode material might experience a temperature transient from room temperature to several hundred Celsius[179]. If the structure of sorbent is not robust at high

temperature, there might be a significant surface area loss and porosity degradation, which is not beneficial for SO_2 adsorption. Therefore, the sorbent bed needs to possess a good thermal stability.

Manganese oxide can remove SO_2 very efficiently at high temperatures (e.g. T > 650 °C) based on the thermodynamic calculation. Its equilibrium concentration is in sub ppm level, which means that MnO_x is still able to remove the SO_2 in high temperature air stream. There are mainly two strategies to improve desulfurization performance: one is supported sorbents, the other is to dilute active sorbent compounds by metal oxides. For supported sorbents, the active species are supported on secondary oxides to form a structure of high surface area and high porosity. For SOFC application, the secondary oxides need also to possess excellent thermos-stability. Alumina and zirconia are the primary choice for industrial application.

REFERENCES

(1) Akhtar, N.; Decent, S. P.; Kendall, K. Cell Temperature Measurements in Micro-Tubular, Single-Chamber, Solid Oxide Fuel Cells (MT-SC-SOFCs). *J. Power Sources* **2010**, *195*, 7818–7824.

(2) Choi, S.; Yoo, S.; Kim, J.; Park, S.; Jun, A.; Sengodan, S.; Kim, J.; Shin, J.; Jeong, H. Y.; Choi, Y.; Kim, G.; Liu, M. Highly Efficient and Robust Cathode Materials for Low-Temperature Solid Oxide Fuel Cells: $PrBa_{0.5}Sr_{0.5}Co_{(2-x)}Fe_{(x)}O_{(5+\delta)}$. *Sci. Rep.* **2013**, *3*, 2426.

(3) Celik, S.; Timurkutluk, B.; Mat, M. D. Measurement of the Temperature Distribution in a Large Solid Oxide Fuel Cell Short Stack. *Int. J. Hydrogen Energy* **2013**, *38*, 10534–10541.

(4) Xiong, Y.; Yamaji, K.; Horita, T.; Yokokawa, H.; Akikusa, J.; Eto, H.; Inagaki, T. Sulfur Poisoning of SOFC Cathodes. *J. Electrochem. Soc.* **2009**, *156*, B588.

(5) Sasaki, K.; Haga, K.; Yoshizumi, T.; Minematsu, D.; Yuki, E.; Liu, R. R.; Uryu, C.; Oshima, T.; Ogura, T.; Shiratori, Y.; Ito, K.; Koyama, M.; Yokomoto, K. Chemical Durability of Solid Oxide Fuel Cells: Influence of Impurities on Long-Term Performance. *J. Power Sources* **2011**, *196*, 9130–9140.

(6) Zhu, X. B.; Wei, B.; Lu, Z.; Yang, L.; Huang, X. Q.; Zhang, Y. H.; Liu, M. L. A Direct Flame Solid Oxide Fuel Cell for Potential Combined Heat and Power Generation. *Int. J. Hydrogen Energy* **2012**, *37*, 8621–8629.

(7) Liu, M.; Lynch, M. E.; Blinn, K.; Alamgir, F. M.; Choi, Y. Rational SOFC Material Design: New Advances and Tools. *Mater. Today* **2011**, *14* (11), 534–546.

(8) Karwa, A. N.; Tatarchuk, B. J. Pressure Drop and Aerosol Filtration Efficiency of Microfibrous Entrapped Catalyst and Sorbent Media: Semi-Empirical Models. *Sep. Purif. Technol.* **2012**, *86*, 55–63.

(9) Schuler, J. A.; Yokokawa, H.; Calderone, C. F.; Jeangros, Q.; Wuillemin, Z.; Hessler-Wyser, A.; Van herle, J. Combined Cr and S Poisoning in Solid Oxide Fuel Cell Cathodes. *J. Power Sources* **2012**, *201*, 112–120.

(10) Bucher, E.; Gspan, C.; Hofer, F.; Sitte, W. Sulphur Poisoning of the SOFC Cathode Material $La_{0.6}Sr_{0.4}CoO_{3-\delta}$. *Solid State Ionics* **2013**, *238*, 15–23.

(11) Shim, J.; Jeong, D.; Jang, W.; Jeon, K.; Jeon, B. Deoxygenation of Oleic Acid over $Ce_{(1-x)}Zr_{(x)}O_2$ Catalysts in Hydrogen Environment. *Renew. Energy* **2013**, *2* (111), 1–5.

(12) Samokhvalov, A.; Tatarchuk, B. J. Review of Experimental Characterization of

Active Sites and Determination of Molecular Mechanisms of Adsorption, Desorption and Regeneration of the Deep and Ultradeep Desulfurization Sorbents for Liquid Fuels. *Catal. Rev. Eng.* **2010**, *52*, 381–410.

(13) Nair, S.; Tatarchuk, B. J. Supported Silver Adsorbents for Selective Removal of Sulfur Species from Hydrocarbon Fuels. *Fuel* **2010**, *89*, 3218–3225.

(14) Hussain, A.; Yang, H. Y.; Tatarchuk, B. J. Investigation of Organosulfur Adsorption Pathways from Liquid Fuels onto Ag/TiO_x-Al_2O_3 Adsorbents at Ambient Conditions. *Energy & Fuels* **2013**, *27*, 4353–4362.

(15) Nair, S.; Hussain, A.; Tatarchuk, B. J. The Role of Surface Acidity in Adsorption of Aromatic Sulfur Heterocycles from Fuels. *Fuel* **2013**, *105*, 695–704.

(16) Sundararaman, R.; Song, C. Catalytic Decomposition of Benzothiophenic and Dibenzothiophenic Sulfones over MgO-Based Catalysts. *Appl. Catal. B Environ.* **2013**, *148–149*, 80–90.

(17) Escandón, L. S.; Ordóñez, S.; Vega, A.; Díez, F. V. Sulphur Poisoning of Palladium Catalysts Used for Methane Combustion: Effect of the Support. *J. Hazard. Mater.* **2008**, *153*, 742–750.

(18) Wang, F.; Wang, W.; Qu, J.; Zhong, Y.; Tade, M. O.; Shao, Z. Enhanced Sulfur Tolerance of Nickel-Based Anodes for Oxygen-Ion Conducting Solid Oxide Fuel Cells by Incorporating a Secondary Water Storing Phase. *Environ. Sci. Technol.* **2014**, *48*, 12427–12434.

(19) Ferrizz, R. M.; Gorte, R. J.; Vohs, J. M. TPD and XPS Investigation of the Interaction of SO_2 with Model Ceria Catalysts. *Catal. Letters* **2002**, *82* (1–2), 123–129.

(20) Ferreira, L. S.; Trierweiler, J. O. Modeling and Simulation of the Polymeric Nanocapsule Formation Process. *IFAC Proc. Vol.* **2009**, *7* (PART 1), 405–410.

(21) Mathieu, Y.; Tzanis, L.; Soulard, M.; Patarin, J.; Vierling, M.; Molière, M. Adsorption of SO_x by Oxide Materials : A Review. **2013**, *114*, 81–100.

(22) Romano, E. J.; Schulz, K. H. A XPS Investigation of SO_2 Adsorption on Ceria-Zirconia Mixed-Metal Oxides. *Appl. Surf. Sci.* **2005**, *246* (1–3), 262–270.

(23) Kennedy, D. M.; Cahela, D. R.; Zhu, W. H.; Westrom, K. C.; Nelms, R. M.; Tatarchuk, B. J. Fuel Cell Cathode Air Filters: Methodologies for Design and Optimization. *J. Power Sources* **2007**, *168* (2), 391–399.

(24) Wang, F.; Yamaji, K.; Cho, D. H.; Shimonosono, T.; Nishi, M.; Kishimoto, H.; Brito, M. E.; Horita, T.; Yokokawa, H. Evaluation of Sulfur Dioxide Poisoning for LSCF Cathodes. *Fuel Cells* **2013**, *13* (4), 520–525.

(25) Wang, F. F.; Yamaji, K.; Cho, D. H.; Shimonosono, T.; Kishimoto, H.; Brito, M. E.; Horita, T.; Yokokawa, H. Effect of Strontium Concentration on Sulfur Poisoning of LSCF Cathodes. *Solid State Ionics* **2012**, *225*, 157–160.

(26) Kuklja, M. M.; Kotomin, E. a; Merkle, R.; Mastrikov, Y. a; Maier, J. Combined Theoretical and Experimental Analysis of Processes Determining Cathode Performance in Solid Oxide Fuel Cells. *Phys. Chem. Chem. Phys.* **2013**, *15*, 5443–5471.

(27) Córdoba, P. Status of Flue Gas Desulphurisation (FGD) Systems from Coal-Fired Power Plants : Overview of the Physic-Chemical Control Processes of Wet Limestone FGDs. **2015**, *144*, 274–286.

(28) Lowell, P. S.; Schwitzgebel, K.; Parsons, T. B. Selection of Metal Oxides for Removing SO_2 From Flue Gas. *Ind. Eng. Chem. Process Des. Dev.* **1971**, *10* (3), 384–390.

(29) Yang, H.; Lu, Y.; Tatarchuk, B. J. Glass Fiber Entrapped Sorbent for Reformates Desulfurization for Logistic PEM Fuel Cell Power Systems. *J. Power Sources* **2007**, *174* (1), 302–311.

(30) Wen, B.; He, M.; Costello, C. Simultaneous Catalytic Removal of NO_x, SO_x, and CO from FCC Regenerator. *Energy and Fuels* **2002**, *16* (5), 1048–1053.

(31) Cantú, M.; López-Salinas, E.; Valente, J. S.; Montiel, R. SO_x Removal by Calcined MgAlFe Hydrotalcite-like Materials: Effect of the Chemical Composition and the Cerium Incorporation Method. *Environ. Sci. Technol.* **2005**, *39* (24), 9715–9720.

(32) Jae, L. S.; Jun, H. K.; Jung, S. Y.; Lee, T. J.; Ryu, C. K.; Kim, J. C. Regenerable MgO-Based SO_x Removal Sorbents Promoted with Cerium and Iron Oxide in RFCC. **2005**, 9973–9978.

(33) Sumathi, S.; Bhatia, S.; Lee, K. T.; Mohamed, a. R. Cerium Impregnated Palm Shell Activated Carbon (Ce/PSAC) Sorbent for Simultaneous Removal of SO_2 and NO-Process Study. *Chem. Eng. J.* **2010**, *162* (1), 51–57.

(34) Deng, S. G.; Lin, Y. S. Synthesis, Stability, and Sulfation Properties of Sol−Gel-Derived Regenerative Sorbents for Flue Gas Desulfurization. *Ind. Eng. Chem. Res.* **1996**, *35* (4), 1429–1437.

(35) Gavaskar, V.; Abbasian, J. Dry Regenerable Metal Oxide Sorbents for SO_2 Removal from Flue Gases. 1. Development and Evaluation of Copper Oxide Sorbents. *Ind. Eng. Chem. Res.* **2006**, 5859–5869.

(36) McCrea, D. H.; Forney, a. J.; Myers, J. G. Recovery of Sulfur from Flue Gases Using a Copper Oxide Absorbent. *J. Air Pollut. Control Assoc.* **1970**, *20* (12),

819–824.

(37) Yoo, K. S.; Kim, S. D.; Park, S. Bin. Sulfation of Al_2O_3 in Flue Gas Desulfurization by CuO/g-Al_2O_3 Sorbent. *Ind. Eng. Chem. Res.* **1994**, *1* (33), 1786–1791.

(38) Jeong, S. M.; Kim, S. D. Enhancement of the SO_2 Sorption Capacity of CuO/γ-Al_2O_3 Sorbent by an Alkali-Salt Promoter. *Ind. Eng. Chem. Res.* **1997**, *36*, 5425–5431.

(39) Corma, A; Palomares, A. E.; Rey, F.; Marquez, F. Simultaneous Catalytic Removal of SO_x and NO_x with Hydrotalcite-Derived Mixed Oxides Containing Copper, and Their Possibilities to Be Used in FCC Units. *J. Catal.* **1997**, *170* (1), 140–149.

(40) Cheng, W. P.; Yu, X. Y.; Wang, W. J.; Liu, L.; Yang, J. G.; He, M. Y. Synthesis, Characterization and Evaluation of Cu/MgAlFe as Novel Transfer Catalyst for SO_x Removal. *Catal. Commun.* **2008**, *9* (6), 1505–1509.

(41) Kim, K. H.; Chol, J. S. Kinetics and Mechanism of the Oxidation of Sulfur Dioxide on α-Fe_2O_3. *J. Phys. Chem.* **1981**, *85*, 2447–2450.

(42) Ma, J. R.; Liu, Z. Y.; Liu, S. J.; Zhu, Z. P. A Regenerable Fe/AC Desulfurizer for SO_2 Adsorption at Low Temperatures. *Appl. Catal. B-Environmental* **2003**, *45*, 301–309.

(43) Davini, P. Influence of Surface Properties and Iron Addition on the SO_2 Adsorption Capacity of Activated Carbons. **2002**, *40*, 729–734.

(44) Sanchez-cantu, M.; Perez-diaz, L. M.; Maubert, A. M.; Valente, J. S. Dependence of Chemical Composition of Calcined Hydrotalcite-like Compounds for SO_x Reduction. *Catal. Today* **2010**, *150* (3–4), 332–339.

(45) Kang, H. T.; Lv, K.; Yuan, S. L. Applied Clay Science Synthesis , Characterization , and SO_2 Removal Capacity of MnMgAlFe Mixed Oxides Derived from Hydrotalcite-like Compounds. *Appl. Clay Sci.* **2013**, *72*, 184–190.

(46) Arcibar-orozco, J. A.; Rangel-mendez, J. R.; Bandosz, T. J. Reactive Adsorption of SO_2 on Activated Carbons with Deposited Iron Nanoparticles. *J. Hazard. Mater.* **2013**, *246–247*, 300–309.

(47) Koballa, Thomas E.; Dudukovic, M. P. Sulfur Dioxide Adsorption on Metal Oxides Supported on Alumina. *AIChE Symp. Ser.* **1978**, *73*, 199–228.

(48) Liu, Y; Qu, Y.; Guo, J.; Wang, X.; Chu, Y.; Yin, H.; Li, J. Thermal Regeneration of Manganese Supported on Activated Carbons Treated by HNO_3 for Desulfurization. *Energy & Fuels* **2015**, *29* (3), 1931–1940.

(49) Qu, Y.; Guo, J.; Chu, Y.; Sun, M.; Yin, H.. The Influence of Mn Species on the SO_2 Removal of Mn-Based Activated Carbon Catalysts. *Appl. Surf. Sci.* **2013**, *282*, 425–431.

(50) Guo, J.; Qu, Y.; Shu, S.; Wang, X.; Yin, H. Effects of Preparation Conditions on Mn-Based Activated Carbon Catalysts for Desulfurization. *New J. Chem.* **2015**, No. x.

(51) Wang, J.; Zhao, F.; Hu, Y.; Zhao, R.; Liu, R. Modification of Activated Carbon Fiber by Loading Metals and Their Performance on SO_2 Removal. *Chinese J. Chem. Eng.* **2006**, *14* (4), 478–485.

(52) Lamaita, L.; Peluso, M. A.; Sambeth, J. E.; Thomas, H. J. Synthesis and Characterization of Manganese Oxides Employed in VOCs Abatement. **2005**, *61*, 114–119.

(53) Piumetti, M.; Fino, D.; Russo, N. Mesoporous Manganese Oxides Prepared by Solution Combustion Synthesis as Catalysts for the Total Oxidation of VOCs. *Appl. Catal. B Environ.* **2015**, *163*, 277–287.

(54) Morales, M. R.; Barbero, B. P.; Cadús, L. E. Evaluation and Characterization of Mn-Cu Mixed Oxide Catalysts for Ethanol Total Oxidation: Influence of Copper Content. *Fuel* **2008**, *87* (7), 1177–1186.

(55) Trawczyński, J.; Bielak, B.; Miśta, W. Oxidation of Ethanol over Supported Manganese Catalysts - Effect of the Carrier. *Appl. Catal. B Environ.* **2005**, *55* (4), 277–285.

(56) Tikhomirov, K.; Kröcher, O.; Elsener, M.; Widmer, M.; Wokaun, A. Manganese Based Materials for Diesel Exhaust SO_2 Traps. *Appl. Catal. B Environ.* **2006**, *67* (3–4), 160–167.

(57) Pereira, H. B.; Polato, C. M. S.; Monteiro, J. L. F.; Henriques, C. a. Mn/Mg/Al-Spinels as Catalysts for SOx Abatement Influence of CeO_2 Incorporation and Catalytic Stability. *Catal. Today* **2010**, *149* (3–4), 309–315.

(58) Njagi, E. C.; Chen, C.; Genuino, H.; Galindo, H.; Huang, H.; Suib, S. L. Applied Catalysis B : Environmental Total Oxidation of CO at Ambient Temperature Using Copper Manganese Oxide Catalysts Prepared by a Redox Method. *"Applied Catal. B, Environ.* **2010**, *99* (1–2), 103–110.

(59) Carnö, J.; Ferrandon, M.; Björnbom, E.; Järås, S. Mixed Manganese Oxide/platinum Catalysts for Total Oxidation of Model Gas from Wood Boilers. *Appl. Catal. A Gen.* **1997**, *155* (2), 265–281.

(60) Strohmeier, B. R.; Hercules, D. M. Surface Spectroscopic Characterization of Manganese/aluminum Oxide Catalysts. *J. Phys. Chem.* **1984**, *88* (21), 4922–4929.

(61) Yang, Z.; Zhang, Y.; Zhang, W.; Wang, X.; Qian, Y.; Wen, X.; Yang, S. Nanorods of Manganese Oxides: Synthesis, Characterization and Catalytic Application. *J. Solid State Chem.* **2006**, *179* (3), 679–684.

(62) Ettireddy, P. R.; Ettireddy, N.; Mamedov, S.; Boolchand, P.; Smirniotis, P. G. Surface Characterization Studies of TiO_2 Supported Manganese Oxide Catalysts for Low Temperature SCR of NO with NH_3. *Appl. Catal. B-Environmental* **2007**, *76*, 123–134.

(63) Bounechada, D.; Darmastuti, Z.; Andersson, M.; Ojamäe, L.; Lloyd Spetz, A.; Skoglundh, M.; Carlsson, P.-A. Vibrational Study of SO_x Adsorption on Pt/SiO_2. *J. Phys. Chem. C* **2014**, *118*, 29713–29723.

(64) Qu, Z.; Bu, Y.; Qin, Y.; Wang, Y.; Fu, Q. The Improved Reactivity of Manganese Catalysts by Ag in Catalytic Oxidation of Toluene. *Appl. Catal. B Environ.* **2013**, *132–133*, 353–362.

(65) Kim, S. C.; Shim, W. G. Catalytic Combustion of VOCs over a Series of Manganese Oxide Catalysts. *Appl. Catal. B Environ.* **2010**, *98* (3–4), 180–185.

(66) Craciun, R.; Nentwick, B.; Hadjiivanov, K.; Knözinger, H. Structure and Redox Properties of MnOx/Yttrium-Stabilized Zirconia (YSZ) Catalyst and Its Used in CO and CH_4 Oxidation. *Appl. Catal. A Gen.* **2003**, *243* (1), 67–79.

(67) Zhao, L.; Li, X. Y.; Zhao, J. Correlation of Structural and Chemical Characteristics with Catalytic Performance of Hydrotalcite-Based CuNiAl Mixed Oxides for SO_2 Abatement. *Chem. Eng. J.* **2013**, *223*, 164–171.

(68) Guo, J. X.; Liang, J.; Chu, Y. H.; Sun, M. C.; Yin, H. Q.; Li, J. J. Desulfurization Activity of Nickel Supported on Acid-Treated Activated Carbons. *Appl. Catal. A Gen.* **2012**, *421–422*, 142–147.

(69) Zhao, L.; Li, X.; Qu, Z.; Zhao, Q.; Liu, S.; Hu, X. The NiAl Mixed Oxides: The Relation between Basicity and SO_2 Removal Capacity. *Sep. Purif. Technol.* **2011**, *80* (2), 345–350.

(70) Xiao, Y.; Liu, Q. Y.; Liu, Z. Y.; Huang, Z. G.; Guo, Y. X.; Yang, J. L. Roles of Lattice Oxygen in V_2O_5 and Activated Coke in SO_2 Removal over Coke-Supported V_2O_5 Catalysts. *Appl. Catal. B-Environmental* **2008**, *82*, 114–119.

(71) Ma, J.; Liu, Z.; Liu, Q.; Guo, S.; Huang, Z.; Xiao, Y. SO_2 and NO Removal from Flue Gas over V_2O_5/AC at Lower Temperatures - Role of V_2O_5 on SO_2 Removal. *Fuel Process. Technol.* **2008**, *89* (3), 242–248.

(72) Dunn, J. P.; Koppula, P. R.; G. Stenger, H.; Wachs, I. E. Oxidation of Sulfur Dioxide to Sulfur Trioxide over Supported Vanadia Catalysts. *Appl. Catal. B Environ.* **1998**, *19* (2), 103–117.

(73) Macken, C.; Hodnett, B. K.; Paparatto, G. Testing of the CuO/Al_2O_3 Catalyst−Sorbent in Extended Operation for the Simultaneous Removal of NO_x and SO_2 from Flue Gases. *Ind. Eng. Chem. Res.* **2000**, *39* (10), 3868–3874.

(74) Jeong, S. M.; Kim, S. D. Removal of NO_x and SO_2 by $CuO/\gamma\text{-}Al_2O_3$ Sorbent/Catalyst in a Fluidized-Bed Reactor. *Ind. Eng. Chem. Res.* **2000**, *39*, 1911–1916.

(75) Qingxin, M.; Liu, Y.; He, H. Synergistic Effect between NO_2 and SO_2 in Their Adsorption and Reaction on Alumina. *J. Phys. Chem. A* **2008**, *112* (29), 6630–6635.

(76) Wu, Q.; Gao, H.; He, H. Conformational Analysis of Sulfate Species on Ag/Al_2O_3 Using Theoretical and Experimental Vibration Spectra. *J. Phys. Chem. B* **2006**, 8320–8324.

(77) Schreier, E.; Eckelt, R.; Richter, M.; Fricke, R. Sulphur Trap Materials Based on Mesoporous Al_2O_3. *Appl. Catal. B-Environmental* **2006**, *65*, 249–260.

(78) Xue, E.; Seshan, K.; Ross, J. R. H. Roles of Supports, Pt Loading and Pt Dispersion in the Oxidation of NO to NO_2 and of SO_2 to SO_3. *Appl. Catal. B-Environmental* **1996**, *11*, 65–79.

(79) Hamzehlouyan, T.; Sampara, C.; Li, J.; Kumar, A.; Epling, W. Experimental and Kinetic Study of SO_2 Oxidation on a $Pt/\gamma\text{-}Al_2O_3$ Catalyst. *Appl. Catal. B Environ.* **2014**, *152–153*, 108–116.

(80) Rodriguez, J. a.; Liu, G.; Jirsak, T.; Hrbek, J.; Chang, Z.; Dvorak, J.; Maiti, A. Activation of Gold on Titania: Adsorption and Reaction of SO_2 on $Au/TiO_2(110)$. *J. Am. Chem. Soc.* **2002**, *124* (18), 5242–5250.

(81) Hussain, a. H. M. S.; McKee, M. L.; Heinzel, J. M.; Sun, X.; Tatarchuk, B. J. Density Functional Theory Study of Organosulfur Selective Adsorption on Ag–TiO_2 Adsorbents. *J. Phys. Chem. C* **2014**, *118* (27), 14938–14947.

(82) Ao, C. H.; Lee, S. C.; Zou, S. C.; Mak, C. L. Inhibition Effect of SO_2 on NO_x and VOCs during the Photodegradation of Synchronous Indoor Air Pollutants at Parts per Billion (ppb) Level by TiO_2. *Appl. Catal. B Environ.* **2004**, *49* (3), 187–193.

(83) Baltrusaitis, J.; Jayaweera, P. M.; Grassian, V. H. Sulfur Dioxide Adsorption on TiO_2 Nanoparticles: Influence of Particle Size, Coadsorbates, Sample Pretreatment, and Light on Surface Speciation and Surface Coverage. *J. Phys. Chem. C* **2011**, *115* (2), 492–500.

(84) Centi, G.; Perathoner, S. Performances of SO_x Traps Derived from Cu/Al Hydrotalcite for the Protection of NO_x Traps from the Deactivation by Sulphur. *Appl. Catal. B Environ.* **2007**, *70* (1–4), 172–178.

(85) Centi, G.; Perathoner, S. Behaviour of SOx-Traps Derived from Ternary Cu/Mg/Al Hydrotalcite Materials. *Catal. Today* **2007**, *127* (1–4), 219–229.

(86) Maria, C.; Polato, S.; Assumpc, C.; Carlos, A.; Rodrigues, C. De-SO_x Additives Based on Mixed Oxides Derived from Mg, Al-Hydrotalcite-like Compounds Containing Fe, C , Co or Cr. *Catal. Today* **2008**, *135*, 534–540.

(87) Zhao, L.; Li, X.; Hao, C.; Raston, C. L. SO_2 Adsorption and Transformation on Calcined NiAl Hydrotalcite-like Compounds Surfaces: An in Situ FTIR and DFT Study. *Appl. Catal. B Environ.* **2012**, *117–118*, 339–345.

(88) Zhao, L.; Li, X.; Zhao, J. Correlation of Structural and Chemical Characteristics with Catalytic Performance of Hydrotalcite-Based CuNiAl Mixed Oxides for SO_2 Abatement. *Chem. Eng. J.* **2013**, *223*, 164–171.

(89) Li, L.; King, D. L. Applied Catalysis B : Environmental Fast-Regenerable Sulfur Dioxide Absorbents for Lean-Burn Diesel Engine Emission Control. *"Applied Catal. B, Environ.* **2010**, *100* (1–2), 238–244.

(90) Tailor, R.; Ahmadalinezhad, A.; Sayari, A. Selective Removal of SO_2 over Tertiary Amine-Containing Materials. *Chem. Eng. J.* **2014**, *240*, 462–468.

(91) Peterson, G. W.; Karwacki, C. J.; Feaver, W. B.; Rossin, J. A. Zirconium Hydroxide as a Reactive Substrate for the Removal of Sulfur Dioxide. *Ind. Eng. Chem. Res.* **2009**, *48* (4), 1694–1698.

(92) Peterson, G. W.; Rossin, J. a.; Karwacki, C. J.; Glover, T. G. Surface Chemistry and Morphology of Zirconia Polymorphs and the Influence on Sulfur Dioxide Removal. *J. Phys. Chem. C* **2011**, *115* (19), 9644–9650.

(93) Gaudin, P.; Dorge, S.; Nouali, H.; Kehrli, D.; Michelin, L.; Josien, L.; Fioux, P.; Vidal, L.; Soulard, M.; Vierling, M.; Molière, M.; Patarin, J. Synthesis of Cu-Ce/ KIT-6 Materials for SO_x Removal. *Appl. Catal. A Gen.* **2014**, *(In Press)*.

(94) Guo, J.; Lua, A. C. Textural and Chemical Characterisations of Activated Carbon Prepared from Oil-Palm Stone with H_2SO_4 and KOH Impregnation. *Microporous Mesoporous Mater.* **1999**, *32* (1–2), 111–117.

(95) Aarna, I.; Suuberg, E. M. Role of Carbon Monoxide in the NO-Carbon Reaction. *Energy and Fuels* **1999**, *13* (6), 1145–1153.

(96) Jeong-Ho Yun, D.-K. C. S.-H. K. Equilibria and Dynamics for Mixed Vapors of BTX in an Activated Carbon Bed. *AIChE J.* **1999**, *45* (4), 751–760.

(97) Lee, Y.; Park, J. Adsorption Characteristics of SO_2 on Activated Carbon Prepared from Coconut Shell with Potassium Hydroxide Activation. *Environ. Sci. Technol.* **2002**, *36*, 1086–1092.

(98) Bagreev, A.; Bashkova, S.; Bandosz, T. J. Adsorption of SO_2 on Activated Carbons: The Effect of Nitrogen Functionality and Pore Sizes. *Langmuir* **2002**, *18* (4), 1257–1264.

(99) Tsuji, K.; Shiraishi, I. Combined Desulfurization, Denitrification and Reduction of Air Toxics Using Activated Coke: 2. Process Applications and Performance of Activated Coke. *Fuel* **1997**, *76* (6), 555–560.

(100) Fu, H.; Wang, X.; Wu, H.; Yin, Y.; Chen, J. Heterogeneous Uptake and Oxidation of SO_2 on Iron Oxides. *J. Phys. Chem. C.* **2007**, *111*, 6077–6085.

(101) Mangun, C. L.; Debarr, J. A.; Economy, J. Adsorption of Sulfur Dioxide on Ammonia-Treated Activated Carbon Fibers. *Carbon N. Y.* **2001**, *39*, 1689–1696.

(102) Doornkamp, C.; Ponec, V. The Universal Character of the Mars and Van Krevelen Mechanism. *J. Mol. Catal. A Chem.* **2000**, *162* (1–2), 19–32.

(103) Gutiérrez-Ortiz, J.I.; López-Fonseca, R; Aurrekoetxea, U. and González-Velasco, J. R. Low-Temperature Deep Oxidation of Dichloromethane and Trichloroethylene by H-ZSM-5-Supported Manganese Oxide Catalysts. *J. Catal.* **2003**, *218* (1), 148–154.

(104) Thirupathi, B.; Smirniotis, P. G. Nickel-Doped Mn/TiO_2 as an Efficient Catalyst for the Low-Temperature SCR of NO with NH_3: Catalytic Evaluation and Characterizations. *J. Catal.* **2012**, *288*, 74–83.

(105) Li, L. Y.; King, D. L. Fast-Regenerable Sulfur Dioxide Absorbents for Lean-Burn Diesel Engine Emission Control. *Appl. Catal. B-Environmental* **2010**, *100*, 238–244.

(106) Li, H.; Lu, G.; Dai, Q.; Wang, Y.; Guo, Y.; Guo, Y. Efficient Low-Temperature Catalytic Combustion of Trichloroethylene over Flower-like Mesoporous Mn-Doped CeO_2 Microspheres. *Appl. Catal. B Environ.* **2011**, *102* (3–4), 475–483.

(107) Sentorun-Shalaby, C.; Saha, S. K.; Ma, X. L.; Song, C. S. Mesoporous-Molecular-Sieve-Supported Nickel Sorbents for Adsorptive Desulfurization of Commercial Ultra-Low-Sulfur Diesel Fuel. *Appl. Catal. B-Environmental* **2011**, *101*, 718–726.

(108) Ettireddy, P. R.; Ettireddy, N.; Mamedov, S.; Boolchand, P.; Smirniotis, P. G. Surface Characterization Studies of TiO_2 Supported Manganese Oxide Catalysts for Low Temperature SCR of NO with NH_3. *Appl. Catal. B Environ.* **2007**, *76* (1–2), 123–134.

(109) Tang, X.; Li, J.; Sun, L.; Hao, J. Origination of N_2O from NO Reduction by NH_3 over β-MnO_2 and α-Mn_2O_3. *Appl. Catal. B Environ.* **2010**, *99* (1–2), 156–162.

(110) Xing, S. T.; Hu, C.; Qu, J. H.; He, H.; Yang, M. Characterization and Reactivity of

MnO_x Supported on Mesoporous Zirconia for Herbicide 2,4-D Mineralization with Ozone. *Environ. Sci. Technol.* **2008**, *42*, 3363–3368.

(111) Liang, S. H.; Bulgan, F. T. G.; Zong, R. L.; Zhu, Y. F. Effect of Phase Structure of MnO_2 Nanorod Catalyst on the Activity for CO Oxidation. *J. Phys. Chem. C* **2008**, *112*, 5307–5315.

(112) Kapteijn, F; Langeveld, Dick van; Moulijn Jacob A.; Andreini, Amedeo; Vuurman, Michael A.; Turek, Andrzej M; Jehng, Jih-Mirn; Wachs, I. E. Alumina-Supported Manganese Oxide Catalysts. *J. Catal.* **1994**.

(113) Zhu, Y. F.; Zhu, Y. L.; Ding, G. Q.; Zhu, S. H.; Zheng, H. Y.; Li, Y. W. Highly Selective Synthesis of Ethylene Glycol and Ethanol via Hydrogenation of Dimethyl Oxalate on Cu Catalysts: Influence of Support. *Appl. Catal. A Gen.* **2013**, *468*, 296–304.

(114) Zhang, Y.; Qin, Z.; Wang, G.; Zhu, H.; Dong, M.; Li, S.; Wu, Z.; Li, Z.; Wu, Z.; Zhang, J.; Hu, T.; Fan, W.; Wang, J. Catalytic Performance of MnO_x-NiO Composite Oxide in Lean Methane Combustion at Low Temperature. *Appl. Catal. B-Environmental* **2013**, *129*, 172–181.

(115) Zuo, J.; Chen, Z.; Wang, F.; Yu, Y.; Wang, L.; Li, X. Low-Temperature Selective Catalytic Reduction of NO_x with NH_3 over Novel Mn-Zr Mixed Oxide Catalysts. *Ind. Eng. Chem. Res.* **2014**, *53*, 2647–2655.

(116) Waqif, M.; Bazin, P.; Saur, O.; Lavalley, J. C.; Blanchard, G.; Touret, O. Study of Ceria Sulfation. *Appl. Catal. B Environ.* **1997**, *11* (2), 193–205.

(117) Usher, C. R. A Laboratory Study of the Heterogeneous Uptake and Oxidation of Sulfur Dioxide on Mineral Dust Particles. *J. Geophys. Res.* **2002**, *107* (D23).

(118) Wachs, I. E. Raman and IR Studies of Surface Metal Oxide Species on Oxide Supports: Supported Metal Oxide Catalysts. *Catal. Today* **1996**, *27* (3–4), 437–455.

(119) Nanayakkara, C. E.; Pettibone, J.; Grassian, V. H. Sulfur Dioxide Adsorption and Photooxidation on Isotopically-Labeled Titanium Dioxide Nanoparticle Surfaces: Roles of Surface Hydroxyl Groups and Adsorbed Water in the Formation and Stability of Adsorbed Sulfite and Sulfate. *Phys. Chem. Chem. Phys.* **2012**, *14* (19), 6957.

(120) Goodman, a. L.; Li, P.; Usher, C. R.; Grassian, V. H. Heterogeneous Uptake of Sulfur Dioxide on Aluminum and Magnesium Oxide Particles. *J. Phys. Chem. A* **2001**, *105* (25), 6109–6120.

(121) Gao, Y.; Chen, D. Heterogeneous Reactions of Sulfur Dioxide on Dust. *Sci. China, Ser. B Chem.* **2006**, *49* (3), 273–280.

(122) Cen, W.; Hou, M.; Liu, J.; Yuan, S.; Liu, Y.; Chu, Y. Oxidation of SO_2 and NO by Epoxy Groups on Graphene Oxides: The Role of the Hydroxyl Group. *RSC Adv.* **2015**, *5* (29), 22802–22810.

(123) Chen, H.; Nanayakkara, C. E.; Grassian, V. H. Titanium Dioxide Photocatalysis in Atmospheric Chemistry. *Chem. Rev.* **2012**, *112* (11), 5919–5948.

(124) Zhang, Y.; Qin, Z.; Wang, G.; Zhu, H.; Dong, M.; Li, S.; Wu, Z.; Li, Z.; Wu, Z.; Zhang, J.; Hu, T.; Fan, W.; Wang, J. Catalytic Performance of MnO_x-NiO Composite Oxide in Lean Methane Combustion at Low Temperature. *Appl. Catal. B Environ.* **2013**, *129*, 172–181.

(125) Lou, X.; Liu, P.; Li, J.; Li, Z.; He, K. Effects of Calcination Temperature on Mn Species and Catalytic Activities of Mn/ZSM-5 Catalyst for Selective Catalytic Reduction of NO with Ammonia. *Appl. Surf. Sci.* **2014**, *307*, 382–387.

(126) Pourkhalil, M.; Moghaddam, A. Z.; Rashidi, A.; Towfighi, J.; Mortazavi, Y. Preparation of Highly Active Manganese Oxides Supported on Functionalized MWNTs for Low Temperature NO_x Reduction with NH_3. *Appl. Surf. Sci.* **2013**, *279*, 250–259.

(127) Song, C. Fuel Processing for Low-Temperature and High-Temperature Fuel Cells: Challenges, and Opportunities for Sustainable Development in the 21st Century. *Catal. Today* **2002**, *77* (1–2), 17–49.

(128) Wang, Z.; Peng, Y.; Ren, X.; Gui, S.; Zhang, G. Absorption of Sulfur Dioxide with Sodium Hydroxide Solution in Spray Columns. *Ind. Eng. Chem. Res.* **2015**, *54* (35), 8670–8677.

(129) Garea, A.; Herrera, J. L.; Marques, J. A.; Irabien, A. Kinetics of Dry Flue Gas Desulfurization at Low Temperaturesusing $Ca(OH)_2$: Competitive Reactions of Sulfation and Carbonation. *Chem. Eng. Sci.* **2001**, *56* (4), 1387–1393.

(130) Karatepe, N.; Erdoğan, N.; Ersoy-Meriçboyu, A.; Küçü, S. Preparation of diatomite/$Ca(OH)_2$ Sorbents and Modelling Their Sulphation Reaction. *Chem. Eng. Sci.* **2004**, *59* (18), 3883–3889.

(131) Bahrami, R.; Ale Ebrahim, H.; Halladj, R.; Ale Ebrahim, M. A. Applying the Random Pore Model in a Packed Bed Reactor for the Regenerative SO_2 Removal Reaction by CuO. *Ind. Eng. Chem. Res.* **2014**, *53* (42), 16285–16292.

(132) Li, Y.; Qi, H.; You, C.; Xu, X. Kinetic Model of CaO/fly Ash Sorbent for Flue Gas Desulphurization at Moderate Temperatures. *Fuel* **2007**, *86* (5–6), 785–792.

(133) Shih, S. M.; Lai, J. C.; Yang, C. H. Kinetics of the Reaction of Dense CaO Particles with SO_2. *Ind. Eng. Chem. Res.* **2011**, *50* (22), 12409–12420.

(134) Vogel, R. F.; Mitchell, B. R.; Massoth, F. E. Reactivity of SO_2 with Supported Metal Oxide-Alumina Sorbents. *Environ. Sci. Technol.* **1974**, *8*, 432–436.

(135) Centi, Gabriele; Passarini, Nello; Perathoner, Siglinda; Riva, A. Combined $DeSO_x/DeNO_x$ Reactions on a Copper on Alumina Sorbent-Catalyst. 1. Mechanism of SO_2 Oxidation-Adsorption. *Ind. Eng. Chem. Res.* **1992**, *31*, 1947–1955.

(136) Centi, G.; Passarini, N.; Perathoner, S.; Riva, A. Combined $DeSO_x/DeNO_x$ Reactions on a Copper on Alumina Sorbent-Catalyst. 2. Kinetics of the $DeSO_x$ Reaction. *Ind. Eng. Chem. Res.* **1992**, *31*, 1956–1963.

(137) Yoo, Kyung Seun; Kim, Sang Done; Park, S. B. Sulfation of Al_2O_3 in Flue Gas Desulfurization by CuO/Al_2O_3 Sorbent. *Ind. Eng. Chem. Res.* **1994**, *33*, 1786–1791.

(138) Tikhomirov, K.; Krocher, O.; Elsener, M.; Widmer, M.; Wokaun, A. Manganese Based Materials for Diesel Exhaust SO_2 Traps. *Appl. Catal. B-Environmental* **2006**, *67*, 160–167.

(139) Kiang, K.; Li, K.; Rothfus, R. Kinetic Studies of Sulfur Dioxide Absorption by Manganese Dioxide. *Environ. Sci. Technol.* **1976**, *10*, 886–892.

(140) Uysal, B. Z.; Aksahin, I.; Yucel, H. Sorption of SO_2 on Metal Oxides in a Fluidized Bed. *Ind. Eng. Chem. Res.* **1988**, *27*, 434–439.

(141) Centi, G.; Perathoner, S. Role of the Size and Texture Properties of Copper-on-Alumina Pellets During the Simultaneous Removal of SO_2 and NO_x From Flue Gas. *Ind. Eng. Chem. Res.* **1997**, *36* (8), 2945–2953.

(142) Dos Santos, R. P.; Da Silva, T. C.; Gonçalves, M. L. A.; Louis, B.; Pereira, E. B.; Herbst, M. H.; Pereira, M. M. Investigation of the Nature of V-Species on Alumina Modified by Alkali Cations: Development of Multi-Functional $DeSO_x$ Catalysts. *Appl. Catal. A Gen.* **2012**, *449*, 23–30.

(143) Przepiórski, J.; Czyzewski, a.; Kapica, J.; Moszynski, D.; Grzmil, B.; Tryba, B.; Mozia, S.; Morawski, a. W. Low Temperature Removal of SO_2 Traces from Air by MgO-Loaded Porous Carbons. *Chem. Eng. J.* **2012**, *191*, 147–153.

(144) Tatarchuk, B.; Chang, B. K.; Lu, Y.; Chen, Laiyuan; Luna, Eric; Cahela, D. Microfibrous Entrapment of Small Reactive Particulates and Fibers for High Contacting Efficiency Removal of Contaminants from Gaseous or Liquid Streams. US 7501012B2, 2009.

(145) Kalluri, R. R.; Cahela, D. R.; Tatarchuk, B. J. Microfibrous Entrapped Small Particle Adsorbents for High Efficiency Heterogeneous Contacting. *Sep. Purif. Technol.* **2008**, *62* (2), 304–316.

(146) Sheng, M.; Yang, H. Y.; Cahela, D. R.; Tatarchuk, B. J. Novel Catalyst Structures with Enhanced Heat Transfer Characteristics. *J. Catal.* **2011**, *281*, 254–262.

(147) Kalluri, R. R.; Cahela, D. R.; Tatarchuk, B. J. Comparative Heterogeneous Contacting Efficiency in Fixed Bed Reactors: Opportunities for New Microstructured Systems. *Appl. Catal. B-Environmental* **2009**, *90* (3–4), 507–515.

(148) Yang, H.; Cahela, D. R.; Tatarchuk, B. J. A Study of Kinetic Effects due to Using Microfibrous Entrapped Zinc Oxide Sorbents for Hydrogen Sulfide Removal. *Chem. Eng. Sci.* **2008**, *63* (10), 2707–2716.

(149) Suyadal, Y.; Oguz, H. Dry Desulfurization of Simulated Flue Gas in a Fluidized-Bed Reactor for a Broad Range of SO_2 Concentration and Temperature: A Comparison of Models. *Ind. Eng. Chem. Res.* **1999**, *38* (8), 2932–2939.

(150) Dam-Johansen, K.;Hansen, P.F.B.; Østergaard, K. High-Temperature Reaction between Sulfur Dioxide and Limestone—III. A Grain-Micrograin Model and its Verification. *Chem. Eng. Sci.* **1991**, *46* (3), 847–853.

(151) Gasvaskar, V. S.; Abbasian, J. Dry Regenerable Metal Oxide Sorbents for SO_2 Removal from Flue Gases. 2. Modeling of the Sulfation Reaction Involving Copper Oxide Sorbents. *Ind. Eng. Chem. Res.* **2007**, *46*, 1161–1166.

(152) Alvarez, E.; González, J. F. High Pressure Thermogravimetric Analysis of the Direct Sulfation of Spanish Calcium-Based Sorbents. *Fuel* **1999**, *78* (3), 341–348.

(153) Bausach, M.; Pera-Titus, M.; Fité, C.; Cunill, F.; Izquierdo, J. F.; Tejero, J.; Iborra, M. Kinetic Modeling of the Reaction between Hydrated Lime and SO_2 at Low Temperature. *AIChE J.* **2005**, *51* (5), 1455–1466.

(154) Kopac, Turkan; Kocabas, S. Sulfur Dioxide Adsorption Isotherms and Breakthrough Analysis on Molecular Sieve 5A Zeolite. *Chem. Eng. Comm.* **2003**, *190* (May 2001), 1041–1054.

(155) Dahlan, I.; Lee, K. T.; Kamaruddin, A. H.; Mohamed, A. R. Sorption of SO_2 and NO from Simulated Flue Gas over Rice Husk Ash (RHA)/CaO/CeO_2 Sorbent: Evaluation of Deactivation Kinetic Parameters. *J. Hazard. Mater.* **2011**, *185* (2–3), 1609–1613.

(156) Yasyerli, S.; Dogu, G.; Ar, I. Activities of Copper Oxide and Cu–V and Cu–Mo Mixed Oxides for H_2S Removal in the Presence and Absence of Hydrogen and Predictions of a Deactivation Model. *Ind. Eng. Chem. Res.* **2001**, *40*, 5206–5214.

(157) Li, L.; Wen, X.; Fu, X.; Wang, F.; Zhao, N.; Xiao, F.; Wei, W.; Sun, Y. MgO/Al_2O_3 Sorbent for CO_2 Capture. *Energy and Fuels* **2010**, *24* (10), 5773–5780.

(158) Suyadal, Y.; Erol, M.; Oğuz, H. Deactivation Model for Dry Desulphurization of Simulated Flue Gas with Calcined Limestone in a Fluidized-Bed Reactor. *Fuel* **2005**, *84* (12–13), 1705–1712.

(159) Ferna, I.; Garea, A.; Irabien, A. SO_2 Reaction with $Ca(OH)_2$ at Medium (300-425°C): Kinetic Behaviour. *Chem. Eng. Sci.* **1998**, *53* (10), 1869–1881.

(160) Lee, K. T.; Koon, O. W. Modified Shrinking Unreacted-Core Model for the Reaction between Sulfur Dioxide and Coal Fly ash/CaO/$CaSO_4$ Sorbent. *Chem. Eng. J.* **2009**, *146* (1), 57–62.

(161) Levenspiel, O. *Chemical Reaction Engineering*, 1st ed.; Wiley: New York, 1962.

(162) Yaşyerli, S.; Ar, İ.; Doğu, G.; Doğu, T. Removal of Hydrogen Sulfide by Clinoptilolite in a Fixed Bed Adsorber. *Chem. Eng. Process. Process Intensif.* **2002**, *41* (9), 785–792.

(163) Garces, H. F.; Galindo, H. M.; Garces, L. J.; Hunt, J.; Morey, A.; Suib, S. L. Low Temperature H_2S Dry-Desulfurization with Zinc Oxide. *Microporous Mesoporous Mater.* **2010**, *127* (3), 190–197.

(164) Fogler, H. S. *Elements of Chemical Reaction Engineering*, 2nd ed.; Prentice-Hall: New Jersey, 1992.

(165) Yang, R. T. *Gas Separation by Adsorption Process*; Imperial College Press: Butterworths, Boston, 1987.

(166) Edwards, M. F.; Richardson, J. F. Gas Dispersion in Packed Beds. *Chem. Eng. Sci.* **1968**, *23*, 109–123.

(167) Yang, J.; Shih, S.; Lin, P. Effect of Carbon Dioxide on the Sulfation of High Surface Area $CaCO_3$ at High Temperatures. *Ind. Eng. Chem. Res.* **2012**, *51*, 2553–2559.

(168) Ye, Q.; Jiang, J.; Wang, C.; Liu, Y.; Pan, H.; Shi, Y. Adsorption of Low-Concentration Carbon Dioxide on Amine-Modified Carbon Nanotubes at Ambient Temperature. *Energy & Fuels* **2012**, *26* (4), 2497–2504.

(169) Gu, Q.; Henderson, R. T.; Tatarchuk, B. J. A CFD Pressure Drop Model for Microfibrous Entrapped Catalyst Filters Using Micro-Scale Imaging. *Eng. Appl. Comput. Fluid Mech.* **2015**, *9* (1), 567–576.

(170) Suzuki, M.; Smith, J. M. Axialdispersion in Beds of Small Particles. *Chem. Eng. J.* **1972**, *3* (November), 256–264.

(171) Fontell, E.; Kivisaari, T.; Christiansen, N.; Hansen, J. B.; Pålsson, J. Conceptual Study of a 250 kW Planar SOFC System for CHP Application. *J. Power Sources* **2004**, *131* (1–2), 49–56.

(172) Campanari, S. Thermodynamic Model and Parametric Analysis of a Tubular SOFC Module. *J. Power Sources* **2001**, *92* (1–2), 26–34.

(173) Waters, R. F.; Peri, J. B.; John, G. S.; Seelig, H. S. High Temperature Changes in Alumina Structure and Activity of Platinum-Alumina Catalysts. *Ind. Eng. Chem.* **1960**, *52* (5), 415–416.

(174) Edwards, M. F.; Richardson, J. F. Gas Dispersion in Packed Beds. *Chem. Eng. J.* **1968**, *23*, 109–123.

(175) Cahela, D. R.; Tatarchuk, B. J. Permeability of Sintered Microfibrous Composites for Heterogeneous Catalysis and Other Chemical Processing Opportunities. *Catal. Today* **2001**, *69* (1–4), 33–39.

(176) Van den Brand, J.; Sloof, W. G.; Terryn, H.; De Wit, J. H. W. Correlation between Hydroxyl Fraction and O/Al Atomic Ratio as Determined from XPS Spectra of Aluminium Oxide Layers. *Surf. Interface Anal.* **2004**, *36* (1), 81–88.

(177) Singh, J.; Mukherjee, A.; Sengupta, S. K.; Im, J.; Peterson, G. W.; Whitten, J. E. Sulfur Dioxide and Nitrogen Dioxide Adsorption on Zinc Oxide and Zirconium Hydroxide Nanoparticles and the Effect on Photoluminescence. *Appl. Surf. Sci.* **2012**, *258* (15), 5778–5785.

(178) Skaf, M.; Aouad, S.; Hany, S.; Cousin, R.; Abi-Aad, E.; Aboukaïs, A. Physicochemical Characterization and Catalytic Performance of 10% Ag/CeO_2 Catalysts Prepared by Impregnation and Deposition–precipitation. *J. Catal.* **2014**, *320* (3), 137–146.

(179) Yang, H. Gas Phase Desulfurization Using Regenerable Microfibrous Entrapped Metal Oxide Based Sorbents for Logistic PEM Fuel Cell Applications, 2007.

(180) Fritsch, S.; Navrotsky, A. Thermodynamic Properties of Manganese Oxides. *Journal of the American Ceramic Society*. 1996, pp 1761–1768.

APPENDICES

Appendix A Phase Diagram of MnO_x under Various Temperature and P_{O2}

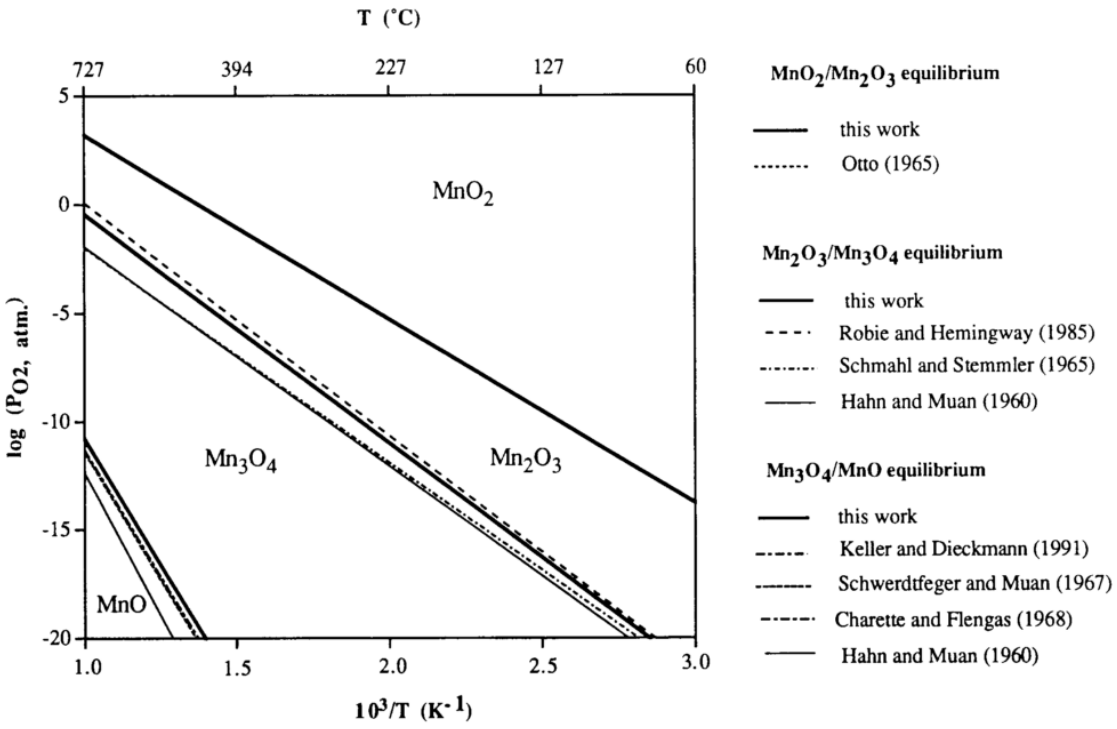

Figure A1. Phase diagram of MnO_2-Mn_2O_3-Mn_3O_4-MnO (p_{O2} given in atm)[180]

Appendix B Physical Properties of Gas Mixture

Appendix B.1 Viscosity Calculation

The viscosity of gas mixtures in this work can be calculated using the equations B-1, B-2, and B-3.

$$\mu = 2.6693\times10^{-5}\frac{\sqrt{MT}}{\sigma^2\Omega_\mu} \quad \text{(B-1)}$$

Where M is gas molecular weight, σ is collision diameter or called Lennard-Jones diameter of molecule, Ω_μ is a dimensionless parameter varying with $\kappa T/\varepsilon$.

The calculated values of O_2 and N_2 are 2.0293×10^{-4} and 1.7156×10^{-4} g (cm·s)$^{-1}$, respectively. Since the concentration of SO_2 is very low compared to O_2 and N_2, the contribution of SO_2 can be considered as negligible. The viscosity of gas mixture can be calculated using semi-empirical formula as follows:

$$\mu_{mix} = \sum_{\alpha=1}^{N}\frac{x_\alpha\mu_\alpha}{\sum_\beta x_\beta\Phi_{\alpha\beta}} \quad \text{(B-2)}$$

Where the dimensionless quantities $\Phi_{\alpha\beta}$ are

$$\Phi_{\alpha\beta} = \frac{1}{\sqrt{8}}\left(1+\frac{M_\alpha}{M_\beta}\right)^{-1/2}\left[1+\left(\frac{\mu_\alpha}{\mu_\beta}\right)^{1/2}\left(\frac{M_\beta}{M_\alpha}\right)^{1/4}\right]^2 \quad \text{(B-3)}$$

The viscosity of O_2 (12 vol.%) and N_2 (88 vol.%) mixture is 1.753×10^{-4} g (cm·s)$^{-1}$.

Appendix B.2 Gas Diffusivity Calculation

The diffusivity of SO_2-Air system was calculated using Fuller's equation as follows:

$$D_m = \frac{10^{-3} T^{1.75} (\frac{1}{M_A} + \frac{1}{M_B})^{\frac{1}{2}}}{P[(V_A)^{\frac{1}{3}} + (V_B)^{\frac{1}{3}}]^2} \quad \text{(B-4)}$$

Where D_m is the molecular diffusivity (cm^2/s), the molecular weight of SO_2 ($M_A =$ 64.07 g mol^{-1}), the molecular weight of air ($M_B = 28.97$ g mol^{-1}), the diffusion volume of SO_2 $V_A = 41.1$ cm^3 mol^{-1}, the diffusion volume of air $V_B = 20.1$ cm^3 mol^{-1}. Therefore, the calculated molecular diffusivity D_m is 0.122 cm^2 s^{-1}.

Appendix B.3 Particle Reynolds Number (Re_{dp}) and Schmidt Number (Sc)

The particle Reynolds number can be calculated as follows:

$$Re = \frac{d_p \rho U}{\mu(1-\varepsilon)} \quad \text{(B-5)}$$

Where the gas mixture density is 1184.6 g m^{-3}, face velocity U=1.33 m s^{-1}, and gas mixture viscosity $\mu = 1.753 \times 10^{-2}$ g (m·s)$^{-1}$, as calculated in Appendix B.1. So the Reynolds number is 13.57.

Schmidt number can be obtained as follows:

$$Sc = \frac{\mu}{\rho_a D_m} \quad \text{(B-6)}$$

Where $\mu = 1.753 \times 10^{-4}$ g (cm·s)$^{-1}$, $\rho_a = 1184.6$ g m^{-3}, $D_m = 0.122$ cm^2 s^{-1}. So the calculated Schmidt number is 1.213.

Appendix B.4 Mear's Criterion for External Diffusion

We use Mear's criterion to check if the external mass transfer from the bulk gas phase to the catalyst surface can be considered as negligible[164]. If the reaction is a first order reaction, Mears proposed that as follows

$$\text{If} \quad \frac{-r\rho_b(d_p/2)}{k_c C_{AO}} < 0.15 \tag{B-7}$$

The external mass transfer effects can be neglected.

In our case,

$$-r = 1.386\times10^{-7}\ kmol\ kg^{-1}\ s^{-1} \tag{B-8}$$

$$\rho_b = 757.9\ kg\ m^{-3} \tag{B-9}$$

$$d_p = 1.51\times10^{-4}\ m \tag{B-10}$$

$$Sh = \frac{\sqrt{(1-\varepsilon)}}{\varepsilon} Re^{1/2} Sc^{1/3} = 6.9 \tag{B-11}$$

$$k_c = \frac{ShD_m}{D_p} = \frac{6.9\times0.122\times10^{-4}}{1.51\times10^{-4}} = 0.557\ m\ s^{-1} \tag{B-12}$$

$$C_{AO} = 4.40\times10^{-7} kmol\ m^{-3} \tag{B-13}$$

Combining (B-7) ~ (B-13),

$$\frac{-r\rho_b(d_p/2)}{k_c C_{AO}} = 0.0324 < 0.15$$

Therefore, according to Mear's criterion, the external mass transfer coefficient can be neglected when u=1.33 m s^{-1}. The same conclusion can be drawn when u>0.66 m s^{-1}.

Appendix B.5 Axial Dispersion Effect

By using the equation mentioned in Chapter IV (the condition is listed in Table A1), we can obtain

$$\frac{1}{Pe_{dp}} = \frac{0.3}{ReSc} + \frac{0.5}{1 + \frac{3.8}{ReSc}} \tag{B-14}$$

$$Pe_{dp} = 2.36$$

$$Dz = \frac{Ud_p}{Pe_{dp}} = 5.91\times10^{-5}\ m^2 s^{-1}$$

To check if axial dispersion can be neglected or not, Finlayson's correlation can be employed as criterion as follows

$$\frac{-r\rho_b d_p}{U_o C_{AO}} \ll \frac{U_o d_p}{D_a} \tag{IV-20}$$

where $D_a = \frac{UL}{Pe}$

In this work, $\frac{-r\rho_b d_p}{U_o C_{AO}} = 0.0271$, and $\frac{U_o d_p}{D_a} = 2.362$

Table A1 Physical Properties of SO_2 Adsorption

U (m s^{-1})	1.33
d_p (m)	1.51×10^{-4}
ε	0.206
T (°C)	20
L (m)	5.25×10^{-3}
C_{AO} $(mol\ m^{-3})$	4.40×10^{-4}

Appendix B.6 Effect of Internal Diffusion

The effective diffusivity of SO_2 in the pores (*De*) can be calculated using equation (IV-21)

$$De = \frac{D_m \varepsilon \sigma}{\tau} \tag{B-16}$$

where ε is bed void fraction, which is 0.43 in this work; σ is constriction factor, which is assumed to be 0.5; τ is the surface tortuosity factor, for gamma alumina, assuming τ= 4. Hence, according to Weisz-Prater criterion for internal diffusion,

$$C_{WP} = \frac{-r\rho_b(\frac{d_p}{2})^2}{D_e C_{AS}} \tag{B-17}$$

where C_{AS}=C_{AO}, assuming the external mass transfer resistance can be neglected.

The internal effectiveness factor can be calculated as follows:

$$C_{WP} = 3(\Phi_1 coth\Phi_1 - 1) \quad \text{(B-18)}$$

$$\eta = \frac{3}{\Phi_1^2}(\Phi_1 coth\Phi_1 - 1) \quad \text{(B-19)}$$

The C_{wp} value, Thiele modulus, and internal effectiveness factor are summarized in Table IV.1.

Table A2 Internal Diffusion Parameters for Various Particle Size of Sorbents

Particle size (μm)	Log mean (μm)	C_{WP}	Thiele modulus (ϕ_1)	Internal effectiveness factor (η)
250~420	328	9.79	4.26	0.54
180~250	213	4.13	2.33	0.76
149~180	164	2.45	1.70	0.85
125~149	137	1.71	1.38	0.89
88~125	105	1.00	1.03	0.94

So there is certain internal mass transfer resistance in this adsorption system.

In this work, $CWP = 2.07.\Phi_1 = 1.542, \eta = 0.871$

Appendix C Matlab code for Mathematical Model

```
function [z,t,CA]=deactivation
% Partical Differential Equations:
% D(C)/D(t)=-uo/e*D(C)/D(z)+Dz*D^2(C)/D(z)^2-eta*ks*rho*(1-e)*C
%        if no internal diffusion, eta ~=1
%        GAMMA = u0/e
%        e=0.206,GAMMA=6.46;
%        DAB=Dz;DAB=8.5e-5;
%  In this case, according to the standard expression of PDE
%  m=0,
%  f(x,t,u,dudx)= -GAMMA*CA+ Dz*D(CA)/D(z),
%  c=1,
%  s(x,t,u,dudx)= -KO*exp(-KD*t)*CA;[a=exp(-KD*t)]
%  I.C. CA(z,o)=0, Z>0
%  B.C.
%  lefe side: CA(0,t)-CAO=0; so, pl=CA(0,t)-CAO,(pl=CAl-CAO;),  ql=0
%  right side: D(CA)/D(z)|(z=L)=0; that is, GAMMA/Dz*CA+
%  1/Dz*(-GAMMA*CA+Dz*(D(CA)/D(z)))=0
%  so, pr=GAMMA/DAB*CAr;qr=1/DAB;


global DAB CAO GAMMA KO KD
CAO=4.4e-4;
L=5.2e-3;
DAB=1.95e-4;
KO=24477.8;
KD=6.75e-4;
GAMMA=1.86; % uo/epsilon
h=10800;

t=linspace(0,h,100);
z=linspace(0,L,100);


m=0;
sol=pdepe(m,@deactivationpdefunb,@deactivationic,@deactivationbc,z,t);
CA=sol(:,:,1);
for i=1:length(t)
    [CA_i,dCAdz_i]=pdeval(m,z,CA(i,:),0);
    NAz(i)=-dCAdz_i*DAB;
end

% Generate 3D plot
surf(z,t/(60),CA/CAO)
title('Model 1')
xlabel('Bed Depth(m)')
ylabel('Time(min)')
zlabel('SO2 (C/Co)')
```

```
%PDE function


function [c,f,s]=deactivationpdefunb(z,t,CA,dCAdz)
global DAB GAMMA KO KD
c=1;
f=-GAMMA*CA+DAB*dCAdz;
s=-KO*exp(-KD*t)*CA;

%intial condition
function CA_i=deactivationic(z)
CA_i=0;

%boundary condition
function [pl,ql,pr,qr]=deactivationbc(z1,CAl,zr,CAr,t)
global DAB CAO GAMMA
pl=CAO;
ql=0.538;       %ql=epsilon/uo
pr=GAMMA/DAB*CAr;
qr=1/DAB;
```